

AD-A093 950

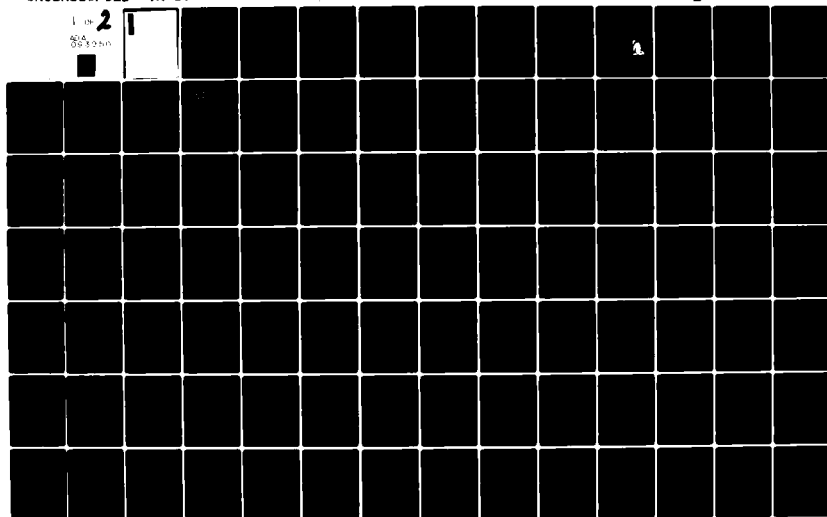
NORTHWESTERN UNIV EVANSTON IL DEPT OF MECHANICAL AND--ETC F/G 7/4
INVESTIGATION OF METAL AND METAL OXIDE CLUSTERS SMALL ENOUGH TO--ETC(U)
NOV 80 G D STEIN
TR-17

N00014-76-C-0378

NL

UNCLASSIFIED

1 of 2
ADA
003250



AD A093950

temperature. Even for the 100-atom cluster, a melting point
temperature of about 40 K is more than a factor of 2 lower

REPORT DOCUMENTATION PAGE		READ INSTRUCTIONS BEFORE COMPLETING FORM
1. REPORT NUMBER N00014-76-C-0378-TR17 ✓	2. GOVT ACCESSION NO. AD-H093950	3. RECIPIENT'S CATALOG NUMBER
4. TITLE (and Subtitle) INVESTIGATION OF METAL AND METAL OXIDE CLUSTERS SMALL ENOUGH TO CONSTITUTE THE CRITICAL SIZE FOR GAS PHASE NUCLEATION IN COMBUSTION PROCESSES		5. TYPE OF REPORT & PERIOD COVERED FINAL REPORT 10/1/75 - 6/30/79
7. AUTHOR(s) Gilbert D./Stein		6. PERFORMING ORG. REPORT NUMBER TR-171
9. PERFORMING ORGANIZATION NAME AND ADDRESS Northwestern University Department of Mechanical and Nuclear Engineering, Evanston, IL 60201 ✓		8. CONTRACT OR GRANT NUMBER(s) N00014-76-C-0378 ✓
11. CONTROLLING OFFICE NAME AND ADDRESS Office of Naval Research Arlington, VA 22217		10. PROGRAM ELEMENT, PROJECT, TASK AREA & WORK UNIT NUMBERS NRO 92-544 1-1-1
14. MONITORING AGENCY NAME & ADDRESS (if different from Controlling Office) ONR, Chicago 536 S. Clark Street Chicago, IL 60605		12. REPORT DATE November 1980
		13. NUMBER OF PAGES
16. DISTRIBUTION STATEMENT (of this Report) Distribution of this document is unlimited.		15. SECURITY CLASS. (of this report) Unclassified
17. DISTRIBUTION STATEMENT (of the abstract entered in Block 20, if different from Report)		15a. DECLASSIFICATION/DOWNGRADING SCHEDULE
18. SUPPLEMENTARY NOTES C		
19. KEY WORDS (Continue on reverse side if necessary and identify by block number) Clusters, Nucleation, Molecular Beam, Free Jet, Laval Nozzle, Electron Diffraction		
20. ABSTRACT (Continue on reverse side if necessary and identify by block number) Over the course of this contract a variety of techniques have been employed to study the properties of small atomic and molecular clusters formed in the gas phase via homogeneous nucleation. The clustering occurs either in an adiabatic expansion of a condensable species (e.g. argon, krypton, xenon, or sulfur hexafluoride) in an inert carrier gas (e.g. helium), or as a mixing process using a hot condensable (e.g. lead, silver, copper, indium or bismuth) and a cold carrier gas (e.g. argon,		

20.

helium, carbon dioxide or sulfur hexafluoride). A continuous development of several types of cluster sources has been carried out and includes free jets, very small hypersonic laval nozzles, and a series of metal ovens with carrier gas mixing. Any one, of these sources, constitutes the first stage of a differentially pumped, molecular beam system which then produces a continuous beam of clusters. The density in the beam is so low that it is collisionless and thus the clusters do not interact with each other or with any other foreign molecule or surface. The study of these isolated clusters is carried out primarily using high energy electron beams (40 to 75 KeV). The resulting diffraction patterns are obtained either on film or through use of a single channel, scintillation, pulse counting system employing synchronous detection. The diffraction patterns after interpretation, provide information on the structure of the clusters, as well as an estimate of their size and temperature. The size range studied extends from 50,000 down to 50 atoms per cluster. The goal is always to push toward the smallest size possible and to ascertain whether changes in structure occur. If there is a change in structure then the nature of the change and the size range at which it occurs is determined. It is found that as cluster size is reduced there were indeed structural changes such as, the transition from face centered tetragonal to face centered cubic (fcc) in indium, the appearance of icosahedral structure in noble gas clusters and the appearance of a new "amorphous" phase in metal clusters such as lead and silver. Computer programs were written to determine the extent and magnitude of changes to the diffraction patterns due to the possibility of electron multiple scattering within the cluster. These effects are significant for clusters of high atomic weight species and, of course, for very large sizes. Finally, an investigation was undertaken (but not yet completed) to examine the similarities and differences in the structural changes that occur in the noble gas clusters Ar, Kr and Xe, and in the metals Pb and Ag; all of which have f.c.c. bulk structure.

TABLE OF CONTENTS

	Page No.
Report Documentation Page.....	1
Publications Under ONR Contract N00014-76-C-0378.....	4
Reports Under ONR Contract N00014-76-C-0378.....	5
Atoms and Molecules in Small Aggregates: The Fifth State of Matter, G. D. Stein.....	6
Production and Electron Diffraction Studies of Silver Metal Clusters in the Gas Phase, B. G. DeBoer and G. D. Stein.....	17
Evidence for Mixed Clusters Formed During Sulfur Hexafluoride Expansions in an Argon Carrier Gas, S. S. Kim and G. D. Stein.....	39
Homogeneous Nucleation of Sulfur Hexafluoride Clusters in Laval Nozzle Molecular Beams, O. Abraham, S. S. Kim and G. D. Stein.....	49
Gasdynamics of Very Small Laval Nozzles, O. Abraham, J. A. Binn, B. G. DeBoer and G. D. Stein.....	84
Noble Gas Condensation in Controlled-Expansion Beam Sources, S. S. Kim, D. C. Shi and G. D. Stein.....	131
Distribution List.....	148

Accession No. _____

File No. _____

Index No. _____

Project No. _____

Report No. _____

Author _____

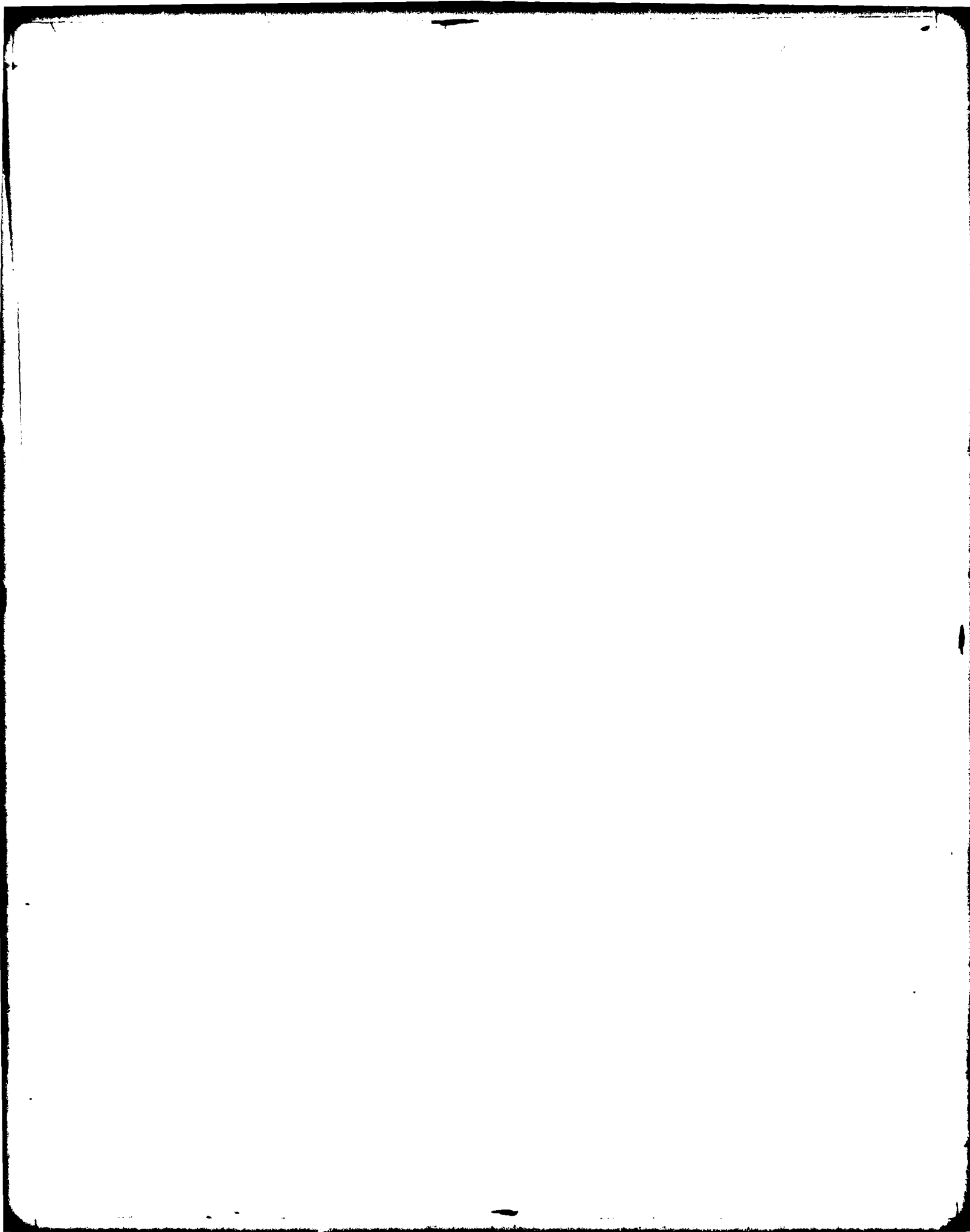
Editor _____

Reviewer _____

Approved _____

Disapproved _____

Remarks _____



- C. A. Moses and G. D. Stein, "On the Growth of Steam Droplets Formed in a Laval Nozzle Using Both Static Pressure and Light Scattering Measurements," Condensation in High Speed Flows, A. A. Pouring, Ed., American Society of Mechanical Engineering, New York, 1977.
- P. R. Jueck, 3rd and G. D. Stein, "Electron Diffraction Studies of Clusters Formed in Seeded Nozzle Beams," Colloque No. 2 Supplement au J. de Physique, C2-53 "Conference International Sur Les Petites Particules Et Amas Inorganiques," 1977.
- A. Yokozeki and G. D. Stein, "A Metal Cluster Generator for Gas Phase Electron Diffraction and Its Application to Bismuth Lead and Indium: Variation in Microcrystal Structure with Size," J. Appl. Phys., pp. 2224-2232, 1978.
- C. A. Moses and G. D. Stein, "On the Growth of Steam Droplets Formed in a Laval Nozzle Using Both Static Pressure and Light Scattering Measurements," Transactions of ASME, J. Fluids Eng., 100, pp. 311-322, 1978.
- A. Yokozeki, "Lead Microclusters in the Vapor Phase as Studied by Molecular Beam Electron Diffraction: Vestige of Amorphous Structure," J. Chem. Phys., 68, pp. 3760-3773, 1978.
- B. G. DeBoer, S. S. Kim and G. D. Stein, "Molecular Beam Studies of Sulfur Hexafluoride Clustering in an Argon Carrier Gas From Both Free Jet and Laval Nozzle Sources," Rarefied Gas Dynamics, R. Campargue, Ed., Commissariat a L'Energie Atomique, Paris, pp. 1151-1160, 1979.
- G. D. Stein, "Atoms and Molecules in Small Aggregates: The Fifth State of Matter," The Physics Teacher, 17, pp. 503-512, 1979.
- S. S. Kim, D. C. Shi and G. D. Stein, "Noble Gas Condensation in Controlled-Expansion Beam Sources," to appear in Rarefied Gas Dynamics, American Institute of Aeronautics and Astronautics, New York, N.Y.
- O. Abraham, J. A. Binn, B. G. DeBoer and G. D. Stein, "Gasdynamics of Very Small Laval Nozzles," submitted to Physics of Fluids.
- O. Abraham, S. S. Kim and G. D. Stein, "Homogeneous Nucleation of Sulfur Hexafluoride Clusters in Laval Nozzle Molecular Beams," submitted to Journal of Chemical Physics.
- S. S. Kim and G. D. Stein, "Evidence for Mixed Clusters formed during Sulfur Hexafluoride Expansions in an Argon Carrier Gas," to appear in the Journal of Applied Physics.
- B. G. DeBoer and G. D. Stein, "Production and Electron Diffraction Studies of Silver Metal Clusters in the Gas Phase," submitted to Surface Science.

Reports Under ONR Contract N00014-76-C-0378

G. D. Stein, "A Pre-expansion Cluster Generator for Nozzle Molecular Beams," Technical Report #1, January, 1977, 61 pp.

C. A. Moses and G. D. Stein, "On the Growth of Steam Droplets Formed in a Laval Nozzle Using Both Static Pressure and Light Scattering Measurements," Technical Report #2, January, 1977, 40 pp.

A. Yokozeke and G. D. Stein, "A Metal Cluster Generator for Gas Phase Electron Diffraction and Its Application to Bismuth Lead and Indium: Variation in Microcrystal Structure with Size," Technical Report #3, January, 1978, 35 pp.

A. Yokozeke, "Lead Microclusters in the Vapor Phase as Studied by Molecular Beam Electron Diffraction: Vestige of Amorphous Structure," Technical Report #4, November, 1977, 31 pp.

B. G. DeBoer, S. S. Kim and G. D. Stein, "Molecular Studies of Sulfur Hexafluoride Clustering in an Argon Carrier Gas From Both Free Jet and Laval Nozzle Sources," Technical Report #5, November, 1978, 12 pp.

G. D. Stein, "Atoms and Molecules in Small Aggregates: The Fifth State of Matter," Technical Report #6, February, 1979, 37 pp.

G. D. Stein, "Investigation of Metal and Metal Oxide Clusters Small Enough to Constitute the Critical Size for Gas Phase Nucleation in Combustion Processes," Final Report, November, 1980, 152 pp.

ATOMS AND MOLECULES IN SMALL AGGREGATES:
THE FIFTH STATE OF MATTER

G. D. Stein

The Physics Teacher, 17, pp. 503-512

Atoms and molecules in small aggregates

The fifth state of matter*

In our earliest encounters with the study of physics we were told that matter could be subdivided into three phases: solid, liquid, and gaseous, with physical features that made them distinct. As time went on we encountered a fourth state of matter: that of plasmas existing naturally in stellar and interstellar media and artificially in numerous research laboratories. Plasmas consist of a mixture of positively and negatively charged particles which indeed exhibit properties very distinct from those of the more familiar three states of matter. Now there is a fifth possibility. Those of us who have been pursuing the study of atoms and molecules in small isolated aggregates or clusters have made physical measurements on these systems revealing properties significantly different from those of the bulk phase, so much so that one might deem it appropriate to designate matter in this domain as the fifth state of matter. Even when clusters or particles are not in isolation their properties may still vary appreciably from bulk as in the case of colloids of sufficiently small size.

It will become apparent as we pursue the subject at hand that the physics of the boundary between the three traditional phases (i.e., interfacial phenomena) will become an omnipresent feature in the study of small clusters. When one considers clusters small enough so that they are essentially all surface, one should not be surprised to encounter physical phenomena which are at least atypical of the bulk phase and hard to calculate.

Small clusters arise naturally as an important entity in the treatment of the kinetics of phase change and in nearly all cases clusters are formed as the result of a phase change. Thus an interesting interdependence arises in which the physical properties of small clusters are important in theoretical predictions for the kinetics of phase change and conversely an understanding of the kinetics of phase change is important for the production of clusters of a given mean size for use in the measurement of their properties. For example the predicted rate of formation of water droplets in a condensing vapor (i.e., its nucleation rate) may vary by as much as a factor of ten billion (10^{10}) for a 30% variation in droplet surface tension. Understanding how the kinetics of water nucleation takes place provides the insight necessary to produce high concentrations of clusters of specific mean size and as narrow a size distribution as possible. This is important for any experiment designed to study cluster properties.

Nearly every technique for the formation of small clusters necessitates the creation of an environment where the species to be clustered is highly supersaturated. This is the single most important parameter for the production of high concentrations of clusters of very small size. Small cluster samples whether in the gaseous, liquid, or solid state, or on substrates (supporting surfaces) have been examined with photons as a probe, such as light scattering and absorption. A few of these techniques include such things as absorption spectroscopy, light scattering, both elastic (Rayleigh scattering) and inelastic (Raman scattering). All the modern techniques of tunable continuous wave (CW) and pulsed illumination (with laser pulse times as short as nanosecond to picosecond—that is 10^{-9} to 10^{-12} sec) are currently being brought to bear in the study of these small clusters. In addition, photons are being used to ionize the cluster species

*Based on a seminar given at Yale University while there on leave.

GILBERT D. STEIN



Gilbert Stein graduated from Purdue and received his Ph.D. from Yale. After a brief sojourn in aerospace research, he returned to Yale as an instructor before coming to Northwestern. His interests include, among travel, art appreciation, and collecting, and squash. He is currently learning French and piano from his children. Department of Mechanical and Nuclear Engineering, Northwestern University, Evanston, Illinois 60201.

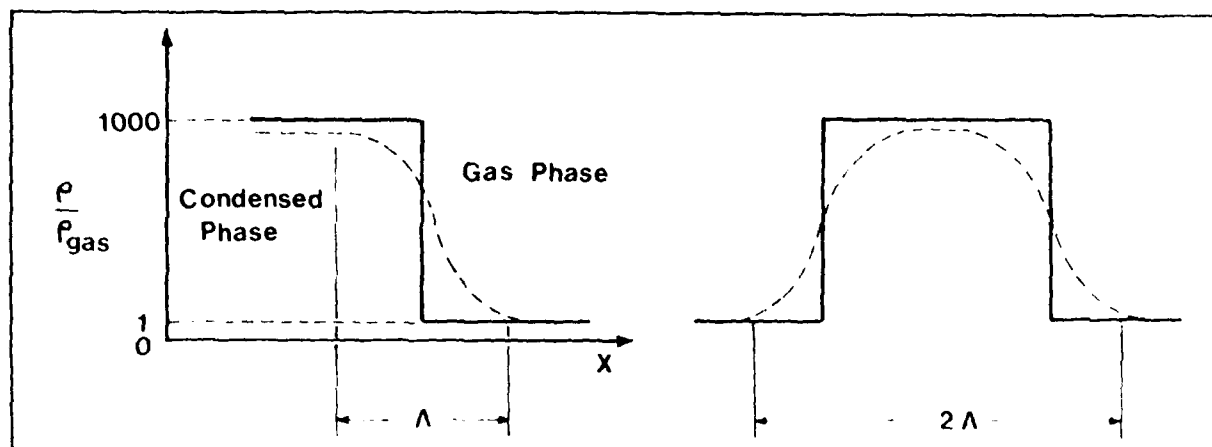


Fig. 1. The density change across a single interface is shown on the left. The solid line represents a mathematical interface while the dotted line shows the density variation in an actual interface. The characteristic length, $\Lambda \sim na$, where a is the average distance between atoms or molecules in the condensed phase. The case for two interfaces close together forming a one-dimensional thin film is shown on the right.

for subsequent mass analysis using mass spectrometers. Clusters are also being examined with electrons as a probe using both low- and high-energy electron diffraction and a variety of electron microscopic techniques. Very short-wavelength photons (x-rays) have also been used to study the structure of small clusters. Magnetic and electric fields have also been used for examination with methods such as nuclear magnetic resonance and electron spin resonance. Finally, neutrons have been used as probe particles to study the structure of small clusters.

Small cluster formation

At the outset one might ask how small does the particle have to be before it is considered to be a cluster having properties distinct from the bulk material? And why are small clusters important for the understanding of the dynamics of phase change? Let us begin by recalling a few features from classical or bulk macroscopic thermodynamics. We recall that a single component thermodynamic system could be completely described by the specification of three properties. For example, the volume of the system could be considered as a function of pressure, temperature, and mass, $V_1 = V_1(P, T, m_1)$. Now if this system is cut in half, each half may be described by $V_2 = V_2(P, T, m_2)$, where $m_2 = m_1/2$, and we see that the system is still specified with three variables. However, if one continues this process of cutting the system in half, we will see that at some point the system begins to display some additional properties which were not noticed previously. For example when the system size begins to get small we notice that the components begin to stick together or stick to solid surfaces or nearby walls. Clearly some other thermodynamic property is coming into play. If one were to continue this halving process even further there would come a point at which the small particles would begin to levitate or float about in the medium, be it liquid or gaseous, displaying Brownian motion. Again, we are beginning to observe another physical phenomenon that was not apparent in the large systems. In order to define uniquely the classical thermodynamic state of the system additional properties must be specified, for example, size, or surface charge, or surface free energy. Typically when particles

approach the 10 to 100 μm ($1 \mu\text{m} = 10^{-6} \text{ m}$) size range they will begin to exhibit the above mentioned features.

Let us now consider another process treated in introductory physics or thermodynamics. Imagine a gas enclosed in a cylinder where a piston is free to move and is subject to constant pressure. As heat is removed from the gas the piston slowly descends until at some point phase change begins and liquid appears in the bottom of the cylinder. But if one actually performs this experiment it is seen that the liquid phase may not appear at the vapor-liquid equilibrium temperature and the gas will instead supersaturate. Several implicit conditions are required in order to realize the idealized phase change.

1. In order for the phase change to occur and the liquid to form, a surface onto which the liquid will collect is required. If the walls of the cylinder are suitable they can provide the needed surface.

2. If the surface is not available, that is, not effective as an active site for the formation of the new phase, then the new phase will have to begin homogeneously, that is, it will have to form upon itself. Classical thermodynamics tells us that in order to have a droplet of finite radius in equilibrium with the gas, the gas must be supersaturated. In fact, the smallest possible radius of such a spherical drop is inversely proportional to the natural log of the saturation ratio. Once the droplet exceeds this radius it will grow without limit and produce sufficient condensed phase to establish a stable thermodynamic equilibrium.

3. The reason the gas supersaturates is because it is cooled at a finite cooling rate as opposed to an infinitely slow cooling rate required for a quasistatic process in classical thermodynamics. Even when a gas is supersaturated the new phase may not form at an appreciable rate because there is a positive amount of energy required to form the droplet of the minimum radius r^* . Essentially the reason for this is due to the energy of formation of the surface $4\pi r^2 \sigma$ where σ is the surface tension. Thus the higher the supersaturation of the gas the smaller is r^* , the smaller is the energy barrier to the formation of the droplet of critical size, and the more rapid is the rate of formation of the droplets or clusters. Thus we see that the further out of equilibrium the thermodynamic system is,

TABLE I Cluster size for bulk density		
No. of interatomic Distances, n	$2\lambda = 2n$ a	$g_B = (2n+1)^3$
3	6	343
4	8	729
5	10	1331

the greater is the rate process which drives the system back toward equilibrium.

For virtually every type of actual phase change, whether formed homogeneously as pure droplets or heterogeneously as a droplet growing on a surface or a foreign site, whether a phase change between gas and liquid, gas and solid, or solid and liquid, the starting or critical size involves a cluster or aggregate whose size g is less than 1000 molecules (atoms if monatomic species) per cluster. Beyond the critical size the new phase can grow without limit. How does this size range compare with the size limit at which bulk properties are valid? In order to estimate this size let us consider properties at an interface between two phases. For example, consider the density as a function of position across an interface as shown in Fig. 1. Typically the density change from gas to condensed phase is of order 1000:1. Mathematically we might consider that the interface occurs at a plane of zero thickness. Microscopically, when one considers that a phase is made up of discrete atoms or molecules, the density change will occur across some number n of mean intermolecular (interatomic) distances λ . Thus the characteristic length over which the density goes from bulk liquid to bulk gas is $\lambda = n a$ where n would be no smaller than 3 and perhaps as high as 10 or more. Now consider a slab of condensed phase with gas phase on two sides as shown in Fig. 1B. The minimum characteristic length at which bulk properties would obtain at the center of the condensed phase would be roughly 2λ . If we consider a three-dimensional condensed phase (i.e., a droplet-like entity) we can estimate the number of atoms or molecules required in order to have bulk properties even though only at the center of the droplet. The results of this estimate are shown in Table I where the number of interatomic or intermolecular distances required for the density change from that of gas to condensed phase is varied from 3 to 5. We see that a cluster must have more than 343 (1,331) molecules or atoms in the cluster, if $n = 3(5)$, before there is enough material in the droplet so that there is bulk property anywhere in the cluster. Note that if $n = 5$ then virtually all the critical size clusters for the formation or nucleation of a new phase fall within the region wherein bulk physical properties will not be present anywhere in the droplet.

The above estimate was made with density as the property that was varied. There are many physical properties other than density that may be considered and numerous estimates have been made in the literature of the cluster size at which these other properties begin to deviate from

those of the bulk. These estimates are based on approximate models and are therefore subject to challenge. For example, it has been estimated that only 3 to 4 atoms are necessary to approximate the electronic structure of a metal cluster whereas other estimates for properties such as the latent heat or surface tension require several thousand atoms or molecules in a cluster before bulk values are approached.

Clusters are everywhere

From the foregoing discussion it is evident that clusters are important wherever there is a physical phase change involved. This one phenomenon alone can involve a tremendous scope of applications. For example, the nucleation and growth of small metal particles on substrates is very important for thin-film and solid-state devices. Many atmospheric phase changes such as the formation of solid aerosols, water condensation, and hail formation involve small nuclei to initiate the processes. Physical properties of metals are determined in part by the cluster concentration and therefore the metal grain size. Many chemical engineering processes require the condensation of crystallites or formation of liquid droplets that initiate the formation of a new phase. The products of combustion such as water or carbon dioxide and steam in many types of engines and turbines can condense into droplets and cause subsequent damage to parts downstream of the condensation process. Performance of boilers and condensers in large equipment depend on nucleation phenomena.

Cloud chambers and bubble chambers for use in high-energy physics are examples of radiation-induced nucleation. Numerous geologic and cosmologic phase changes are important within the earth and beyond. The list can go on and on. One very important application for small clusters is in the field of catalysis where for some chemical reactions it has been found that small metal and metal-oxide clusters are much more effective than bulk material in promoting chemical reactions. Other diverse areas, such as the study of the theory of liquids, involve a model which is essentially that of a cluster. The use of heterogeneous cloud seeding agents in the atmosphere for the control of rainfall, increasing snow pack in mountains, and the suppression of hail damage to crops are other examples of the use of small clusters.

Clusters are systems which are small in three dimensions but there are examples of systems that are small in one and two dimensions which also exhibit behavior not typical of bulk material. For example, thin films are small in only one dimension and once they become thinner than about 1000Å (100 nm) their properties begin to show deviation. Examples of systems which are small in two dimensions are those of fibers or whiskers. Their properties also are different from bulk. In particular for crystalline materials, due to the small volume involved, the probability for imperfections or dislocations is reduced thereby resulting in materials with unusually high strength. Is it possible that some materials in small cluster form might be ideal for superconducting materials? This prospect would have great economic implications.

Examples of property changes of small aggregates

The problem of comparison between a cluster and a bulk phase of the same material may be considered in terms of a two step change. The first step would involve identifying a certain number (g) of molecules in the bulk

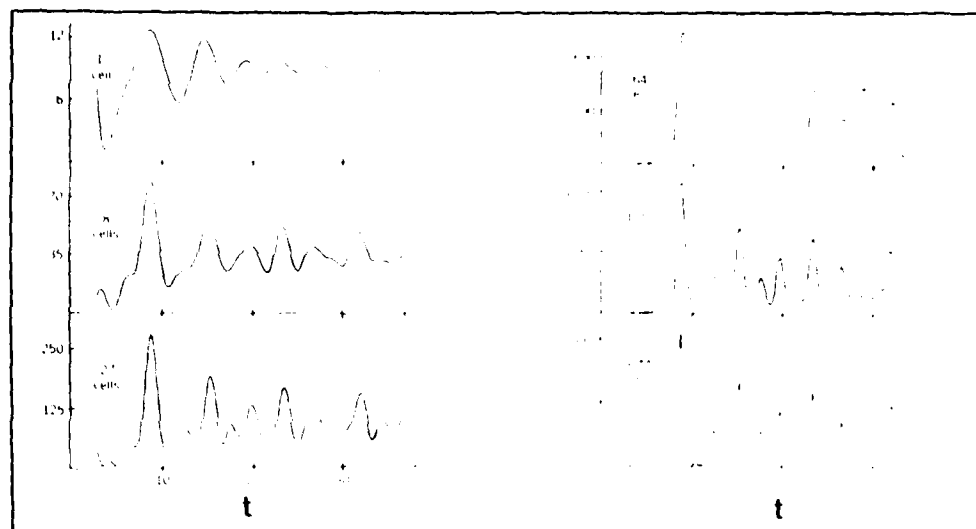


Fig. 2. Theoretical x-ray diffraction patterns are shown for a body-centered cubic lattice as a function of the number of unit cells in the cluster. The y coordinate is a relative scale for peak height, while for x, t is a function of the angle of scattering for the x-ray. Thus the changes in diffraction pattern occur even for perfect unit cells as the cluster size gets smaller with dramatic changes below 20 cells per cluster. (From C. Morozumi and H. C. Ritter)

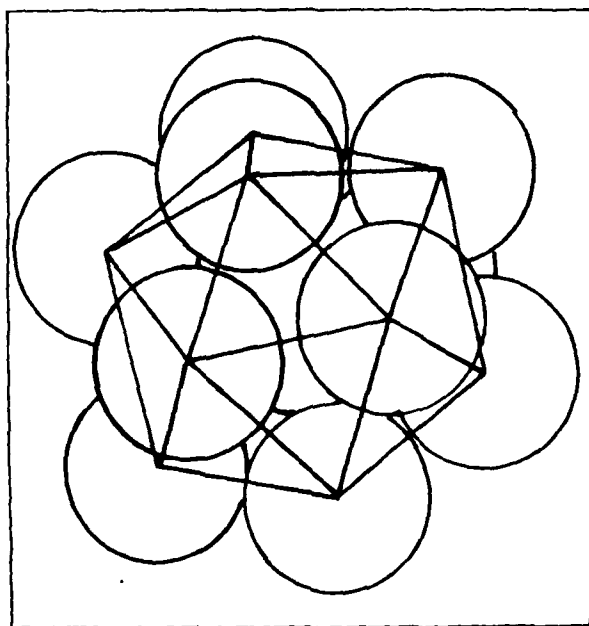


Fig. 3. The minimum energy configuration for van der Waals type atomic clusters with $g \leq 55$ atoms is that of the icosahedral packing. A complete 13-atom icosahedron is shown here.

phase and imagine them removed or isolated from the bulk with exactly the same structure (i.e., atomic positions). The finiteness of the new system alone will cause a change in some physical measurements, for example diffraction patterns. The second stage of the process then would be to allow the cluster to relax into its equilibrium position as an isolated entity. This then would result in further variations of some physical properties.

Consider the case of x-ray or electron diffraction from a crystal which is perfect but of finite extent. Complete constructive interference at the Bragg angles and destructive interference at the angles in-between, resulting in infinitely narrow diffraction peaks, require a crystal of infinite extent. As the crystal becomes finite in size the peaks are broadened and peak heights reduced, but with little additional changes as the size goes from infinity down to micron diameter. The broadening occurs for finite crystals because at angles slightly off the Bragg angle (say $\Delta\theta$) there are not enough scatterers in the crystal lattice for complete destructive interference. The fewer atoms (molecules) in the lattice the poorer is the destructive interference for a given $\Delta\theta$. Hence the peaks are increasingly broadened as the size decreases (This phenomenon is analogous to the resolving power of a diffraction grating like those used in spectrographs and monochrometers. The greater the extent of the grating the better is its resolution.) Below this size (μ in diameter) the peaks begin to alter more rapidly¹ and, as the number of unit cells decrease below about 100, the patterns take on substantial changes as seen in Fig. 2. Thus even with perfect unit cells (body-centered cubic-BCC, in this case) which have no interatomic variations in distance, no thermal vibration of the atoms about equilibrium positions and no crystal defects, the diffraction pattern is drastically different from

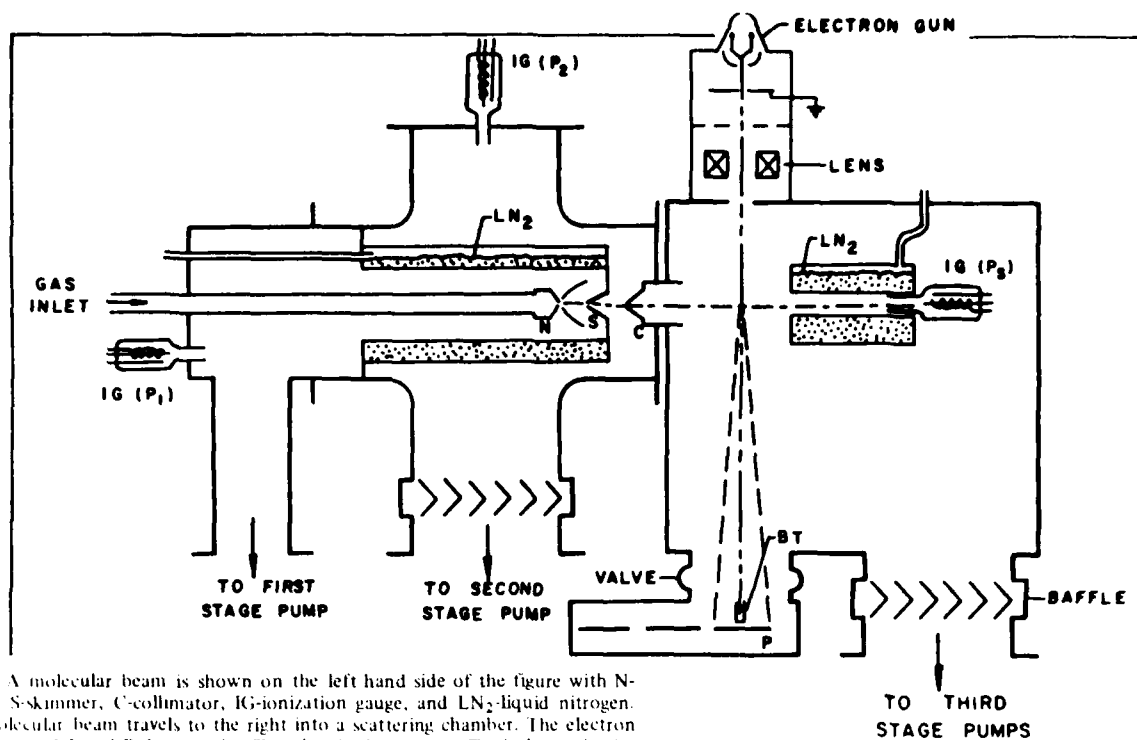


Fig. 4. A molecular beam is shown on the left hand side of the figure with N-nozzle, S-skimmer, C-collimator, IG-ionization gauge, and LN₂-liquid nitrogen. The molecular beam travels to the right into a scattering chamber. The electron beam trap is BT and P denotes the film plate in the cassette. Typical energies for the electron beam are in the neighborhood of 40 000 eV.

that of the bulk for the small clusters. In order to model successively more realistic clusters for comparison to experiment, one must add to the perfect model the above mentioned effects.

Argon clusters

Let us consider the structure and properties of a "simple" monatomic species which exhibits little or no chemical bonding but only the much weaker van der Waals attraction. Argon is the most common of this family and its bulk crystalline structure is face-centered cubic (FCC, i.e., a cube with atoms at the corners and centered on the six faces). The interaction potential between two argon atoms, that is, the attractive or repulsive force which is a function of the distance between them, operates between any two argon atoms in a simple additive manner. Using a simple potential function, which fits experimental measurements, minimum energy configurations for clusters as a function of size have been computed. These so-called static calculations have been made by numerous researchers. It was found² that for clusters up through size 55 the equilibrium configuration is not FCC but tends toward the icosahedral packing shown in Fig. 3. With single atoms being added sequentially the icosahedral structure cannot propagate itself and at some point the minimum energy configuration for the growing cluster will revert to face-centered cubic.

There is experimental evidence for the postulated icosahedral structure for crystalline argon obtained using a nozzle-molecular beam technique by a research group at the University of Paris (Orsay).^{3,4} A typical molecular beam configuration is shown in Fig. 4 and has been used over the last 20 years for a great variety of research investigations.⁵ It consists of a gas source which is either a small

nozzle or an orifice free jet (i.e., a pin hole in a thin metal disc) and is operated at pressures high enough so that the expansion through the hole forms a free jet or plume in the evacuated first stage of the beam. As the gas expands it cools adiabatically, becomes supersaturated, and clusters begin to nucleate. The pressure in the first stage of pumping is low enough so that the density in the free jet becomes so low that the expansion becomes essentially collisionless. Somewhere near this point in the expansion an aperture is used to define a beam. It is formed as a cone with a hole in it to minimize aerodynamic interference with the beam that passes through it and is called a skimmer. Frequently a second stage of pumping is used in order to keep the pressure in the scattering chamber as low as possible. For a given gas, if the gas inlet pressure p_0 is low, clustering is progressively increased, more and more clusters will form, resulting in a cluster beam. For structure analysis of the cluster beam, a high-energy electron gun is placed at right angles to the cluster beam just downstream of the collimator in this scattering chamber. Diffraction patterns are taken, usually on film, with a beam stop to catch the primary undiffracted electron beam. The cluster beam intensity is monitored using an ionization gauge or a mass spectrometer.

Electron diffraction patterns from clustered argon beams have been obtained and compared to theoretical structure calculations. The patterns for large clusters ($g \geq 500$) compare well to FCC bulk structure. Where the size ranges from $g \approx 50$ the data is reproduced well using a model which is a combination of icosahedral clusters and beam gas.⁴ The fraction which is icosahedral goes from 80% to 0% as g goes from 50 to 20. Even though one may expect a small range of sizes in the cluster beam, the comparison is nevertheless very good and thus provides the experimental

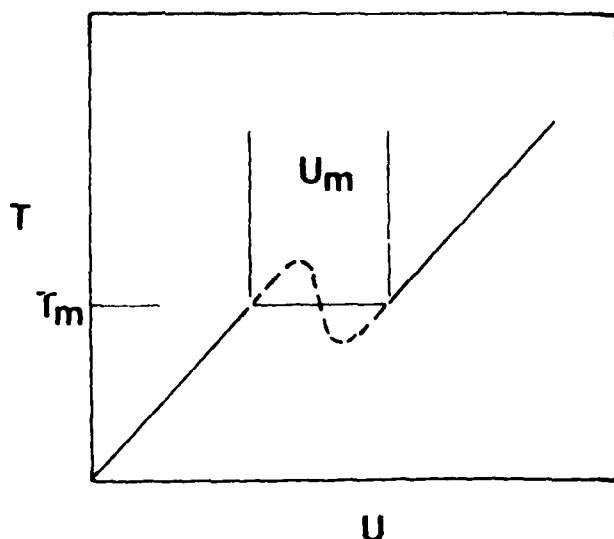
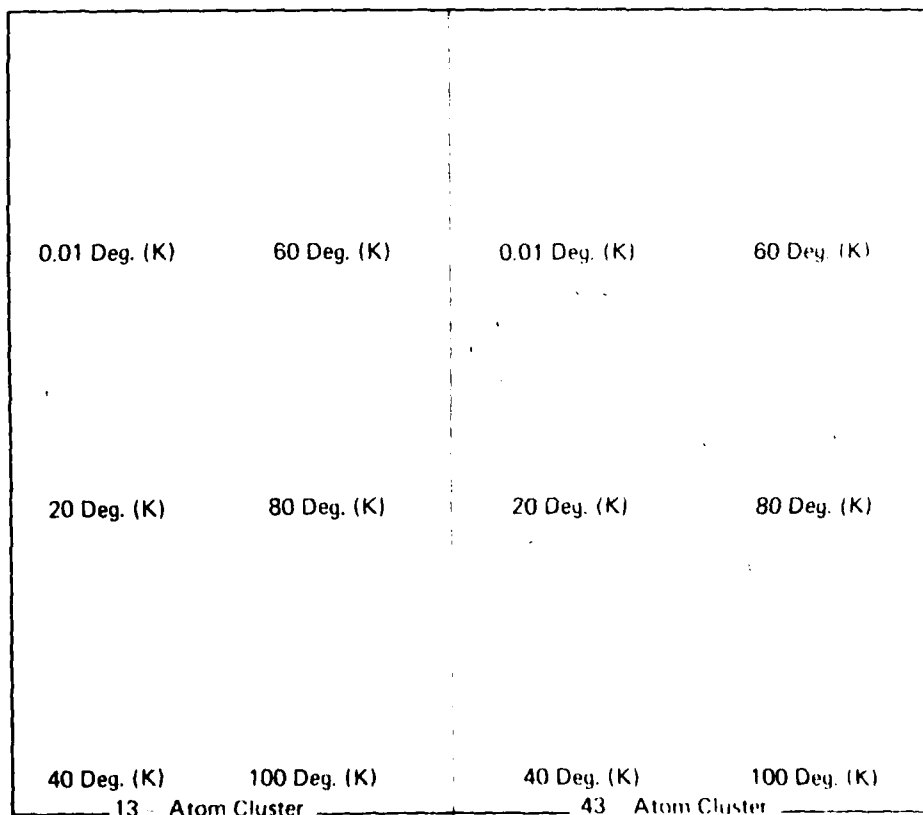


Fig. 5. Theoretical molecular dynamics calculations for argon clusters can be presented on a temperature versus energy per atom plot as a function of cluster size. The so-called van der Waals loop is shown with T_m the melting point temperature and U_m the energy of vaporization. The results show evidence of a van der Waals loop and thus a phase change even for the size 4 or tetramer.

Fig. 6. Individual snapshot pictures from 13-atom and 43-atom clusters were obtained from Monte Carlo simulation at various temperatures. Note the icosahedral packing at very low temperature and evidence of a transition to a liquidlike or amorphous structure in the temperature range of 40-60 K in agreement with the molecular dynamics calculations.⁶ (Reprinted with permission from E. E. Abraham.)



verification for the appearance of these minimum energy icosahedral argon structures under proper molecular beam operating conditions.

In addition to static structure configurations, dynamic calculations have been carried out by a number of researchers in which there is kinetic and potential energy interaction within the cluster. Basically two theoretical techniques have been employed. The first is called molecular dynamics in which each particle is given an initial position and velocity and the evolution of the cluster is followed with ordinary Newtonian mechanics. The second technique is called Monte Carlo with the calculations initiated using an ensemble of g atoms located within some arbitrary spherical volume. Using a given interatomic potential, the potential energy of the initial configuration is calculated. Then one of the atoms is chosen at random and given a random displacement. A new potential energy is then calculated followed by a second random displacement. After a large number of these steps the potential energy is ensemble averaged and a cluster equilibrium state determined. All of the thermodynamic properties can then be calculated from these or subsequent configurations.

Results obtained using molecular dynamics⁶ show a triple-valued van der Waals-type loop in the energy per atom as a function of temperature as the cluster size is increased. The structure of the cluster passes from solid to liquid in the loop region as temperature is increased, analogous to a van der Waals loop for an isotherm in a pressure-volume diagram for a bulk phase change (see Fig. 5).

Several interesting features are predicted⁶:

1. The melting point of a cluster is dependent on its size, that is, the smaller the cluster the lower the melting

temperature. Even for the 100-atom cluster, a melting point temperature of about 40 K is more than a factor of 2 lower than the 84 K melting point temperature of bulk solid argon.

2. The 13 atom cluster, which is a complete icosahedron, has a "heat of fusion" (U_m in Fig. 5) which is larger than the clusters above and below it. This again points to the minimum in potential energy for this configuration or an optimum in van der Waals bonding, thus requiring more energy per atom for its phase change.

3. For the larger size clusters, as the temperature increases toward the melting point, other calculations predict that the cluster is partially liquid and partially solid. It has been postulated elsewhere that clusters in this regime would be liquid-like near the surface with the core remaining solid.

An example of the results that can be obtained using Monte Carlo calculations are shown in Fig. 6. Here single configuration snapshots are shown for a 13 atom and a 43 atom cluster at temperatures between 0.01 K and 100 K.⁷ We see that as the temperature nears 0 K the structure is very close to that of the icosahedral minimum energy configuration. It is also noted that as the temperature increases to the range of 40-60 K the structure is definitely moving away from icosahedral in qualitative agreement with the molecular dynamics calculations.

Water clusters

The above section dealt with simple monatomic systems possessed of weak interaction due to the van der Waals attractive force. Here we will consider a case of hydrogen bonding which is much stronger than van der Waals attraction by a factor of about 20.

An investigation of the structure of water clusters in the gas phase using high-energy electron diffraction was undertaken in our laboratory⁵ a few years ago using the molecular beam apparatus shown in Fig. 4. The structure of these clusters was not the usual hexagonal form of ice but instead was *diamond cubic*. The diffraction patterns are shown in Fig. 7 with stronger patterns occurring at higher

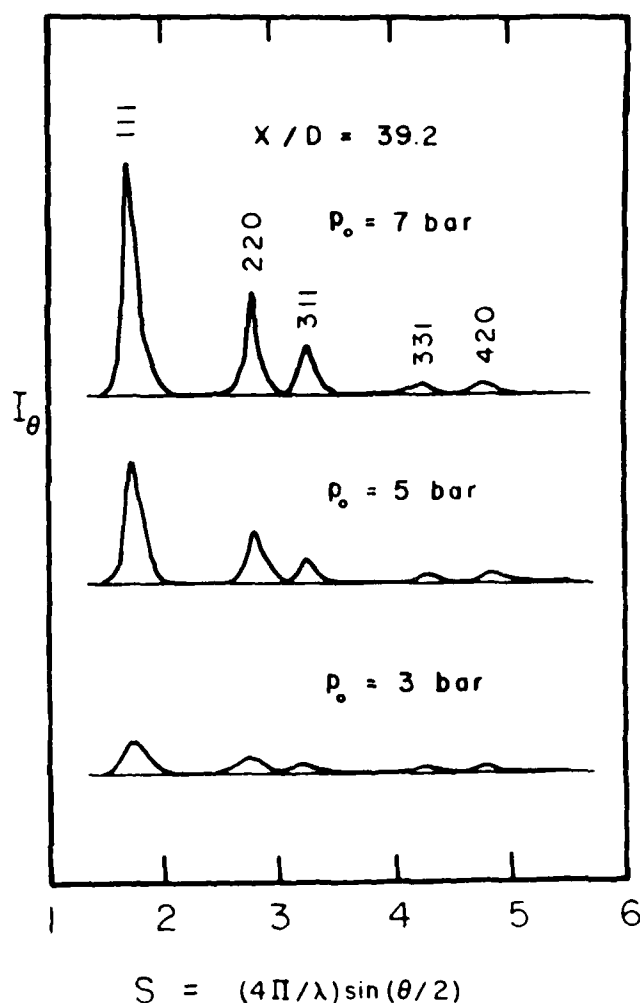


Fig. 7A

Fig. 7. Electron diffraction patterns for water with the background subtracted out are shown in A as obtained from the molecular beam apparatus shown in Fig. 4 for three beam starting pressures. The average size for these clusters is in the range of $p = 2600$ to 330 and is characteristic of the bulk diamond cubic structure of ice. The diamond cubic structure is shown in B with the water molecules shown only as circles to simplify the presentation which is basically that of FCC with 4 molecules interior to the unit cell located as shown.

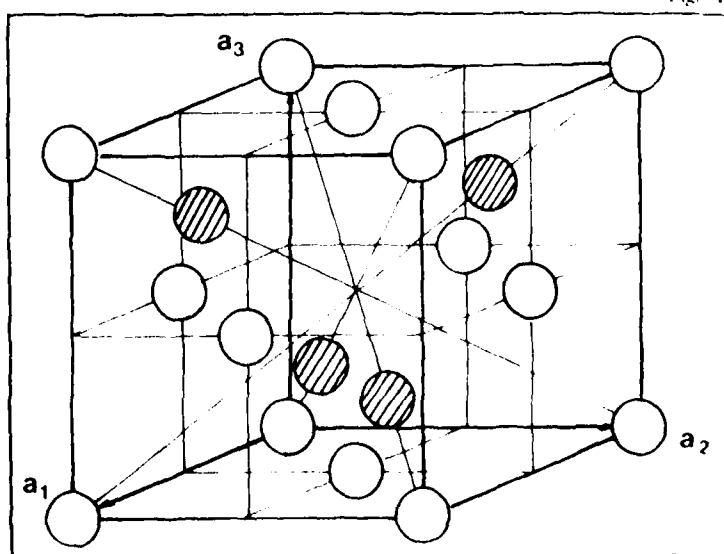


Fig. 7B

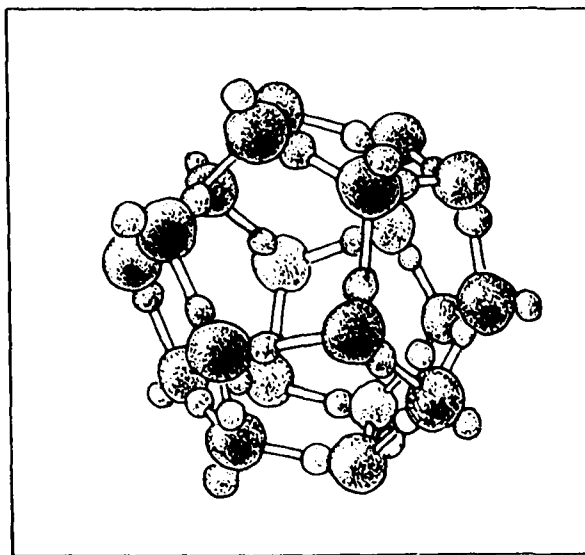


Fig. 8. Static, minimum energy calculations for water clusters predict a five-sided dodecahedron clathrate structure shown here with a hollow interior. A foreign atom or water molecule may be trapped within the clathrate. This structure is drastically different from those of the ordinary condensed phases of ice. (Reprinted with permission from J. L. Kissner, Jr.)

beam source pressures. The smallest average cluster size for which patterns were obtained in this work was 330 molecules per cluster. Careful examination of this structure reveals that each water molecule has the tetragonal coordination characteristic of maximum bonding or minimum energy configuration. Bulk ice structure of this form has been obtained provided it is condensed from the vapor phase on a substrate in the neighborhood of 150 K.

Even more unusual structural forms than diamond cubic are predicted for water when the cluster size gets smaller. Just as with argon, where certain sizes produce minimum energy configurations (in that case icosahedral), so water also is predicted to have certain minimum energy configurations with the five-sided geodesic dodecahedron type of dodecahedron configuration⁸. They are called clathrate structures and are either completely void on the interior or sometimes enclose either another water molecule or a foreign atom. The clathrate structure is shown in Fig. 8 and contains 20 molecules in the cage. Clathrate structures stabilized with xenon atoms have been formed via crystallization from the liquid state but have never been observed until recently to have formed from the vapor phase. The evidence for the vapor phase clathrate structure is based on the relative abundance of various size clusters sampled in molecular beams with mass spectrometers. These have been produced from homogeneous (i.e., pure) water clusters⁹ and also, by a group at Yale University, using protons as nuclei¹⁰.

Again, these structures are radically different from the usual bulk crystalline phases of ice and they cannot propagate themselves with the dodecahedral symmetry by

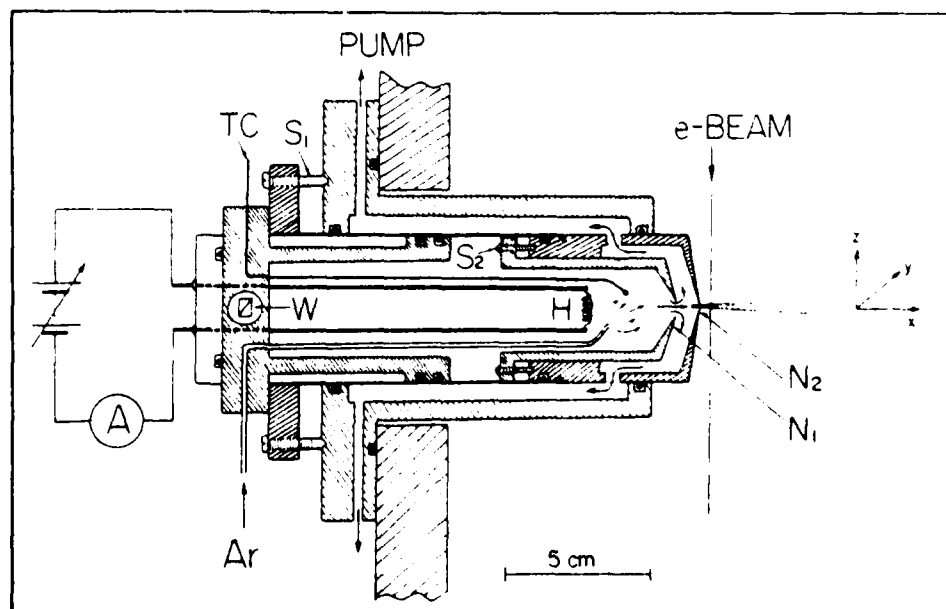


Fig. 9. The schematic arrangement of an oven for the formation of metal clusters is shown. The symbols stand for TC—thermocouple, W—prism mirror window, H—heater for metal vaporization, S₁ and S₂—sets of screws for configuration adjustments, Ar—argon carrier gas, N₁ and N₂—flow orifices or nozzles. In this device the metal is vaporized by resistive heating and the metal nucleates downstream of the heater. The sample is pulled through the orifice N₁ and part of it forms a supersonic molecular beam through N₂. The metal to be evaporated is either placed directly on the heater or in a crucible with the heater coiled around it. The electron diffraction is carried out just downstream of the orifice N₂.

the addition of gas-phase molecules condensing. Just as with argon, as the size gets larger the minimum energy configuration reverts to one of the more usual bulk forms

Metal clusters

For a number of years in our laboratory we have carried out a systematic study of the structure of small clusters formed in the vapor phase. Due to the relatively low vapor pressure of metals, plus their relatively strong bonding (a factor of about 20 greater than the hydrogen bonding in water), and high surface tension, the design criteria for a cluster molecular beam is much different from that for gaseous species.¹¹ The most important design criterion for a metal cluster beam source which will produce small size clusters with sufficient cluster concentration to conduct experiments, is that the supersaturation be very high. This produces an enormous cluster nucleation or formation rate so that, on the time scale of the experiment, cluster concentrations of 10^{10} to $10^{13}/\text{cm}^3$ are produced. With that many clusters competing for the remaining metal vapor, the average size remains quite small.

A metal cluster oven design used in our laboratory is shown in Fig. 9. The metal is vaporized in an inert atmosphere pressure at about 1 Torr (1/760 of an atmosphere) and the gas flowing slowly over either a vapor heater filament or crucible toward the first orifice N_1 . Part of the sample passing through N_1 is pumped by mechanical pumps and the remainder passes through a supersonic orifice N_2 and becomes the cluster beam to be examined using high energy electron diffraction. This source replaces the gas molecular beam in Fig. 4 and is connected directly into the scattering chamber. A number of metals have been studied using this source, resulting in some surprising and exciting results.

Consider the case of indium. Its bulk structure is face centered tetragonal (that is, face centered but with a height c which is greater than its square base a). Figure 10 indicates that when the indium clusters have 5 000 atoms per cluster or larger they exhibit the bulk structures just mentioned. However, as they are made progressively smaller, we can see that the height dimension c decreases while the size of the base a increases with the result that at about $g = 2000$, $c = a$ and the structure becomes face-centered cubic (FCC). The structure appears to be more compact. (Are the surface tension forces which create higher pressures in small droplets the motivating force here?) However an examination of the density of the small size FCC structure shows that it is within 1% of the bulk density. Nevertheless we feel that the structural rearrangement is significant and occurs at a cluster size in a range of 2 000 to 4 000 atoms per cluster which can be considered as relatively large (i.e. containing 500 to 1 000 unit cells).

As a second example consider the case of lead. Figure 10B shows the variation of the unit-cell parameter (which is FCC) with size. Note the very small variation in unit cell dimension with size (observe that the y coordinate is greatly expanded over that of part A) so that on first examination the data for lead does not appear interesting. Careful examination of the data shows that it is consistent with a model of a cluster which has a core which is crystallized, plus a surface layer which becomes progressively more disordered or liquid-like as the cluster gets smaller.¹²

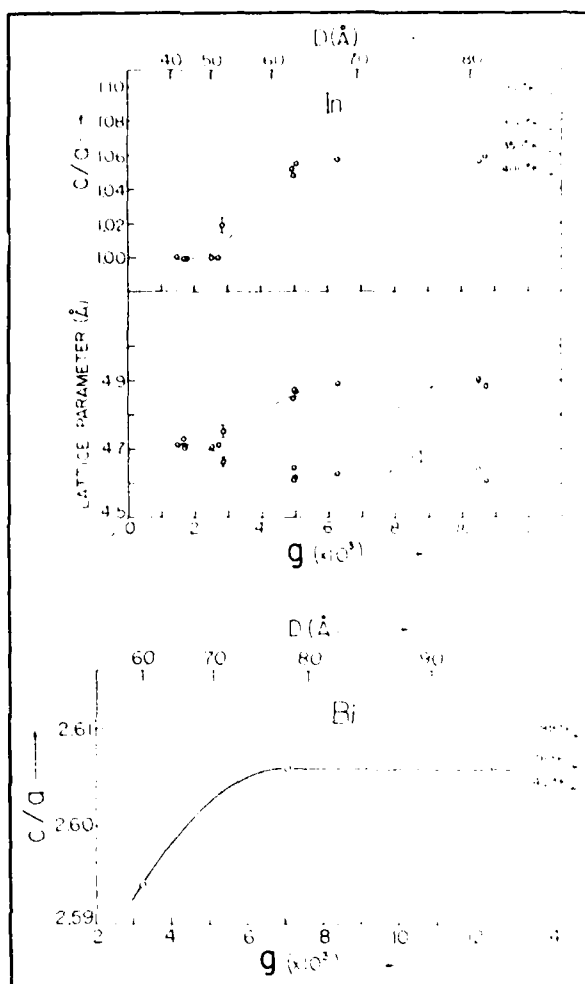


Fig. 10. The unit cell lattice parameters height c , base a , and then ratio, for indium microclusters are plotted as a function of the number atoms in the cluster, g , and the average cluster diameter, D . Broken lines indicate the corresponding values in bulk crystalline materials at various temperatures. Typical experimental error bars are shown by vertical lines. Deviation from bulk structure begins as the diameter approaches 5000 atoms per cluster average size. In B the unit cell parameter for lead is plotted as a function of g . Note the expanded scale for unit cell parameter with very little change in the lead unit cell with size. The indium, on the other hand, has undergone a structural change from face-centered tetragonal to face-centered cubic as the size is decreased to the 2 000 atom per cluster range.

Because the atomic weight of lead is so large, the possibility of multiple electron scattering within the crystal lite is of some concern. Therefore another FCC monatomic structure, that of argon mentioned above ($g > 800$), has been examined and the same effect seen. Thus with decreasing size a larger fraction of the cluster becomes surface with the crystalline center becoming progressively a smaller fraction of the atoms in the cluster. Presumably, then, the structure of the clusters in the 100 to 1 000 atom per cluster range would be completely amorphous or liquid.

like as suggested by the argon data referred to earlier for $g \leq 50$. But then again we may be surprised by the small cluster structure as with the previous examples.

Cluster studies with the laser

With the advent of tunable, highly monochromatic, high power, and very short-pulsed lasers many traditional and new research areas are blossoming forth. The study of small clusters is one of these, and recent advances have occurred at a very rapid rate. Some beautiful spectroscopic studies have been carried out by scientists at the University of Chicago.¹³ They employ highly cooled, free-jet expansions of helium containing a very small quantity of the species of interest (such as iodine) and have obtained highly resolved spectroscopic data on vibrational and rotational structure of very small clusters. Impressive progress on the study of metal clusters has been made using matrix isolation techniques (metal clusters condensed in a matrix of solid argon for example) with laser spectroscopy, particularly at the University of Toronto.¹⁴

Very recently laser spectroscopic studies of small metal clusters in the gas phase have been undertaken in a nearly ideal experimental configuration at the University in Bern, Switzerland.¹⁵ This technique involves the formation of a metal cluster beam and selective electronic excitation by cluster size using a tunable laser. A second high-intensity laser pulse then strikes the sample ionizing only those species which have been electronically excited. The entire experiment is performed in the neighborhood of the inlet optics to a quadrupole mass spectrometer. This extraordinary technique provides spectroscopic data for clusters of a single size. In a sense, it represents the ultimate cluster experiment.

The additional ability to use sub-nanosecond and picosecond (that is less than 10^{-9} to 10^{-12} sec) laser pulses of known and of variable frequency is being used in the study of the dynamics of many systems, including cluster systems. This very powerful technique will provide the ability to study the dynamic, state-to-state changes in clusters.

Summary and prospects for the near future

The existence of matter in small aggregates or clusters is seen to arise in a great variety of important scientific studies and engineering applications. With the advent of new quantum theoretical methods to calculate the physical properties of systems with up to 30 atoms, the extremely rapid advance in laser physics and optics, the recent incorporation of micro-processors into multi-channel

detection instrumentation with the capability for single photon or single particle pulse counting, and the progressively easier and less expensive access to computers for both theoretical and experimental uses, a near explosion of activity in this fascinating and important area of small cluster research has begun.

Acknowledgments

The author would be remiss were he not to acknowledge the fine work and contributions of his co-workers, currently consisting of B. G. DeBoer, S. S. Kim, O. Abraham, and J. H. Binn. He is also pleased to acknowledge those lifeblood associations essential for university research, that of the financial support obtained from research grants and contracts, specifically in our case from the Power Branch of the Office of Naval Research and the Engineering Energetics Program of the National Science Foundation.

References

1. C. Morozumi and H. C. Ritter, *Acta Cryst.* **6**, 588, 1953.
2. J. J. Burton, *Cat. Rev. Sci. Eng.* **9**, 209, 1974.
3. J. Farges, B. Raoult and G. Torchet, *J. Chem. Phys.* **59**, 3484, 1973.
4. J. Farges, M. F. de Feraudy, B. Raoult and G. Torchet, *J. de Phys. Colloque C2*, **36**, C2-13, 1975.
5. J. A. Armstrong and G. D. Stein, *J. Chem. Phys.* **58**, 1999, 1973.
6. C. L. Briant and J. J. Burton, *J. Chem. Phys.* **63**, 2045, 1975.
7. J. K. Lee, J. A. Barker, and F. F. Abraham, *J. Chem. Phys.* **58**, 3166, 1973.
8. R. W. Bolander, J. L. Kassner, Jr. and F. F. Zung, *J. Chem. Phys.* **50**, 402, 1969.
9. S. S. Lin, *Rev. Sci. Instr.* **44**, 516, 1973.
10. J. Q. Searcy and J. B. Fenn, *J. Chem. Phys.* **61**, 5282, 1974.
11. A. Yokozeki and G. D. Stein, *J. Appl. Phys.* **49**, 2224, 1978.
12. A. Yokozeki, *J. Chem. Phys.* **68**, 3766, 1978.
13. R. F. Smalley, D. H. Levy and I. Wharton, *J. Chem. Phys.* **64**, 3266, 1976.
14. G. A. Ozin and H. Huber, *Inorg. Chem.* **17**, 155, 1978.
15. A. Hermann, S. Lentwyler, F. Schumacher and F. Wöste, *Chem. Phys. Lett.* **52**, 418, 1977.

More general or extended references that may shed additional light on the subject at hand are "Molecular Metal Clusters" by E. I. Muettterties, *Science*, Vol. 196, p. 839, 1977; *Homogeneous Nucleation Theory* by F. F. Abraham, Academic Press, New York, 1974; *The Architecture of Molecules* by I. Pauline and R. Hayward, W. H. Freeman Co., San Francisco, 1964, and "Gasdynamics of Expansion Flows with Condensation, and Homogeneous Nucleation of Water Vapor" by P. P. Wegener, *Nonequilibrium Flows*, Vol. I, P. P. Wegener, Ed., Marcel Dekker, Inc., New York, 1969.

PRODUCTION AND ELECTRON DIFFRACTION STUDIES
OF SILVER METAL CLUSTERS IN THE GAS PHASE

B. G. DeBoer and G. D. Stein

submitted to Surface Science

PRODUCTION AND ELECTRON DIFFRACTION STUDIES
OF SILVER METAL CLUSTERS IN THE GAS PHASE

by

B.G. De Boert† and G.D. Stein*

Northwestern University
Department of Mechanical
and Nuclear Engineering
Gasdynamics Laboratory
Evanston, IL 60201

ABSTRACT

Silver is evaporated into an inert gas flowing at pressures between 0.1 to 3 torr and nucleates to form clusters in a size range of 40 to 110 Å. This two-phase mixture flows through a two stage molecular beam into a modified electron microscope. Electron diffraction patterns are taken in the cluster beam and analyzed using the bulk, face center cubic unit cell in conjunction with a twelve beam multiple scattering program. Deviations from the bulk structure are seen and are larger for smaller cluster size. Several possible interpretations are discussed. The effect of different carrier gases on oven performance and cluster size is also presented.

* to whom correspondence should be addressed

† present address : GTE Products Corp. 60 Boston St., Salem,
MA 01970

INTRODUCTION

The objective of this study is to obtain information on the structure of small clusters of metal atoms, prepared by evaporation into a low pressure inert gas, by analysis of their electron diffraction patterns. Potentially large effects of supporting substrates upon the clusters' structures were avoided by employing the quenching gas as a carrier to transport the clusters through a differentially pumped gasdynamic system (forming a "molecular" beam) into a high vacuum region where the electron diffraction pattern can be recorded⁽¹⁾. A necessary subsidiary goal is to discover conditions which produce sufficiently dense metal cluster beams so that electron diffraction patterns can be observed

EXPERIMENTAL

The metal cluster generator has been described previously⁽¹⁾ and is schematically illustrated in Fig. 1. This oven cluster source has been mounted into one part of the "diffraction chamber" of an Hitachi HU-11A/B which is operated as an electron beam source (condenser lenses only used). The electron microscope has been modified with the addition of a coarse aperture just above the cluster source and additional pumping capacity from a 15 cm diffusion pump with 1,000 /sec. It is connected to the diffraction chamber directly opposite the

oven. Electron diffraction patterns are recorded on glass photographic plates.

The metal vapor source used was a small helix, hand-wound tungsten wire (0.38 mm diameter) into which one or more small ingots, formed from 99.999 % silver, are inserted. The amount of silver in each charge is estimated to be in the range 0.1 - 0.25 g. The gas inlet tubing was shortened so that it now discharges through the heater rather than between heater and N_1 as shown in Fig. 1. Pressures measured at various points, with gas flow on but power oven off, are recorded in Table I together with the pressure ratios across the copper inlet tube and across nozzles N_1 and N_2 . Except for the lowest pressure with helium, which is outside the range of operating conditions actually used, these pressure ratios are low enough to cause "choked", sonic, constant mass flow rate through both N_1 and N_2 . However, even though there is a low pressure ratio across the inlet gas tube, the flow is everywhere subsonic. For steady isentropic flow from the tube exit to N_1 the larger tube exit area (1.5 mm diameter vs. 0.81 mm for N_1) requires subsonic flow at the tube exit with a Mach number between 0.14 and 0.2. With viscous effects this Mach number is even lower. The flow transit time for a monatomic gas is calculated to be ca. 0.5 sec for the oven chamber. The second orifice, N_2 , measures (0.51 mm in diameter. With both orifices choked only one-fifth to one-eighth of the carrier

gas exits via N_2 . A somewhat higher proportion of the metal clusters ought to pass through N_2 and the electron beam, because of their much greater "molecular" weight (4×10^4 to 2×10^6).

Diffraction patterns, if observed at all, are commonly visible for only about 10 seconds, and never for more than about 90 seconds. We were clearly not operating the oven under steady-state conditions, although they were constant over the time span of an exposure for film recording of a pattern (i.e., fraction of a second). The oven gas pressure and temperature, P_o and T_o , along with other experimental information, are summarized in Table II.

Exposed plates are developed in the usual manner and their degree of blackening is quantified by scanning across a diameter of the diffraction pattern with a recording microdensitometer. Patterns from three plates are presented in Fig. 2. Peak spacings (diffraction ring diameters), peak widths, and peak heights are all measured from these densitometer records. Calibration of spacings and minimum peak widths is obtained by tracing the patterns obtained from a commercial aluminum diffraction standard. Unit cell dimensions are derived from ring radii using the expression

$$a = L\lambda \sqrt{h^2 + k^2 + l^2} / (r(1 - 3r^2/8L^2)) \quad (1)$$

where $L\lambda$ is a "camera constant" determined from the aluminum standard, $\lambda = 0.053551 \text{ \AA}$ for the 50 Kev electrons, and $L = 47.13 \text{ cm}$. The term in $(r/L)^2$ is a small flat-plate correction. Cluster diameters, D , are estimated from peak widths using

$$D = L\lambda / \sqrt{W^2 - W_0^2} \quad (2)$$

where W is the observed peak width and W_0 is the "instrument broadening" taken to be the peak width found for the aluminum standard. Peak heights were taken to be proportional to the diffracted power in each peak and are corrected for the non-linear response of the plates. Estimated standard deviations are assigned to each intensity, σ_{obs} , and multiplied by the same correction factors. It should be emphasized that only diffraction patterns strong enough to be seen by eye on the phosphor screen were recorded.

RESULTS AND DISCUSSION

Source performance

In addition to varying gas pressures and filament temperatures, in search of optimum conditions for the production of high densities of smaller clusters, we also explored the effect of changing the carrier gas. Argon and helium show differences reflecting their differing atomic masses and collision cross sections^(2, 3). Past experience with nucleation studies indicate that a larger number of smaller clusters

should result from a more rapid cooling of the hot metal vapor⁽¹⁾. The chemically inert molecular gas, sulfur hexafluoride SF_6 , with its many internal degrees of freedom, i.e., its much larger heat capacity per molecule should be a more effective third body in the early stages of cluster formations. Since silver has a relatively small affinity for oxygen, CO_2 was also successfully used as a carrier gas.

A greatly increased production of silver clusters is observed using molecular gases. This occurs at substantially lower filament temperatures (i.e., lower vapor pressures) as indicated in Table II. Silver deposits on the oven liner were collected on microscope grids. Electron diffraction patterns for these samples verified the metallic silver structure with no evidence for compounding due to possible molecular gas decomposition.

An argument was made in an earlier paper⁽¹⁾ for a relationship between cluster size and the product of oven pressure, P_o , times the temperature of the evaporating metal sample, T_{om} . The results are presented in Fig. 3.

Both employed the same cluster generator seen in Fig. 1 and, whereas the prior investigation used one carrier gas (Ar) and several metals (In, Bi, and Pb), this work is for one metal (Ag) and several carrier gases (Ar, He, CO_2 and SF_6). It is

seen that all the results with the filament source are self-consistent with the heavier gases producing a given cluster size as progressively lower $P_{O_2} T_{om}$. The results for Pb in a boron nitride crucible required a greater $P_{O_2} T_{om}$ for a given cluster size, but operated for a longer time before the metal sample was depleted.

Diffraction Analysis

From the electron diffraction patterns, one easily obtains crystalline unit cell dimensions and crystallite sizes from the diffracted rings' diameters and breadths, respectively. However, more detailed atomic scale information is contained in the relative intensities of the rings. This information may be extracted by matching the intensities calculated from a model to the observed intensities. However, the calculations leading from model to diffracted intensities are more complex in the case of electron scattering than for X-rays or neutrons because of multiple scattering or "dynamical" effects. These effects are large enough to cast doubt upon any such analysis based upon simpler kinematic (or the first-approximation, Blackman-formula⁽⁴⁾) calculations⁽⁵⁾. Accordingly, a computer program has been written which calculates the diffracted intensities in as complete and correct a manner as time and budget permitted. An example for silver is shown in Fig. 4, normalized to the (311) reflection. If the scattering were kinematical the curves would all be horizontal with the value at

$D_t = 0$. Variations from (311) (also varying) by a factor of 2 to 3 can be seen at large D_t .

The corrected peak-height data obtained from the plates listed in Table II are used as input to the computer program. The best fitting cluster diameter D_t and root mean square amplitude of thermal vibration \bar{U} are included in Table II. Also listed are the (dis)agreement factors R_M and R_K , for the multislice and kinematic calculations respectively. These are defined as

$$R = [(\sum (I_{obs} - I_{calc})^2 / \sigma_{obs}^2) / \sum (I_{obs} / \sigma_{obs})^2]^{1/2} \quad (3)$$

In every case R_M is an improvement over R_K , but it must be pointed out that R_K is calculated using the value of \bar{U} optimized for R_M .

If this model and calculation are to be deemed successful, strong correlation between several quantities in Table II should be seen. For example higher temperature clusters should have greater \bar{U} and for a given size, D_t and D_e should agree. The above do not seem to correlate, although the goodness of fit R_M does vary with size D_e in a systematic way as shown in Fig. 5. The best agreement occurs for the largest clusters.

The variation, between the experimental and theoretical, 12-beam multiple scattering calculations, for each diffraction peak is seen in Fig. 6. The goodness of fit is clearly better as cluster size increased from top to bottom (these three experiments lie on the upper dotted curve in Fig. 5). The most prominent and consistent features are the larger (111) peak and smaller (400) similar to Ref. 5 (Pb clusters).

A variety of interpretations, other than the bulk fcc structure, have been considered qualitatively but have one or more features that do not fit the observations. They include the combined fcc plus liquid model⁽⁵⁾, stacking faults and twinning between fcc regions, decahedral (pentagonal bipyramid) and icosahedral sphere packing models^(6,7), and the presence of vacancies.

We have obtained improved agreement between observed and calculated intensities, but it appears that a simple cubic-closest-packing model of the silver metal clusters studied here is not correct. It may be that a partially liquid or amorphous structure is correct, but this has not been demonstrated conclusively. Single-phase (homogeneous) models other than fcc can be tested with the multi-beam computer program by replacing one subroutine.


ACKNOWLEDGEMENTS

We are pleased to thank Mr. K.C. Owen for some oven operating measurements used in Table II, and the Chemistry and Power Branches of the U.S. Office of Naval Research, and the National Science Foundation for partial financial support.

REFERENCES

- 1) A. Yokozeki and G.D. Stein, J. Appl. Phys. 49 (1978) 2224.
- 2) C.G. Grangvist and R.A. Buhrman, J. Appl. Phys. 17 (1976) 2200.
- 3) N. Wada, Jpn. J. Appl. Phys. 6 (1967) 553.
- 4) M. Blackman, Proc. R. Soc. (London) Ser. A 173 (1939) 68.
- 5) A. Yokozeki, J. Chem. Phys. 68 (1978) 3766.
- 6) C.Y. Yang, J. Cryst. Growth 47 (1979) 274.
- 7) K. Heinemann, M.C. Yacaman, C.Y. Yang and H. Poppa, J. Cryst. Growth 47 (1979) 177.

TABLE I
Oven Operating Pressures a)

Gas	Inlet ^{b)} P_{oo} torr	P_o/P_{oo}	Oven P_o torr	P_1/P_o	First Pumping Chamber ^{c)} P_1 torr	P_2/P_1	Second Pumping Chamber ^{d)e)} P_2 torr
He	2.99	0.10	0.30	0.53	0.16	$\leq 5 \times 10^{-5}$	$\leq 1.6 \times 10^{-5}$
He	7.22	0.14	1.01	0.36	0.36	$\leq 5 \times 10^{-5}$	
He	9.92	0.16	1.56	0.32	0.51	$\leq 5 \times 10^{-5}$	
Ar	3.07	0.14	0.44	0.40	0.18	$\leq 5 \times 10^{-5}$	
Ar	5.62	0.18	1.03	0.30	0.31	$\leq 5 \times 10^{-5}$	
CO ₂	2.88	0.17	0.48	0.38	0.19	$\leq 5 \times 10^{-5}$	

- a) Gas supply at room temperature (22°C) and oven power off.
- b) Measured at inlet of supply tube 10 cm long and 1.5 mm inside diameter.
- c) The opening or nozzle between the oven and the first pumping chamber has $N_1 = 0.81$ mm.
- d) The opening between the first and second pumping chambers has $N_2 = 0.51$ mm with a separation between nozzles of 4.3 mm (see Ref. 1 for additional details).
- e) Measured over the 15 cm baffle and diffusion pump.

TABLE II
SUMMARY OF EXPERIMENTS AND THEORETICAL COMPARISONS
(Silver Clusters in Various Carrier Gases)

Experiment and Plate No.	Oven Conditions				Diffraction Information						
	Carrier Gas	P _o torr	T _o K	Watts	T _{om} K	a Å	b) D _e Å	c) D _e Å	d) U _t Å	R _m %	R _k %
6	He	1.28	625	55	1500	4.078	43	37	0.13(5)	10.2	18.0
7		1.28	625	55	1500	4.079	56	-	--	--	--
13		2.90	530	100	1300	4.058	56	37	0.08(12)	14.9	22.3
14		2.90	530	100	1300	4.059	60	50	0.09(4)	15.2	24.7
15		2.90	530	100	1300	4.066	74	-	--	--	--
16*		3.2	545	140	1500	4.066	53	42	0.18(3)	16.6	24.2
8	Ar	0.51	770	50	1300	4.085	72	-	--	--	--
9		0.51	770	50	1300	4.089	72	-	--	--	--
10		0.60	760	45	1300	4.085	68	-	--	--	--
3		1.54	695	50	1300	4.095	69	7	0.15(2)	6.2	9.3
4	CO ₂	1.54	695	50	1300	4.091	69	280	0.14(2)	8.7	17.4
38		0.27	625	~30	1100	4.080	46	-	--	--	--
39		0.27	625	1	1100	4.063	50	10	0.17(4)	18.1	21.9
40		0.31	620		1500	4.091	60	-	--	--	--
30*	SF ₆	0.55	720		not observed	4.090	30	60	0.15(6)	32.0	39.0
33		0.36	620	~30	1100	4.075	66	180	0.10(7)	11.0	21.6
34		0.36	620	30	1100	4.072	57	-	--	--	--
35		0.37	600	25	1300	4.076	63	-	--	--	--
36		0.37	600	25	1300	4.084	82	-	--	--	--
21		0.37	625	30	1200	4.059	80	260	0.19(2)	11.8	49.9
22*		0.73	625	30	1200	4.065	110	100	0.10(3)	8.7	21.4

- a) During an experiment the oven temperature was observed by eye and use made of a calibration with an optical pyrometer, viz : Red-Yellow \approx 1100, Yellow \approx 1200, Yellow-White \approx 1300, and White \approx 1500 K.
- b) Diameter D_e is from experimentally measured ring widths.
- c) Diameter D_t is from theoretical best fit to multislice calculations.
- d) Root mean square amplitude of vibration is from multislice calculations with error \pm in parenthesis.
- e) Agreement parameter is from the best fit multislice calculation of peak intensities.
- f) Agreement parameter is from the theoretical kinematic calculation of peak intensities.

FIGURES

Fig. 1. Schematic diagram is shown for the metal cluster generator with TC - thermocouple, W - prism mirror window, H - heater for metal vaporization, S_1 and S_2 - sets of screws for configuration adjustments, CG carrier gas, N_1 and N_2 - flow orifices or nozzles.

Fig. 2. Microdensitometer tracings of Experiments 16, 22 and 30 (see Table II) are plotted with O.D. the optical density, $\log_{10}(I/I_0)$ and $S = 4\pi\lambda^{-1}\sin(\theta/2)$. Plate 30 is displaced 0.5 O.D. for clarity with Miller indices shown.

Fig. 3 Experimental cluster size D_e , as a function of oven pressure and temperature is determined using Eq. (2) for several metals and carrier gases with F-filament source and C-crucible source.

Fig. 4 Theoretical Ag cluster Peak intensities are normalized to the(311)peak and plotted as a function of Diameter D_t .

Fig. 5 The goodness of fit R_M is seen to improve as size n increases.

Fig. 6 A detailed comparison, peak by peak, for the observed and calculated Intensities is plotted vs. S^2 with Miller indices indicated.

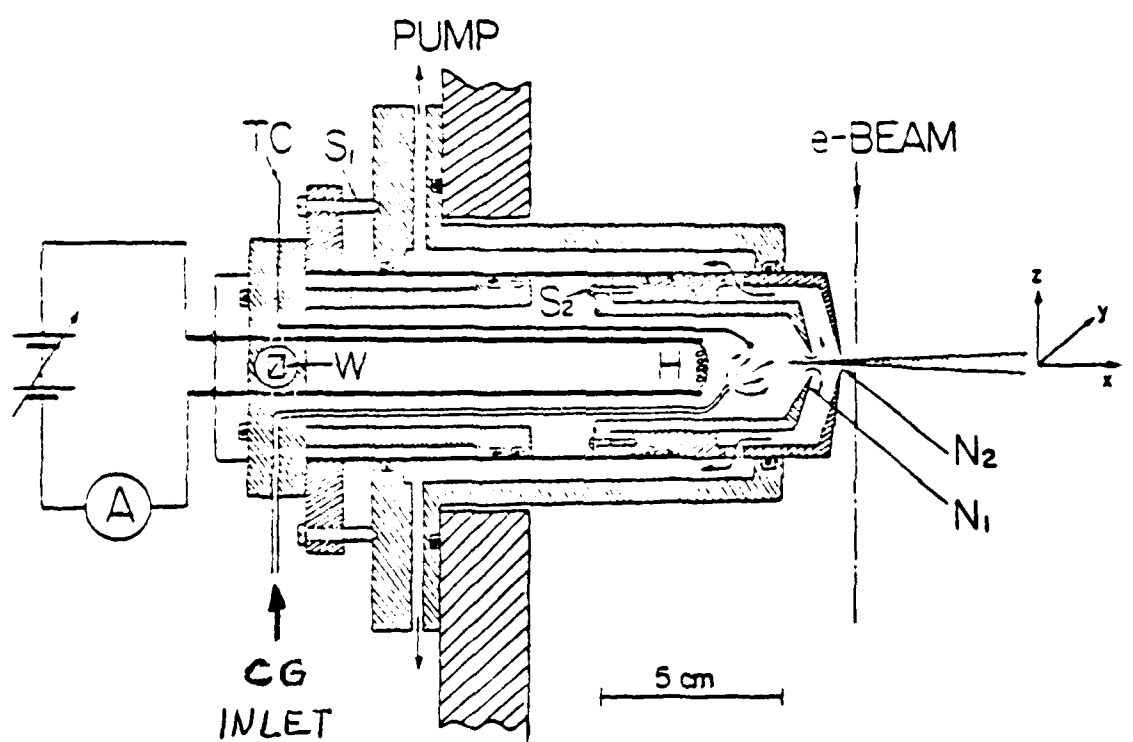


Figure 1

Fig. 2

16

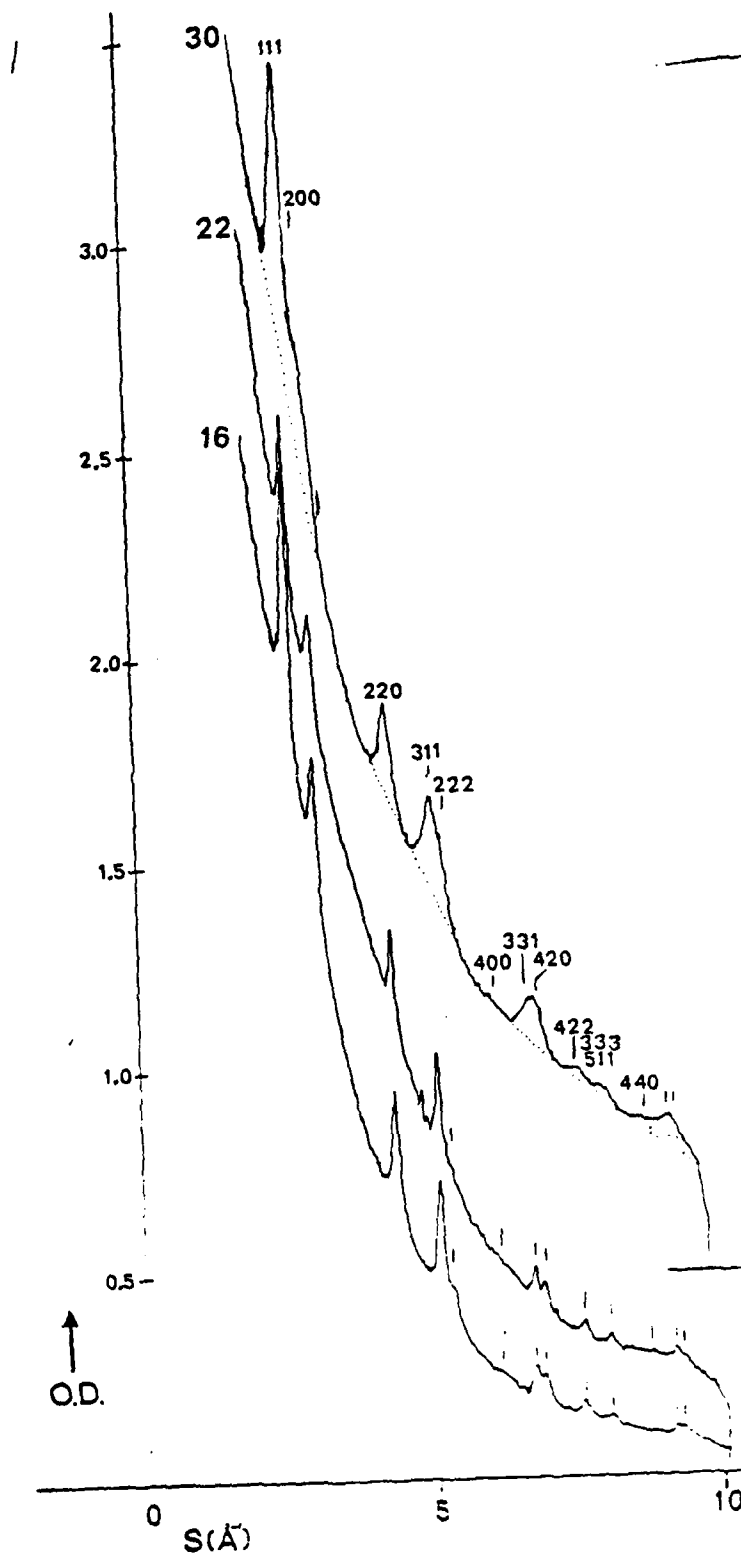


Figure 2

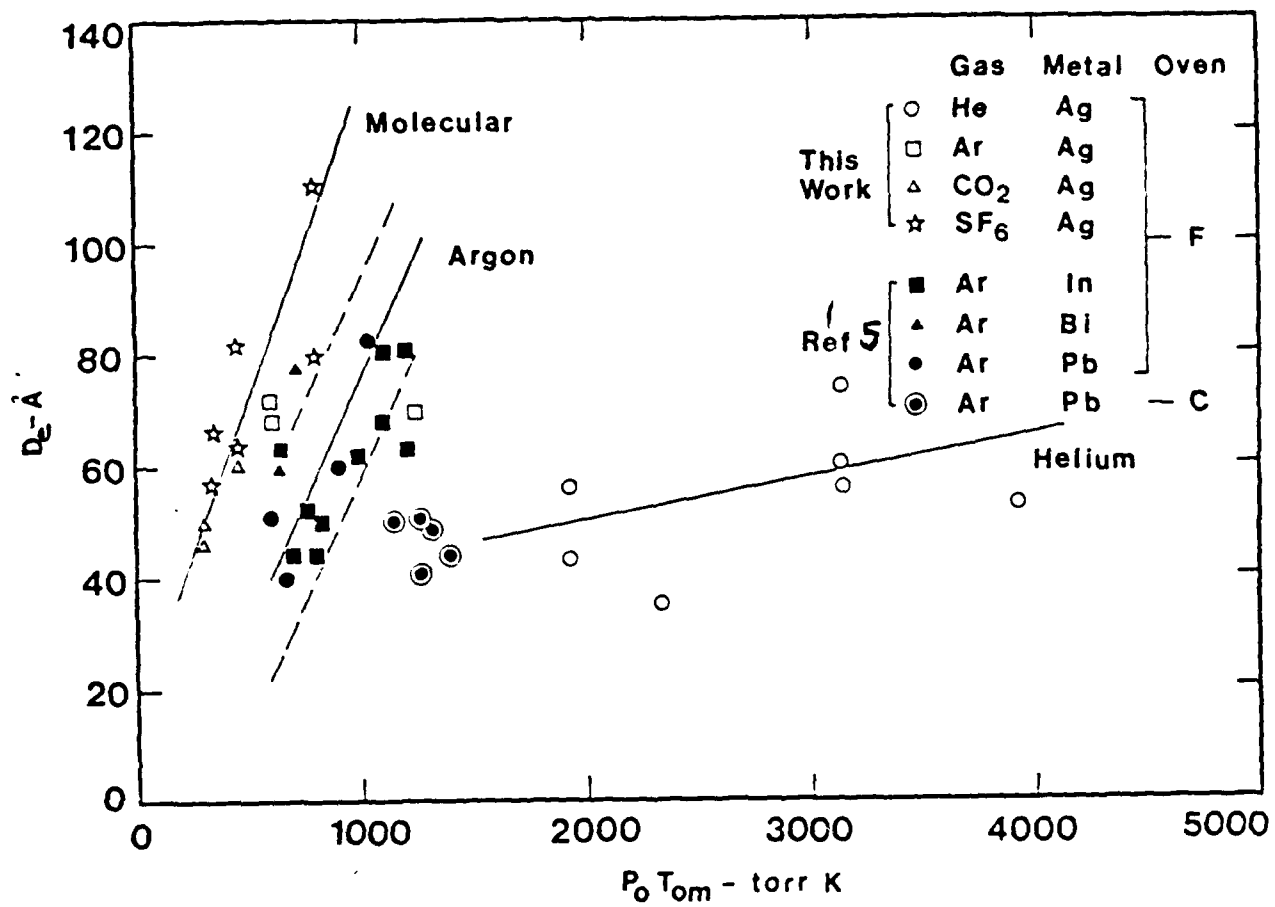


Figure 3

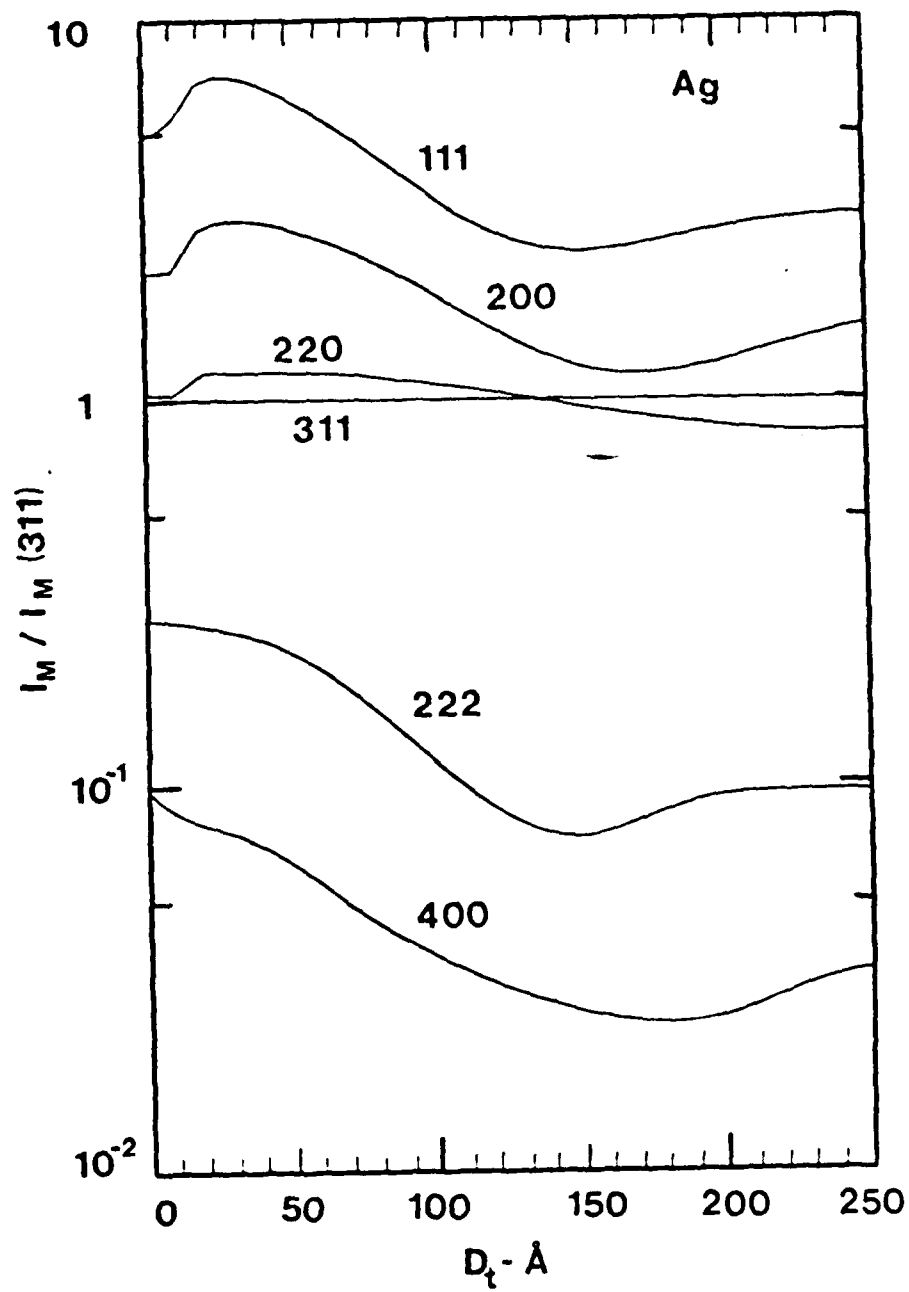


Figure 4

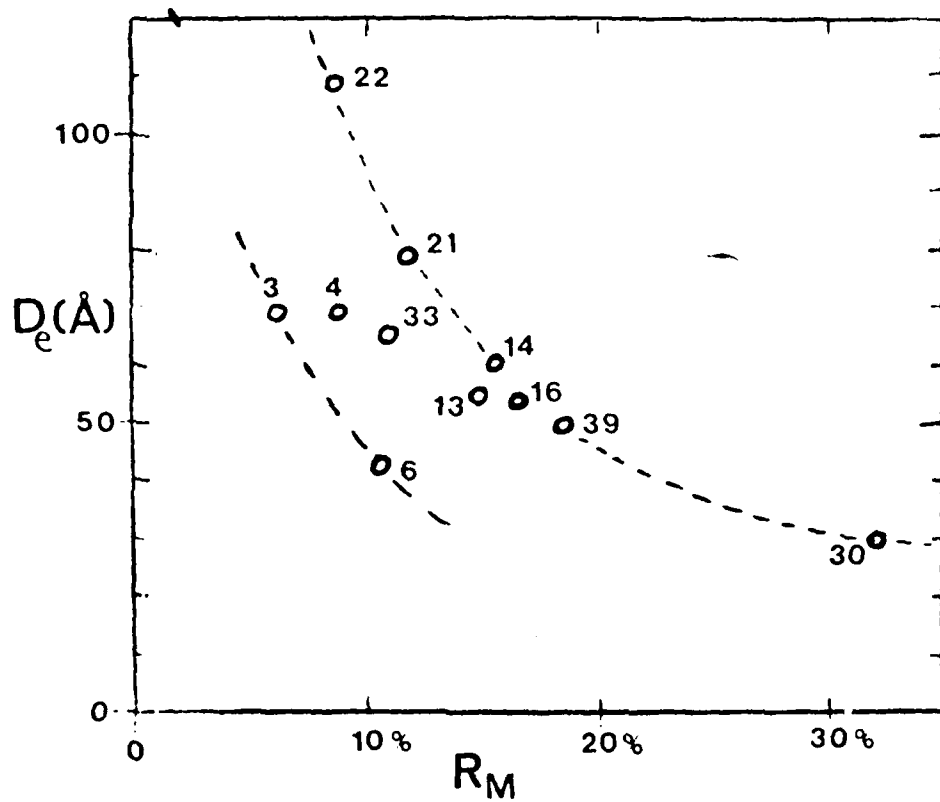


Figure 5

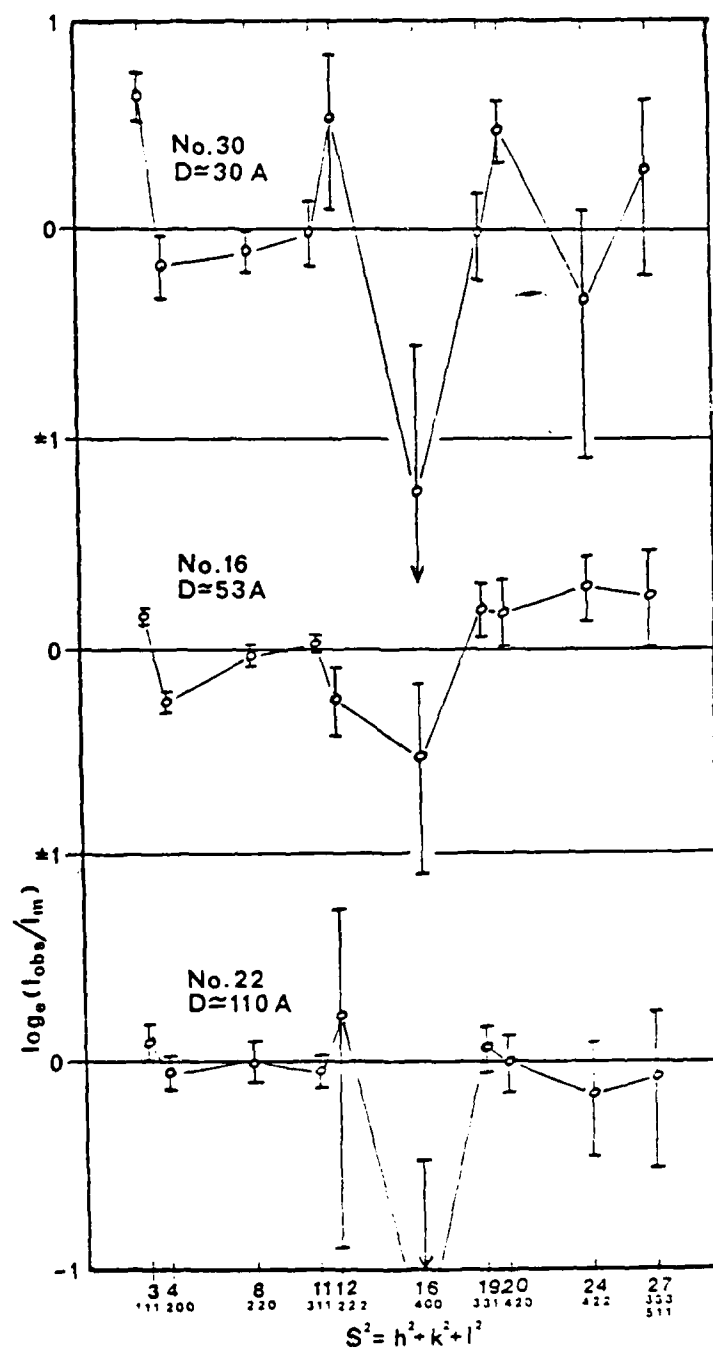


Figure 6

EVIDENCE FOR MIXED CLUSTERS FORMED DURING SULFUR HEXAFLUORIDE
EXPANSIONS IN AN ARGON CARRIER GAS

S. S. Kim and G. D. Stein

to appear in the Journal of Applied Physics

EVIDENCE FOR MIXED CLUSTERS FORMED DURING
SULFUR HEXAFLUORIDE EXPANSIONS IN AN ARGON CARRIER GAS

by

Sang Soo Kim and Gilbert D. Stein^{a)}

April 19, 1980

ABSTRACT

Nucleation of sulfur hexafluoride in an argon carrier gas has been studied in very small, supersonic, adiabatic nozzle expansions. Light scattering is used to detect the onset of condensation and high energy electron diffraction is used to ascertain cluster structure for a range of operating conditions where mixed clusters and/or binary nucleation can occur. For the limited range in SF_6 mole fraction, $x_0 = 0.01$ to 0.03 , both the thermodynamic and cluster diffraction data indicate that the SF_6 nucleates homogeneously with Ar accruing onto the condensed SF_6 after the Ar supersaturates.

Studies of sulfur hexafluoride (SF_6) cooled in adiabatic expansions have been undertaken in numerous research laboratories due to its relevance with regard to isotope separation schemes employing UF_6 and as the now-standard example for the study and illustration of multi-photon absorption phenomena. We have evolved a multi-faceted approach to the study of SF_6 phase change involving gasdynamic studies and theoretical comparisons using the governing equations of motion¹, laser scattering experiments to monitor nucleation and growth², molecular beam investigations to ascertain the important operating parameters with regard to making intense cluster beams³, and high energy electron diffraction for probing cluster size, temperature and structure. The purpose of this communication is to relate an unusual diffraction experiment and the conditions under which we believe that mixed clusters of SF_6 and Ar are formed.

The experimental apparatus consists of a conventional, three-stage, differentially pumped molecular beam which enters a scattering chamber where it is crossed by a 40 KeV electron beam. The diffraction patterns are obtained using film in a variable shutter arrangement known as a rotating sector.^{4,5} However small Laval nozzles are used in place of the usual orifice free jet source. Nozzle 7 is made from glass capillary tubing and has a throat diameter $D^* = 0.13$ mm, exit diameter $D_e = 2.0$ mm, and a length of 2.5 cm (see Ref. 1 for details). Previous experiments³ were used to ascertain the range of operating parameters required to produce SF_6 cluster beams. They showed that SF_6 mole fractions in the range $\chi_{\text{SF}_6} = 0.03-0.125$ were best suited for these studies.

Diffraction patterns are shown in Fig. 1A for $\chi_{\text{SF}_6} = 0.0$ (pure Ar), 0.018, 0.032, and 0.125 and denoted as Exps. A through D respectively. The Ar pattern is face centered cubic (FCC) having a unit cell parameter $a \approx 5.4$ Å. The Miller indices for body centered cubic (BCC) SF_6 are shown in Exp. D yielding a unit cell dimension of $a \approx 5.8$ Å. All these experiments are conducted with the same nozzle and operating conditions with only mole fraction varied. The scattering parameter is $s = (4/\lambda)\sin(\theta/2)$ where λ is the electron wavelength and θ is the scattering angle. The pattern for Exp. B has only the 110 peak for SF_6 while Exp. C has some features of a superposition or linear combination of Exp. A and D, especially at small s . However at other angles this does not appear to be the case.

In order to understand the process of formation for the condensed species the conditions for the onset of nucleation for SF_6 (solid symbol)

and Ar (open symbols) are shown in phase diagram Fig. 1B. The $\chi_{SF_6} = 0.01$ to 0.03 onsets are shown here for comparison with Exp. B and C. The cooling rate, for nozzle expansions, increases with decreasing throat size. Onsets of condensation plotted here for both large⁶ and small nozzles¹ (e.g. Nozzle 7) have been obtained using light scattering. Note that two of the small nozzle onsets for SF_6 cross the Ar vapor-solid equilibrium line. The corresponding Ar partial pressures reveal that the Ar is also supersaturated, $S > 1$ ($S = (p_v/p_\infty)_T$ where p_v is partial pressure of the species in question and p_∞ is the equilibrium pressure at the same temperature T).

Lines of constant undercooling ($\Delta T_p = (T_\infty - T)_p$ where T is the temperature of the gas and T_∞ the vapor-solid equilibrium temperature at the same pressure) are included for the Ar equilibrium line. The onsets of Ar nucleation are for a large nozzle⁷ in a helium carrier gas having $\chi_{Ar} = 0.01$ to 0.06, plus one pure Ar. Note that they all fall along the line $\Delta T_p \approx 20$.

The conditions at the exit of Nozzle 7 for Exp. A-D are shown as the partially solid symbols and corresponding open symbols for theoretical solutions of the equations of motion with phase change and viscous effects.¹ Note that exit conditions for Exp. B and C occur near the line $\Delta T_p = 20$, but this is not an onset condition since the clusters have grown to a size large enough to produce strong diffraction patterns. The theoretical solution for Exp. C predicts nearly all of the SF_6 to be condensed at the nozzle exit ($g_e \approx w_0$ or $C_e \approx 1.0$, see Table I). Within the nozzle at SF_6 onset the Ar is unsaturated ($S_{Ar} = 0.042$) and thus the nucleation process is homogeneous, i.e. pure SF_6 clusters. By the time the expansion has reached the $\Delta T_p = 20$ line, Ar has condensed onto the SF_6 clusters to such an extent that it is visible in the diffraction pattern. The homogeneous nucleation of Ar, as distinct cluster species from that of the SF_6 , must approach or exceed the $\Delta T_p = 20$ line before its nucleation rate can rise to a value high enough to provide enough surface for efficient depletion of the Ar vapor phase. Heterogeneous nucleation of Ar onto the SF_6 can potentially begin shortly after the Exp. C expansion crosses p_∞ for Ar. (The energy of formation for a cluster on a heterogeneous site is always lower than that for homogeneous nucleation.) The situation is similar for Exp. B except that it has a lower mole fraction χ_0 , lower fraction condensed $C_e = 0.379$ and therefore an even smaller mass fraction condensed at the exit, $g_e = 0.0244$ compared to 0.1075 of Exp. C.

A closer examination of Exp. C shows that the strongest reflection for SF_6 , the 110 peak, is still very prominent suggesting that the SF_6 crystal

structure is still largely intact. The strongest Ar reflection, 111, is easily discernible although unresolved from the SF_6 200 and is substantially smaller than the pure Ar 111 peak of Exp. A. Many peaks from Exp. A and D seem to appear in C as well but not as complete peaks or as linear superpositions. In particular the 220 peaks do not superimpose well. Thus there are some differences between that of pure Ar and pure SF_6 crystalline structures. Since the unit cell parameters typical of the pure species do not match up closely one may not expect epitaxial growth of the Ar onto the SF_6 . Perhaps there is a transition layer, amorphous in nature, separating the two. The diffraction pattern for Exp. B shows only one small SF_6 peak (110) with perhaps just a hint of the SF_6 200 unresolved with the Ar 200 and 111. This is consistent with the other patterns since the SF_6 mass fraction condensed is much lower than Exp. C.

One feature of these expansions which will in general discourage the formation of Ar condensate onto the SF_6 clusters is due to the SF_6 latent heat which must be carried away by Ar collisions before the cluster temperature can approach that of the gas. Estimates of cluster temperature obtained from electron diffraction data³ are higher than that of the gas by 30 to 50°C. The higher the mole fraction the greater this difference is expected to be. Thus even though the Ar can supersaturate at some point in these expansions, its condensation onto the SF_6 clusters is not insured. Perhaps this is the reason that these mixed clusters are seen so seldomly in these experiments.

The results of the work presented here may be summarized as follows:

- (1) The mixed cluster diffraction pattern, Exp. C, shows some features of the crystalline structure from both pure Ar and pure SF_6 and some features which can be ascribed to neither. Exp. B shows only one SF_6 peak.
- (2) The thermodynamic history for these supersonic adiabatic expansions reveals that the SF_6 clustered homogeneously at some point within the nozzle, crossed the Ar vapor-solid equilibrium line and most probably condensed Ar onto the surface of the SF_6 clusters. An undercooling $\Delta T_p \approx 20^\circ\text{K}$ is required for the onset of homogeneous Ar nucleation.
- (3) The SF_6 clusters are warmer than the ambient gas, and since a significant fraction of the condensed phase must be Ar if its diffraction peaks are to be seen above those of the SF_6 , the range of conditions necessary for the formation of mixed clusters is limited to $0.5 < x_{\text{SF}_6} < 1.0$.

- (4) For the case of the small nozzles, in which their operating conditions are adjusted so as to produce SF_6 nucleation near the exit, it is possible to have the Ar in the range $\Delta T_p \geq 20$ at which point Ar nucleation could also be initiated. Thus the possibility of a binary nucleation process arises. The growth of this heterogeneous cluster could produce diffraction patterns radically different from those reported in this investigation.

ACKNOWLEDGEMENTS

The authors are indebted to Dr. B. G. DeBoer for his help and suggestions. We would also wish to acknowledge the partial financial support for this research from the Engineering Energetics Program of the National Science Foundation and the Power Branch of the Office of Naval Research.

REFERENCES

1. O. Abraham, J. H. Binn, B. G. DeBoer, and G. D. Stein, unpublished.
2. O. Abraham, S. S. Kim, and G. D. Stein, unpublished.
3. B. G. DeBoer, S. S. Kim, and G. D. Stein, Rarefied Gas Dynamics,
R. Campargue, Ed. Commissariat a L'Energie Atomique, Paris, 1151 (1979).
4. P. Audit and M. Rouault, C. R. Acad. Sci. (Paris) 265, 1100 (1967).
5. G. D. Stein and J. A. Armstrong, J. Chem. Phys. 58, 1999 (1973).
6. B. J. C. Wu, P. P. Wegener, and G. D. Stein, J. Chem. Phys. 68, 308
(1978).
7. B. J. C. Wu, P. P. Wegener, and G. D. Stein, J. Chem. Phys. 69, 1776
(1978).
- a) Northwestern University, Gasdynamics Laboratory, Evanston, IL 60201.

CAPTIONS

Figure 1. Electron diffraction patterns are taken in a molecular beam from clusters formed in SF_6 -Ar mixture expansions with mole fractions that vary from 0.0-0.125. The molecular beam configuration (D_s the skimmer diameter, D_c the collimator diameter, stagnation pressure p_0 and temperature T_0) is the same for all these experiments. The vertical lines with arrows up locate the SF_6 BCC peaks and arrows down those of Ar FCC structure. In the phase diagram p_0 is the partial pressure of either the SF_6 or Ar as appropriate. The solid symbols are for SF_6 onsets of nucleation and the open symbols for Ar onsets. The SF_6 data is for $x_{\text{SF}_6} \approx 0.01$ to 0.03 for a variety of nozzles having different throat areas. The Ar partial pressure for the lower three SF_6 onsets (\boxtimes) indicate that the Ar is also supersaturated. The adiabatic expansion line is shown for Exp. A-D with the experimental and theoretical exit conditions indicated. Lines of constant undercooling, $\Delta T_p = 10$ and 20°C are shown for the Ar vapor-solid equilibrium line. The two solid lines with $\tau = 1$ and $\tau = 10^5$ are theoretical SF_6 onsets computed for the small nozzles², using the classical nucleation theory with τ a convection factor.

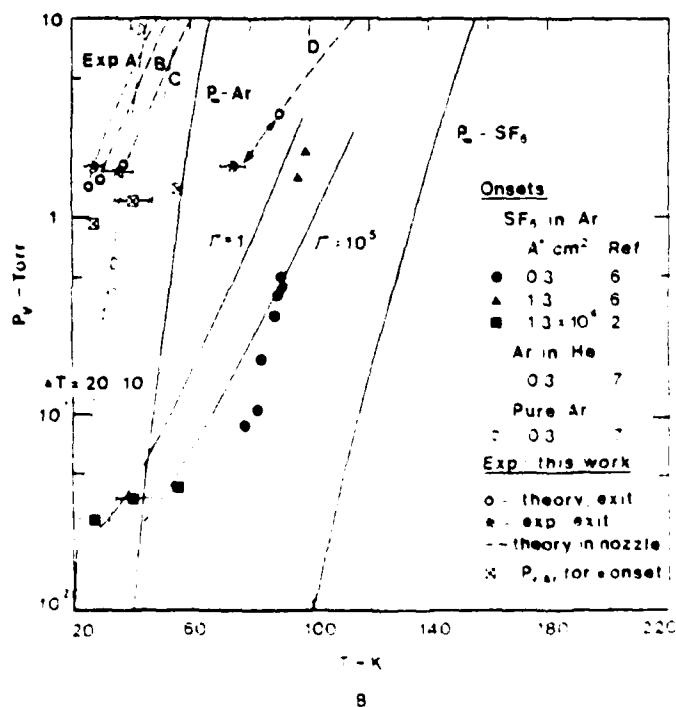
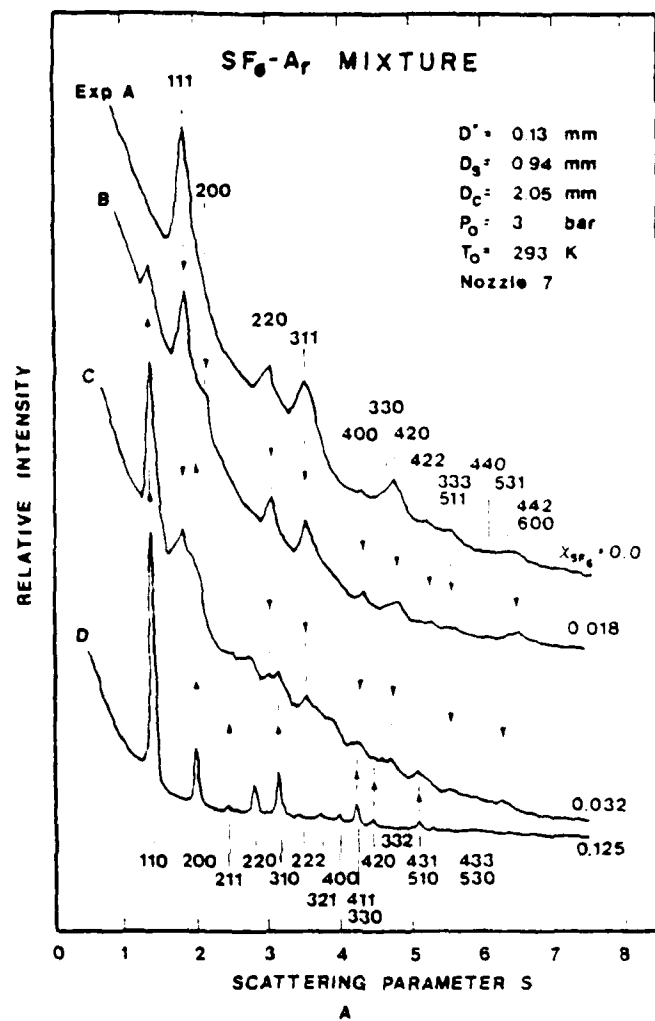
TABLE I
THERMODYNAMIC CONDITIONS

Exp	Inlet or stagnation chamber (experimental)			b) x _{cm}	SF ₆ onset (theoretical)			Exit (theoretical)				Exit (experimental)		
	P _{Ar} torr	T _{Ar} °K	χ _{Ar} a)		P _{Ar} torr	T °K	S _{Ar} -	P _e torr	T _e °K	g _e a)	C _e = g _e /w _e o	P _{SF₆} torr	P _e torr	T _e °K
1	3	293	0.0	0.0				1.39	25.8	0	0	0	1.75	27.7
2	3	293	0.018	0.0664	73.3	85.3	0.13	1.57	30.7	0.0244	0.379	1.76x10 ⁻²	not	taken
3	3	293	0.032	0.1080	119.9	103.0	0.039	1.65	33.4	.1075	0.995	3.45x10 ⁻⁴	1.70	34.7
4	3	293	0.125	0.3427	165.1	132.9	0.010	3.22	90.0	.3427	1.0	3.90x10 ⁻⁸	1.79	73.0

a) = 2.0 g's SF₆/gram mixture

b) = distance from nozzle inlet, nozzle length = 2.5 cm

c) = isentropic adiabatic flow



HOMOGENEOUS NUCLEATION OF SULFUR HEXAFLUORIDE CLUSTERS
IN LAVAL NOZZLE MOLECULAR BEAMS

O. Abraham, S. S. Kim and G. D. Stein

submitted to Journal of Chemical Physics

HOMOGENEOUS NUCLEATION OF SULPHUR HEXAFLUORIDE
CLUSTERS IN LAVAL NOZZLE MOLECULAR BEAMS

by

Oommen Abraham, Sang-Soo Kim and Gilbert D. Stein

Northwestern University
Gasdynamics Laboratory
Evanston, Illinois 60201

March 31, 1980

ABSTRACT

The condensation of SF_6 in Ar and He carrier gases has been studied in diverging Laval nozzles with throat diameters in the range of 0.1 to 0.2 mm. The clustering is detected using laser scattering, molecular beam intensity measurements and high energy electron diffraction. Although the nozzles have cooling rates in the 10^7 °C/sec range, the correction for nucleation lag time results in changes which are less than 15% from the steady state rate theory. For the 3% SF_6 in Ar the onset may enter the Ar supersaturation region with the attendant possibility for binary nucleation. Even though these expansions are not isentropic, due to nozzle wall boundary layers, they are nevertheless much more effective cluster sources than the "isentropic" free jet expansions. The onset of condensation is consistent with earlier results for much larger nozzles and agrees with the classical Volmer theory.

INTRODUCTION

The study and use of Laval nozzles for adiabatic, supersonic expansion of a condensable vapor is important both for many technological applications and fundamental investigations into the dynamics of condensation via homogeneous nucleation. Systematic investigations date back 60 years to the studies by Stodola of steam condensation in turbine nozzles.¹ Since then many other investigators have made contributions to this field for a wide range of condensable vapors.³⁻⁶ Recently there has been particular interest in condensing sulphur hexafluoride, SF_6 , expansions due to its similarities with UF_6 and a variety of proposed methods for gas phase isotope separation.⁷⁻¹¹ The use of very small Laval nozzles (throat diameter D^* in the range 0.025-0.25 mm) as cluster sources for molecular beams has been pioneered by the Karlsruhe group with current applications including fueling and heating of Tokamak fusion machines^{12,13} and cluster research.¹⁴⁻¹⁶ Investigations into the design and use of small Laval sources has been undertaken in our laboratory¹⁷ in order to understand and optimize their design for studies of the physical properties of small clusters using both high energy electron diffraction and tunable laser spectroscopy. The use of free jet sources for the above mentioned research techniques has been well established.¹⁸⁻²⁰ The purpose of the research reported here is to explore the SF_6 nucleation process in these small nozzles and compare ~~these~~ ^{the rate} to the theoretical predictions of the nucleation theory as incorporated into the governing equations of supersonic, adiabatic flow. ^{in these small nozzles} The ~~SE~~ ^{cooling} rates are in an interesting range, intermediate between those of large Laval nozzles in which the steady state nucleation theory is valid, and those of free jet molecular beam sources in which the cooling rate is considered by many researchers to be so rapid that the nucleation theory is no longer valid. The effects of nucleation on

time on the steady state nucleation theory and its impact on measurable properties will be discussed.

DESCRIPTION OF EXPERIMENT

The experimental arrangement is shown schematically in Fig. 1. The SF_6 is supplied from high pressure bottles of known mole fraction ~~XXXX~~ in either an argon or a helium carrier gas. (The SF_6 mole fractions required have previously been determined¹⁰). With measurement of the stagnation pressure p_0 , temperature T_0 and mass fraction ω_0 , the initial state of the gas before expansion is thus determined. The nozzle is installed in the stagnation chamber with a static pressure tap at the nozzle exit. The nozzle contours have been measured and the data fitted to a seventh order polynomial, see Table I for details. An argon-ion laser tuned to 514.5 nm with a 0.1 watt CW beam is focused over the nozzle centerline about 1.25 mm beyond the nozzle exit. A tube with 2 apertures of 1 mm diameter is connected to a fiber optic which exits the vacuum chamber and is terminated at an RCA 7850 photomultiplier tube. The nozzle exit diameter is 2.5 mm (2 mm for Nozzle 7) and the two apertures are located so as to cut off a scattering volume from the laser beam of about 1 mm length, i.e. a volume well within the nozzle exit flow field. When light scattering is not being used the double aperture is moved out of the way and the molecular beam skimmer moved up near the light scattering position thus skimming off the centerline flow. After a second stage of differential pumping the cluster beam enters a scattering chamber where it is crossed by a 40 KeV electron beam for diffraction studies. The cluster beam intensity is monitored with an ionization gauge detector. The electron diffraction patterns are measured with a single channel, electron scintillator, pulse-counting detection system. The cluster beam is modulated with a chopper located between skimmer and

collimator and synchronous detection (i.e. up-down counting) is used to eliminate background scattering. The single channel detector is programmed to accumulate signal for a given number of chopper cycles and is then stepped to the next increment in scattering angle θ and the process repeated until the entire diffraction pattern is taken. The total electron beam flux or current is monitored continuously using a Faraday cup inside the beam trap. The primary function of the diffraction apparatus is to record patterns for structure analysis of clusters, however in the work reported here it is used to estimate mean cluster size and temperature.

LIGHT SCATTERING AND MOLECULAR BEAM MEASUREMENTS

With the incoming laser beam polarized perpendicular to the 90° scattering detector (i.e. its electric field along the flow direction) the Rayleigh scattering intensity has been measured as the function of p_0 for a range of SF_6 mole fractions in Ar, 12.5% SF_6 in He, and pure Ar. This experimental sequence has been used for several nozzles, three of which are reported here and two are shown in Fig. 2. The differential scattering cross section per unit volume $(d\sigma/d\Omega)_v$ is defined as the average differential scattering cross section per particle $\overline{(d\sigma/d\Omega)}$ times the cluster concentration per cm^3 , N :

$$(d\sigma/d\Omega)_v = N \overline{(d\sigma/d\Omega)} = N \int_0^\infty (d\sigma/d\Omega) f(r) dr \quad (1)$$

where the average differential scattering cross section is obtained by integrating over a normalized size distribution $f(r)$. The cross section per unit volume is related to the incoming and scattered light intensities, I_0 and I_{90} , respectively and the scattering geometry by $(I_{90}/I_0) (4R^2/d_a^3) = (d\sigma/d\Omega)_v$ where d_a is the diameter of the aperture furthest from the laser beam and R is the distance from this aperture to the centerline. The differential

scattering cross section per cluster is the usual Rayleigh or dipole expression $(d\sigma/d\Omega) = \alpha^2 k^4 = [r^3 (m^2 - 1) / (m^2 + 2)]^2 (2\pi/\lambda)^4$ where α is the polarizability, k is the wave number $(2\pi/\lambda)$, m is the index refraction, and λ is the light wavelength. The operational definition for the onset of condensation is taken as the intensity as it rises above the background by 0.1 na, which translates to a value for $(d\sigma/d\Omega)_v$ of $2.8 \times 10^{-6} \text{ cm}^{-1}$. This condition for onset is shown in Fig. 2.

With the light scattering apparatus moved out of the way, the nozzle can then be moved toward the skimmer such that the molecular beam intensity is a maximum and the relative distance is close to that for the light scattering (3.25 mm from the exit). The unclustered beam intensities for this molecular beam geometric configuration is just discernible above the measured background ionization gage pressure. As p_0 is increased beyond 1.5 bar ($1 \text{ bar} = 10^5 \text{ Pa} \approx 1 \text{ atm}$) the intensity rises dramatically as a result of clustering in the nozzle.^{21,22} Since these intensity curves are nearly linear (See Fig. 3) the criteria for onset is taken as that pressure obtained from a linear extrapolation back to zero intensity. This criteria is virtually the same as taking a small intensity rise above background as done with the light scattering.

It should be noted however that the unclustered beam intensity can be seen above the background signal although the signal-to-noise level is low. In the laser detection method the unclustered flow, i.e. molecular scattering, cannot be detected due to the stray light intensity seen by the photomultiplier. Thus the molecular beam method is more sensitive than the light scattering arrangement in detecting the initial cluster build up.

SMALL NOZZLE TEMPERATURE MEASUREMENT

Since the small nozzle is used at pressures in the range

of 1-8 bar (high densities, really) the collision mean free path λ_{fp} is much less than the nozzle diameter, with the Knudsen number $Kn = \lambda_{fp}/D$ in the range of 10^{-3} - 10^{-4} even at the nozzle exit. Thus these flows are continuum or collision dominated. Typical Reynolds numbers for these flows are in the 10^4 range¹⁷ so that boundary layers are expected to be thin. Nevertheless since these nozzles have very small inlets of the order of 0.1 mm and very gradual divergence angles, the viscous boundary layer can extend to the centerline thus resulting in fully developed flow. (Only in the case of pure SF_6 expansions is there evidence of an isentropic core.¹⁷) Although isentropic flows are far simpler to deal with analytically, the importance of a more complete understanding of these small nozzle flows necessitates a non-isentropic analysis including the effects of viscosity and heat conductivity. Sufficient gasdynamic measurements have been made so that this more complicated analysis can be made and compared to experiment.

The details of the nozzle geometries used here are given in Table I and typical ranges in nozzle exit properties are shown in Fig. 4 for Nozzle 7. Two sets of curves are presented spanning the range of SF_6 mole fraction from 12.5% to 0% in Ar. The exit Mach number M_R increases with p_o leveling out for argon to a value of 5.5. At the same time the exit temperature drops with increasing p_o to values as low as 30°K and exit static pressures are in the range of 1-2 torr (133-266 Pa).

Cooling rates in geometrically similar nozzles scale with the nozzle throat diameter. For a given throat size the cooling rate is dependent on the variation in nozzle cross sectional area with position. The larger the spacial gradient in area the more rapid is the cooling rate. Typical cooling rates are shown in Fig. 5 for these cases: a nozzle with 1 cm diameter throat ~~XXXXX~~, Nozzle 7 from this work having a throat diameter of 0.125 mm, and a free jet expansion with its throat diameter also 0.125 mm. The

maximum cooling rate always occurs near the nozzle throat, $x = 0$, and is denoted by an asterisk. A typical onset of condensation is also noted. The thermodynamic conditions at onset are most important with regard to the nucleation process since it is near maximum here. The cooling rate at onset for the small Laval nozzle is about an order of magnitude higher than the larger nozzle. (There is some variation with specific heat ratio γ but it is not significant for the purposes of this discussion.) The free jet expansion is not controlled by solid boundaries as are those of the Laval nozzles and it thus represents a maximum cooling rate for a given gas and throat size. In Fig. 5 onset occurs at a cooling rate 40 times that of the Laval nozzle with the same size throat. If the cooling rate gets too high a variety of non-equilibrium processes set in. For example in free jet expansions studies have been made of non-equilibrium rotational, vibrational, and even translational effects.²³ Thus it is not surprising that there may be non-steady state effects for the nucleation process. For most nozzle flows with throats ≥ 1 cm and starting conditions \geq STP the steady state nucleation theory obtains, and there are negligible effects due to nucleation lag time.² ^{small} used in the present experiments The/nozzles/~~XXX~~ have cooling rates high enough that a time-dependent nucleation rate must be considered.

These flows may be assumed to be adiabatic with regard to the interface between the gas flow and the solid nozzle walls. However, from one point to another within the flow the temperature gradients may be high enough that heat conductivity from one part to another is not negligible. The effects of viscosity, for all of the experiments reported here reach to the centerline of the flow at some point in the nozzle. These combined effects result in exit Mach numbers which are lower than the ideal case, with pressures and temperatures which are higher than for isentropic expansions. The cooling of the gas is nevertheless quite substantial, producing very high supersaturation.

and resulting in efficient cluster nucleation and growth, i.e. compared to an isentropic free jet source at the same p_0 and D^* .

THEORETICAL CLUSTER FORMATION AND GROWTH

The effects of boundary layers and their growth to the centerline has been treated in a previous paper with the comparison to a variety of gasdynamic measurements.¹⁷ The governing equations for fluid flow, conservation of mass, momentum and energy; coupled with an equation of state; a nucleation rate law; and a droplet growth equation are used to predict all the thermodynamic properties throughout the nozzle including cluster size and concentration as nucleation proceeds. The nucleation rate expression employed is that of the so called classical theory,

$$J_{ss} = \Gamma \left(\frac{p_v}{kT} \right)^2 \left(\frac{2\sigma}{\pi m} \right)^{1/2} v_c \exp(-\Delta G^*/kT) \quad (2)$$

where J is the number of critical size clusters formed per second per cm^3 , and ΔG^* the Gibbs free energy of formation of the critical size cluster $\Delta G^* = 4\pi r^{*2} \sigma / 3$. The critical radius is given by the Gibbs-Thompson-Helmholtz equation $r^* = 2\sigma v_c / kT \ln(p_v/p_\infty)$. The saturation ratio is defined as p_v/p_∞ . p_v is the partial pressure of the condensable vapor, T is the temperature, p_∞ is the vapor-liquid (or vapor-solid) equilibrium pressure at the same T . k is Boltzmann's constant, σ is the surface tension, m is the mass of a single vapor molecule, v_c is the volume of a condensable molecule in the condensed phase and Γ is a correction factor used to match theory to experiment. The magnitude of the nucleation rate is very sensitive to surface tension (cubic in the exponential expression) which is unknown in the solid regime below the SF_6 triple point (222 K) but has been estimated from published data above the triple point^{33,34} as approximately 20 erg/cm^2 . The temperature dependence for the data above the triple point is incorporated

into the extrapolation below 222 K giving: $\sigma(t) = 6.77(4-T/80)$. The value of Γ is approximately 10^5 .

The theoretical predictions for the nucleation rate in Nozzle 7 is shown in Fig. 6 for a range of starting pressures and a mole fraction of 0.03 SF_6 in Ar. The time-dependent nucleation theory is shown as the solid lines. As p_0 is increased the point of maximum nucleation moves upstream in the supersonic portion of the nozzle and rises to a higher maximum value and falls off more quickly. As p_0 is decreased the maximum nucleation rate decreases by more than two orders of magnitude and spreads out in time or position through the nozzle by about one order of magnitude, thus resulting in a net cluster production or concentration which is down by an order of magnitude. The calculations are carried out for one value of boundary layer displacement thickness at the nozzle exit and a constant viscous dissipation factor ($\Delta = 0.6$ and $F_\mu = .0002$ in Ref. 17). Thus the family of curves do not follow the exact process in the nozzle as a function of p_0 , although it is close, but does illustrate the trends qualitatively, if not completely quantitatively.

The mass fraction condensed is g in grams SF_6 /gram of mixture, and is plotted in Fig. 7 for the same flow conditions as Fig. 6. When all of the SF_6 is condensed out $g_{\text{max}} = w_0 = 0.0987$ and this limit is reached before the exit of the nozzle when $p_0 \geq 4$. Note the very rapid rise in g at high p_0 , with the onset of condensation occurring sooner in nozzle (lower x) as p_0 is increased. For the growth of the clusters beyond the critical size the vapor condensation coefficient is taken as unity as usually done for condensation when the vapor is a small mole fraction in a carrier gas. If one defines the onset of condensation for these calculations as that point where g is equal to 1% of $g_{\text{max}} = w_0$, then the onset of condensation at the nozzle exit will occur for p_0 just below 1.8 bar.

~~cluster so that the predicted cluster concentration is calculated from the~~
~~high speed photography measurements for the onset of the condensation~~
~~process, then comparing this with the cluster concentration calculated~~
~~from the molecular beam measurements to agree with the high speed~~
~~photography.~~

The two most useful features of a droplet size distribution are the mean size and the droplet concentration. These quantities, designated \bar{r}_e and N_e at the nozzle exit, are shown plotted in Fig. 8. As expected the droplet concentration increases with p_0 due to the much higher peak nucleation rate as seen in Fig. 6. As p_0 increases past 1.5 bar, nucleation at the nozzle exit rises to a value where it begins to significantly deplete the vapor phase and the concentration $N_{e, \text{max}}$ begins to increase. The concentration N_e increases with SF_6 mole fraction as seen in previous results.⁵ The concentration N_e is the meaningful quantity when comparing to light scattering data since the detector views the scattering from a fixed volume of gas, independent of the pressure or density in the flow at that point.

The cluster concentration for 3% SF_6 is also shown plotted as a function of clusters per gram of mixture, N_{ge} . Beyond $p_0 = 4$ bar N_{ge} decreases even though the peak nucleation rate increases by a factor of 4 as p_0 goes from 4 to 7 bar. The nucleation rate is shut off more quickly at higher densities due to more efficient droplet growth. The total number of clusters formed per cubic centimeter (the area under the J vs. x Figure) still increases with p_0 but not as rapidly as the flow density increases. Thus N_{ge} decreases. The maximum in N_{ge} occurs at the approximate pressure for which all of the SF_6 is predicted to condense from the vapor.

The mean cluster radius at the exit increases with increasing p_0 and also with increasing mole fraction of SF_6 . Note also that even while the clusters grow to significant size before the onset of condensation, concen-

trations in this early part of the flow are so low that they are not seen in the light scattering apparatus. From the electron diffraction experiments it has been determined that the cluster structure, like the bulk, is body-centered cubic with two molecules per unit cell and a unit cell dimension of about 5.8 Angstroms. Thus the droplet radius can be converted to number of molecules per cluster, G , and is also shown in Fig. 8A. Notice at the higher values of p_0 the cluster size varies from 5×10^4 for 3% SF_6 up to 1.2×10^6 for the 12.5%. These are very large clusters so that if clusters in the range of 50 to 500 molecules per cluster are to be studied p_0 must be near 2 bar.

NON-STEADY STATE NUCLEATION EFFECTS

As mentioned above most condensation experiments in Laval nozzles with throat diameters ≈ 1 cm have cooling rates in the 10^6 °C/sec range where corrections to the steady state nucleation theory are negligible.² The problem of nucleation lag time arises when the change of state of the gas becomes sufficiently fast that the cluster size distribution does not adjust quickly enough to establish a local equilibrium distribution (it being a metastable equilibrium for the supersaturated state). Therefore the steady state nucleation rate, (Eq. 2) must be modified to account for this phenomena.²⁴⁻³² Abraham³² carried out detailed numerical solutions for supersaturated water and found that the treatment by Collins²⁸ and Andres and Boudart³⁰ give the closest predictions to his computer solutions. Collins' prescription is used in this analysis. The nucleation rate therefore becomes time-dependent and, expressed in terms of the steady state rate, is

$$J_t = J_{ss} (1 - \exp(-t/\tau_n)) \quad (3)$$

where t is time and τ_n is the nucleation lag time given by the expression

$$\tau_n = (\pi r^2) \frac{(2\pi mkT)^{1/2}}{p_v} \left(\frac{\rho_c}{m}\right)^2 \frac{kT}{\sigma} \quad (4)$$

where ρ_c is the density of the condensed SF_6 . Solutions to the equations of motion including nucleation and growth, described in the section above, have been carried out using both rates, Eq. 2 and Eq. 3. Computer solutions using the steady state nucleation theory only are shown in Figs. 6-8 as dotted lines. The time-dependent nucleation rate (Fig. 6) rises more slowly than the steady state by a factor of two, peaks out slightly downstream, rises to a higher maximum value, and falls off further downstream. The increase in maximum rate for the time-dependent theory varies from 12 to 15 to 0% as p_0 varies from 7 to 3 to 1.8 bar. At $p_0 = 1.8$ bar, there is so little mass condensed ($g = 0.001$ at the nozzle exit) that the two nucleation rates coincide past the peak. The physical explanation for the qualitative differences between the two rate expressions is believed to be that as the nucleation rate is building up, the steady state rate is higher at each position and clusters grow more rapidly than if they were nucleated further downstream via the time-dependent rate. This increase in cluster growth rate depletes the vapor quicker and thus shuts off the nucleation more rapidly than in the time-dependent case. This results in a peak nucleation rate which occurs earlier in the nozzle and at lower maximum values.

This effect can also be seen when examining theoretical predictions for g as shown in Fig. 7. For the steady state nucleation case g is somewhat higher than for the time-dependent case in agreement with the relative differences cluster growth rate. The differences are largest where g changes most rapidly and this occurs at high flow densities, i.e. higher p_0 . However, for $p_0 \geq 4$ bar the theory predicts complete vapor condensation by the time

the flow reaches the nozzle exit and thus the difference between the two nucleation theories would not appear in any measurement at this point. About the largest difference at the exit for the two theories will appear for those p_0 where g_e is increasing most rapidly, i.e., in the range of 2.4 to 2.6 bar. The difference in g_e for 2.6 bar is 0.70 versus 0.675, a difference of about 3.5%. This is not considered a significant difference.

The theoretical solutions can also be used to predict mean cluster size (there is always a size distribution) and cluster concentration throughout the nozzle and in particular at the exit. Several cases are shown in Fig. 8. The droplet radius increases rapidly from 1 to 3 bar because g_e also rises rapidly in this region. Beyond that point the peak nucleation rate still increases with p_0 providing a net increase in N_e . As g_e approaches w_0 the higher cluster concentration tends to make the average cluster size smaller. However, vapor density also increases with p_0 , providing more vapor to condense on the existing clusters. For the 3% case, the two tendencies nearly cancel out, resulting in first a small decrease in size and then a net increase. In the case of the higher mole fractions N_e levels out beyond 4 bar. The slight drop and rise in mean radius is also seen for these mole fractions, however beyond 4 bar the droplet radius grows more rapidly than the 3% case due to the leveling off of N_e . Two things should be noted at this point. First, the cluster concentration for the steady state nucleation case is lower than for the time-dependent case as seen for 3%, and the mean cluster size is larger. This is completely consistent with the picture described for this phenomena ~~XX~~ when discussing Figs. 6 and 7. Secondly, N_{ge} decreases beyond 4 bar since $g_e = w_0$, even though N_e is increasing in this range. This shows that the density of the gas is increasing faster than the increase in cluster concentration. Here again N_{ge} for the steady state rate is lower than the time-dependent case above 2.2 bar; they cross over below this point.

as does N_e . The greatest difference between the two theories results in a 7% difference in \bar{r}_e and a 12% difference in N_e . The difference in light scattering cross sections $(d\sigma/d\Omega)_v$, is also 12% or less, all of which can be considered as relatively minor changes.

ONSET OF NUCLEATION

The onset of condensation using light scattering and the molecular beam measurements are presented in Fig. 9. The vapor-solid equilibrium line for SF_6 is denoted as p_∞ and provides an indication of the amount of undercooling attained. The equilibrium line for Ar has been included to indicate where it is possible to supersaturate the carrier gas in addition to the SF_6 vapor. Data from two larger nozzles, with cooling rates as shown in Fig. 5 and throat dimensions of $1.16 \times 1.10 \text{ cm}^2$ and $0.70 \times 0.40 \text{ cm}^2$, are included. In contrast, the nozzles for this work with typical throat areas of 10^{-4} cm^2 and higher cooling rates, have nucleation onsets which overlap. The undercooling, on average, increases with decreasing p_v as expected, although the scatter is larger. The detectable onset of nucleation, using light scattering, depends to some extent on the vapor pressure at onset, p_{vk} , (on vapor density, really) but translates to a condensate mass fraction of $g_k \cong 0.01\omega_o$.

Two theoretical onset curves, based on computer solutions and onset condition $g_k \cong 0.01 \omega_o$, are shown for comparison to the data. The left-most curve was calculated using the time-dependent nucleation theory, i.e. the classical theory, Eq. 2 substituted into Eq. 3. This theoretical curve moves away from the vapor-solid equilibrium line as p_v decreases in agreement with earlier results³⁵ and is due primarily to the increase in τ with T but also reflects an increase in nucleation lag as seen in Fig. 9. As p_v becomes less than 0.1 torr, the theoretical onset curves away from

the SF_6 equilibrium line more rapidly and eventually crosses the Ar vapor-solid equilibrium line. Using the correction factor $\Gamma = 10^5$ the onset curve is seen to be moved to the right closer to the equilibrium line and passing through the data at higher pressure. The data are seen to follow the theoretical curve as p_v is lowered although there are a few data points further from the theory on each side. The two lowest onsets occur in the supersaturated region for Ar and so could in principle be formed in a binary nucleation process involving both SF_6 and Ar.

The uncertainty in the points of onset derive primarily from two features, both of which are less severe as onset p_v increases. The first is an error in temperature resulting from the adiabatic assumption for the centerline flow due to wall boundary layer effects. The second is due to some additional expansion beyond the nozzle exit. The first affects both the light scattering and molecular beam measurements. The second feature affects the molecular beam measurements only since the light scattering volume is within the exit "Mach cone" at all times (1.25 mm from exit) and thus does not sense the expansion occurring beyond the end of the nozzle.²

The centerline core sampled by the molecular beam skimmer (located 3.25 mm beyond the nozzle exit) falls outside the Mach cone and thus the flow expands as the free jet, beyond the nozzle exit, adjusts to the lower ambient pressure (0.065 ± 0.010 Torr). Gasdynamic measurements in the nozzle and the free jet reveal that the centerline flow has completely expanded to the ambient pressure by the time it reaches the skimmer. Thus the expansion, for the molecular beam measurements, occurs first in the nozzle and then in the free expansion from nozzle exit to skimmer entrance. The skimmer interference with the flow is expected to be small (i.e. within the error bars of the results shown in Fig. 9) and the flow is

assumed "frozen" beyond the skimmer entrance³⁶. The nozzle exit conditions (as with the light scattering) are determined with measured properties listed in Table II. However, the onset of condensation for the molecular beam experiments occurs at the skimmer entrance. An isentrope, obtained with the specific heat ratio, γ , for the gas mixture using room temperature properties, is fitted through the exit state to determine both the conditions for onset and for crossing the vapor-solid equilibrium line. Since the pressures at exit and skimmer are known, the temperature determination requires only that the flow be adiabatic, not reversible adiabatic (i.e., isentropic). Here again the uncertainty in assuming adiabatic flow is within the error bars. Recall, however, that the molecular beam detection of onset is more sensitive than the light scattering experiments. Thus the mass fraction condensed at onset may be considerably lower than the $g_k \approx 0.01w_0$ condition for the light scattering data and the theoretical curves in Fig. 9. Therefore comparison of the molecular beam onsets to an extrapolation of the theoretical curves would not be warranted, and their location slightly "to the right" of such an extension is qualitatively expected.

CONCLUSIONS

The following are our conclusions derived from this investigation of small nozzle gasdynamics and cluster nucleation:

1. The onset of SF_6 nucleation in these small nozzles, having an order magnitude or more increase in cooling rates, is virtually the same as for the larger nozzles in the region where their onset pressures overlap.
2. As the onsets move to vapor pressures below 1 torr it is possible for the nucleation process to occur in the supersaturated region of the carrier argon gas thus introducing the possibility of binary condensation.
3. Theoretical calculations on the effect of nucleation lag times for nozzle cooling rates in the 10^7 to 10^8 °C/sec range is not an overriding feature for these flows. Estimated variation in physical properties between the time-dependent and steady state nucleation processes range from 0 to 15%.
4. Prediction of the onset of condensation with experimental measurements is satisfactory if a nucleation correction factor $\tau \sim 10^5$ is used in the computer solutions, along with previously estimated parameters to account for boundary layer effects as determined from gasdynamic measurements.¹⁷
5. The onset of condensation of SF_6 in a helium carrier gas is greatly delayed (i.e. higher p_0) over that in argon. This is caused (i.e. higher kinematic viscosity) primarily by the greater viscous dissipation/occurring in these nozzles due to wall effects. In spite of this higher entropy production, these nozzles can still produce copious amounts of large SF_6 clusters and in this sense are much more efficient than free jet molecular beam sources. The improvement in nozzle design suggested by this work, for use with helium expansions, has been

incorporated into a series of new nozzles. Investigations into noble gas clustering in helium carrier gas expansions will be reported soon.

6. These beam sources are capable of producing clusters in a size range all the way from dimers and trimers up to values in excess of 10^6 molecules per cluster, with cluster densities at the nozzle exit in a range of 1 to $4 \times 10^{11} \text{ cm}^{-3}$.
7. The experimental measurements for SF_6 onset using both molecular beam and light scattering techniques are consistent. The molecular beam measurements are more sensitive in the sense that they reveal the clustering process ~~XXXXXXXX~~ sooner than the particular arrangement for the light scattering as used here. The ionization gage measurements show the clustering emerging from unclustered beam measurements as p_0 is increased, whereas molecular light scattering is not observed above the background stray light level.

ACKNOWLEDGEMENTS

The authors would like to thank Mr. Diancheng Chi for conducting a series of gasdynamic measurements to fill in a few experimental gaps. We wish to thank the Northwestern Office of Sponsored Research for computer funds used to complete some of the theoretical analysis. We also gratefully acknowledge the Engineering Energetics Section of the National Science Foundation and the Power Branch of the Office of Naval Research for partial support of this work.

REFERENCES

1. A. Stodola, Steam and Gas Turbines, McGraw-Hill, New York, 117 (1927).
2. P. P. Wegener, Nonequilibrium Flows, P. P. Wegener, Ed. Marcel Dekker, New York, Chapter 4, 163 (1969).
3. H. L. Jaeger, E. J. Willson, P. G. Hill, and K. C. Russell, J. Chem. Phys. 51, 5380 (1969).
4. D. B. Dawson, E. J. Willson, P. G. Hill, and K. C. Russell, J. Chem. Phys. 51, 5389 (1969).
5. G. D. Stein and P. P. Wegener, J. Chem. Phys. 46, 3685 (1967).
6. B. J. C. Wu, P. P. Wegener, and G. D. Stein, J. Chem. Phys. 69, 1776 (1978).
7. B. J. C. Wu, P. P. Wegener, and G. D. Stein, J. Chem. Phys. 68, 308 (1978).
8. B. J. C. Wu and G. A. Laguna, J. Chem. Phys. 71, 2991 (1979).
9. S. S. Fisher, Phys. Fluids 22, 1261 (1979).
10. B. G. DeBoer, S. S. Kim, and G. D. Stein, Rarefied Gas Dynamics, R. Campargue, Ed. Commissariat a L'Energie Atomique, Paris, 1151 (1979).
11. A. A. Vostrikov, N. V. Gaikii, A. K. Rebrov, and B. E. Semyachkin, Sov. Tech. Phys. Lett. 4, 587 (1978).
12. E. W. Becker, H. Falter, O. F. Hagena, W. Henkes, R. Klingelhöfer, H. O. Moser, W. Obert, I. Poth, Nucl. Fusion 17, 617 (1977).
13. E. W. Becker, H. Falter, O. F. Hagena, W. Henkes, R. Klingelhöfer, H. O. Moser, W. Obert, I. Poth, 1st Symposium on the Production and Neutralization of Negative Hydrogen Ions and Beams, Brookhaven National Laboratories, Long Island, New York (1977).
14. O. F. Hagena and W. Obert, J. Chem. Phys. 50, 5 (1973).
15. O. F. Hagena, Molecular Beams and Low Density Gas Dynamics, P. P. Wegener, Ed. Marcel Dekker, New York (1974).
16. W. Obert, Rarefied Gas Dynamics, R. Campargue, Ed. Commissariat a L'Energie Atomique, Paris, 1181 (1979).
17. O. Abraham, J. H. Binn, B. G. DeBoer, and G. D. Stein, submitted to Phys. Fluids.
18. G. D. Stein, The Phys. Teacher 17, 503 (1979).
19. J. Fardeas, B. Raoult, and G. Torchet, J. Chem. Phys. 59, 3454 (1973).

20. G. D. Stein and J. A. Armstrong, J. Chem. Phys. 58, 1999 (1973).
21. E. W. Becker, K. Bier, and W. Henkes, J. Phys. 146, 333 (1956).
22. J. B. Fenn and J. Deckers, Rarefied Gas Dynamics, J. Laurmann, Ed. Academic Press, New York, p. 497 (1963).
23. J. B. Anderson, Molecular Beams and Low Density Gas Dynamics, P. P. Wegener, Ed. Marcel Dekker, New York (1974).
24. J. B. Zeldovich, Zh. Eksp. Teor. Fiz. 12, 525 (1942).
25. A. Kantrowitz, J. Chem. Phys. 19, 1097 (1951).
26. R. F. Probst, J. Chem. Phys. 19, 619 (1951).
27. H. Wakeshima, J. Chem. Phys. 22, 1614 (1954).
28. F. C. Collins, Z. Elektrochem. 59, 404 (1955).
29. W. G. Courtney, J. Chem. Phys. 36, 2009 (1962).
30. R. P. Andres and M. Boudart, J. Chem. Phys. 42, 2057 (1965).
31. J. Feder, K. C. Russell, J. Lothe, and G. M. Pound, Advan. Phys. 15, 111 (1966).
32. F. F. Abraham, J. Chem. Phys. 51, 1632 (1969).
33. J. J. Jasper, J. Phys. Chem. Ref. Data 1, 841 (1972).
34. Gmelin Handbuch der Anorganischen Chemie, Ergänzungsband 2, Schwefelhalogenide, H. Bitterer Ed. Springer Verlag, Berlin, Section 1.7.4.7, p. 141 (1978).
35. G. D. Stein and C. A. Moses, J. Coll. and Interface Sci. 39, 504 (1972).
36. J. B. Anderson, R. P. Andres and J. B. Fenn, Adv. Chem. Phys. Vol X Molecular Beams, J. Ross, Ed., Interscience Pub. (J. Wiley) New York, p. 275 (1966).

FIGURE CAPTIONS

Fig. 1 The experimental arrangement is shown in which the incoming flow contains a fixed mole fraction of SF_6 supplied from high pressure bottles. Flow enters a stagnation chamber containing nozzle N from which p_0 , T_0 and nozzle exit pressure p_e are measured. The laser beam-LB crosses the flow centerline normal to the page and light scattering is measured at right angles through a double slit, fiber optic-FO connection to a photomultiplier tube-PMT. A skimmer Sc and Collimator C sample the flow in a standard molecular beam configuration. The molecular beam-MB is collected in an ionization gage-IG. The molecular beam with clusters is crossed with a 40 KeV electron beam-EB which is collected in a Faraday cup-FC which is housed within a beam trap-BT. The total beam current is monitored with an ammeter-A and the electrons scattered at an angle θ which is adjustable is collected through a slit onto a scintillator-Si coupled to a fiber optic, photomultiplier and pulse counting electronics.

Fig. 2 The differential light scattering cross section per unit volume at the laser location $(\frac{d\sigma}{d\Omega})_v$ for 90 degree scattering is shown as a function of stagnation pressure p_0 for a variety of SF_6 mixtures. Pure argon expansion is included here as a lower limit (0 SF_6 mole fraction). Figure A is for Nozzle 6 and B for Nozzle 7. Note the scale change in the ordinate.

Fig. 3 The nucleation experiments using the molecular beam ionization gage detector are plotted as a function of p_0 and converted to an SF_6 molecular flux at the electron beam intersection.

- Fig. 4 Typical flow properties at the exit of Nozzle 7 are shown plotted as a function of p_o . They include the static pressure p_e , temperature T_e and Mach number M_R . They cover the span in mole fractions from 0% to 12.5%. Note that the exit pressures are in the 1-2 torr range while temperature approaches 30 K.
- Fig. 5 Characteristic cooling rates are shown for Laval nozzles with throat diameter equal to 1 and .0125 cm and for a free jet of the same diameter as the small Laval nozzle. The cooling rate at the throat is denoted with * and typical onset cooling rates indicated by an arrow. The steady state nucleation theory is satisfactory for the lower cooling rate but must be modified for the upper two.
- Fig. 6 The nucleation rate J has been calculated for 3% SF_6 in Ar for Nozzle 7 using appropriate boundary layer parameters as determined from gasdynamic measurements. The steady state J_{ss} is compared to the time-dependent rate J_t . Due to the nucleation lag time the time-dependent rate builds up more slowly than the steady state, rises to a higher peak value and decreases downstream of the steady state. Also as p_o is decreased J begins further down the nozzle and is spread out over a longer flow length.
- Fig. 7 The mass fraction condensed g (grams condensed per gram of mixture) is plotted as a function of position in the nozzle for the same flow conditions as Fig. 6. For $p_o > 3$ bar virtually all the vapor is predicted to be condensed out.
- Fig. 8 The mean particle radius at the exit - \bar{r}_e plus cluster concentration both per unit volume - N_e and per unit gram of mixture - N_{pe} are plotted for several SF_6 mole fractions as a function of p_o . For higher mole fractions the onset of nucleation occurs at lower p_o .

and the clusters grow to larger mean sizes while the number density per unit volume is inversely proportional to mole fraction. The steady state nucleation theory predicts a slightly larger size and smaller concentration for the 3% mixtures. Note that cluster concentration per gram of mixture goes through a maximum at $p_0 = 4$ bar.

Fig. 9 The onset of SF_6 nucleation has been plotted in a phase diagram where p_v is the partial pressure of the SF_6 . The equilibrium lines for both SF_6 and Ar are shown. Previous data from "large" nozzles⁷ are compared with these results and the theoretical predictions are shown as the two solid lines $\tau = 1$ and 10^5 . The symbols with circles around them denote the molecular beam data. Note that three of the lower onset points cross the Ar equilibrium line.

TABLE I
Nozzle Geometry a)

Nozzle Number	D_o cm	D_c cm	L cm	θ_T Deg	θ_N Deg	a_o	a_1	a_2	a_3	a_4	a_5	a_6	a_7
1	0.0137	0.256	3.05	1.78	4.61	0.0137	-0.0982	0.3843	-0.4834	0.3189	-0.0984	0.0113	0
6	0.0119	0.256	2.31	7.31	6.56	0.0119	0.1038	-0.0404	0.1133	-0.065	0.0102	0	0
7	0.0127	0.218	3.0	2.95	3.83	0.01277	-0.01553	0.1555	-0.18189	0.09671	-0.0058	-0.0092	0.0018

a) Polynomial equation for nozzle contour is: $D(x) = \sum_{i=0}^7 a_i x^i$ with D and x in cm.

TABLE II
PROPERTIES FOR FLOWS WITH ONSET OF CONDENSATION
AT NOZZLE EXIT (LIGHT SCATTERING EXPERIMENTS)
OR AT SKINNER ENTRANCE (MOLECULAR BEAM EXPERIMENTS)

Nozzle	X_0 SF ₆ -mole fraction (%)	Measured Data			Derived Quantities at Nozzle Exit (a)				Derived Quantities at Skinner Entrance (b)			
		Method (d)	P_0 (bar)	P_e (corr)	P_{ve} (corr)	T_e (°K)	M_e (k)	ΔT_{ad} (°K)	P_{vs} (corr)	T (°K)	M_s (g)	ΔT_{ad} (°K)
1	0.03	L.S.	2.08	1.21	0.037	40.5	4.47	104.5				
	0.0625	L.S.	1.61	1.13	0.071	63.8	3.45	76.2				
	0.125	L.S.	1.71	1.24	0.155	71.6	3.34	78.4				
	0.125 SF ₆ -He	L.S.	3.78	2.448	0.306	41.3	4.62	128.7				
6	0.03	L.S.	2.87	0.956	0.0285	27.5	5.56	122.5				
	0.0625	L.S.	1.74	0.895	0.0559	79.5	3.01	50.5				
	0.125	L.S.	1.78	0.90	0.1125	67.8	3.45	82.2				
	0.125 SF ₆ -He	L.S.	3.38	2.216	0.276	74.5	3.26	80.5				
7	0.03	L.S.	2.06	1.42	0.0426	55.4	3.56	84.6				
	0.0625	L.S.	1.57	1.02	0.06375	91.0	2.83	56.0				
	0.125	L.S.	1.71	1.13	0.14125	79.7	3.27	64.3				
	0.125 SF ₆ -He	L.S.	3.95	2.76	0.345	93.5	2.95	56.5				
	0.03	M.B.	1.58	1.04	0.0312	95.5 (1)	2.77		0.0020	35.1	5.14	79.0
	0.0625	M.B.	1.28	0.99	0.06187	94.0 (1)	2.32		0.0041	53.0	4.36	79.0
	0.125	M.B.	1.33	1.00	0.125	98.0 (1)	2.42		0.0081	65.8	4.28	79.0

a) onset is at the nozzle exit for the light scattering experiments, i.e. $P_{ve} = P_{vk}$, $T_e = T_k$ and $M_e = M_k$.

b) onset is at the skimmer entrance for the molecular beam experiments, i.e. $P_{vs} = P_{vk}$, $T = T_k$ and $M_s = M_k$.

c) In Ar unless denoted with He.

d) L.S. - light scattering, M.B. - Molecular Beam.

e) $P_{ve} = P_{v0}$, where X_0 is initial SF₆ mole fraction.

f) Derived from energy conservation assuming adiabatic flow.

g) calculated from P_e and P_{in} pressure measurements.

h) $P_{vs} = P_{0.065}(\text{corr})/X_0$

i) average from two experiments.

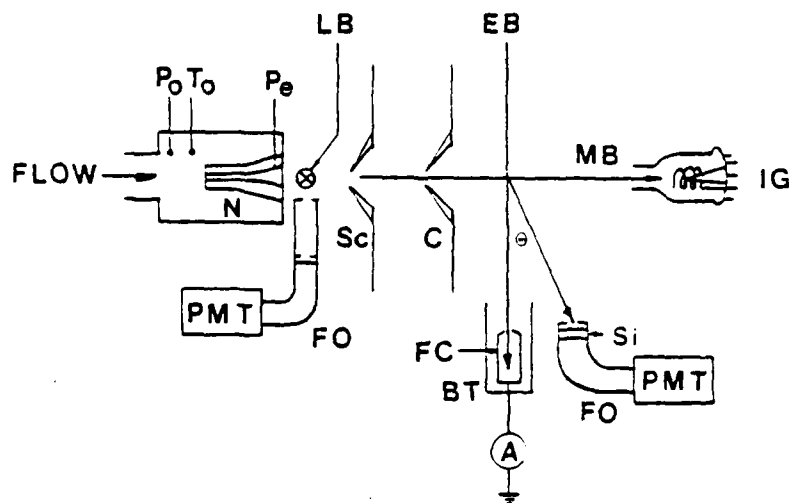


Fig. 1 The experimental arrangement is shown in which the incoming flow contains a fixed mole fraction of SF_6 supplied from high pressure bottles. Flow enters a stagnation chamber containing nozzle N from which p_0 , T_0 and nozzle exit pressure p_e are measured. The laser beam-LB crosses the flow centerline normal to the page and light scattering is measured at right angles through a double slit, fiber optic-FO connection to a photomultiplier tube-PMT. A skimmer Sc and Collimator C sample the flow in a standard molecular beam configuration. The molecular beam-MB is collected in an ionization gage-IG. The molecular beam with clusters is crossed with a 40 KeV electron beam-EB which is collected in a Faraday cup-FC which is housed within a beam trap-BT. The total beam current is monitored with an ammeter-A and the electrons scattered at an angle θ which is adjustable is collected through a slit onto a scintillator-Si coupled to a fiber optic, photomultiplier and pulse counting electronics.

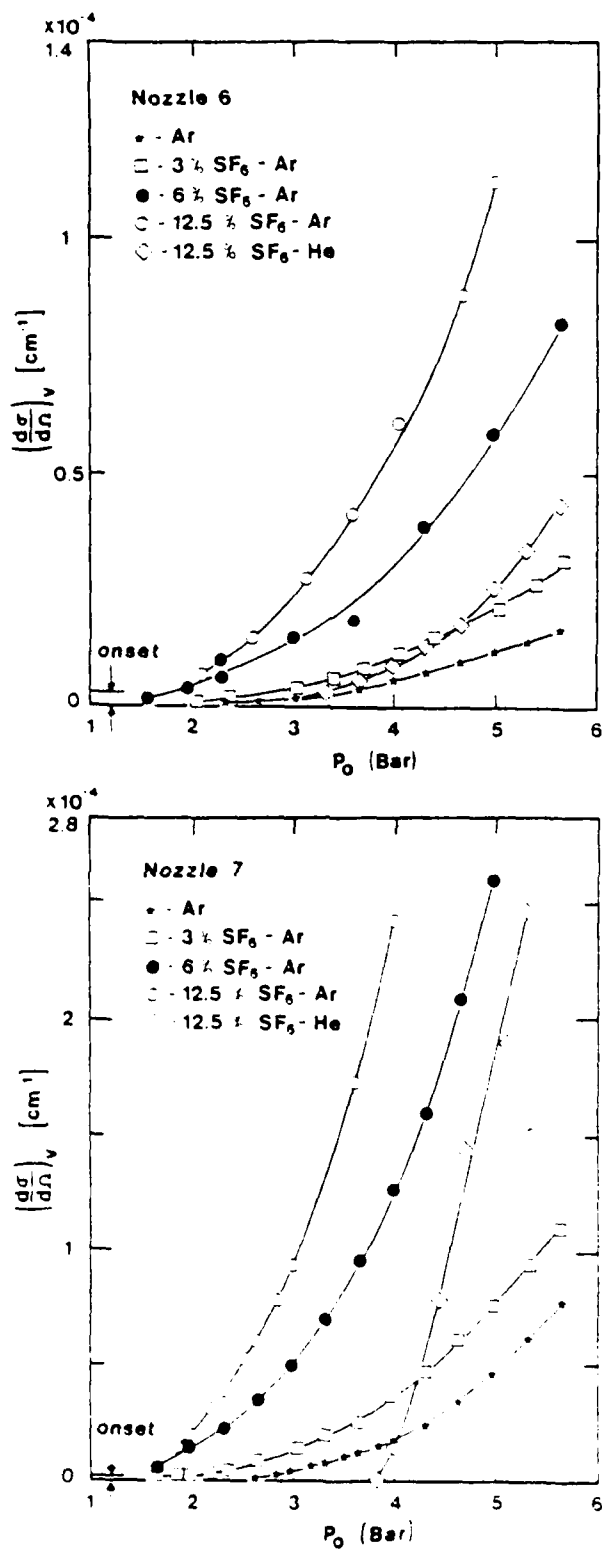


Fig. 2 The differential light scattering cross section per unit volume at the laser location- $(\frac{d\sigma}{d\Omega})_v$ for 90 degree scattering is shown as a function of stagnation pressure P_0 for a variety of SF_6 mixtures. Pure argon expansion is included here as a lower limit (0 SF_6 mole fraction). Figure A is for Nozzle 6 and B for Nozzle 7. Note the scale change in the ordinate.

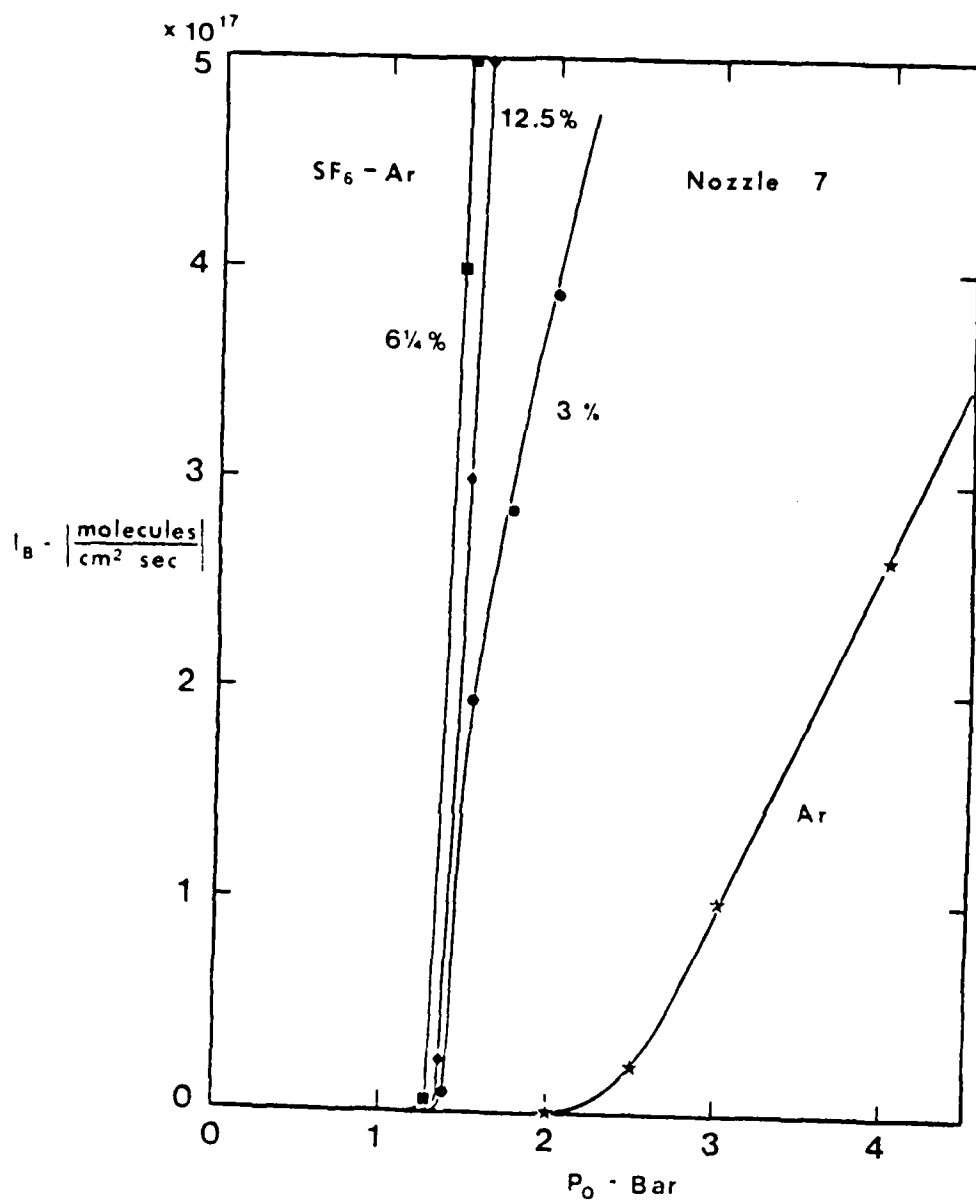


Fig. 3 The nucleation experiments using the molecular beam ionization gage detector are plotted as a function of p_0 and converted to an SF₆ molecular flux at the electron beam intersection.

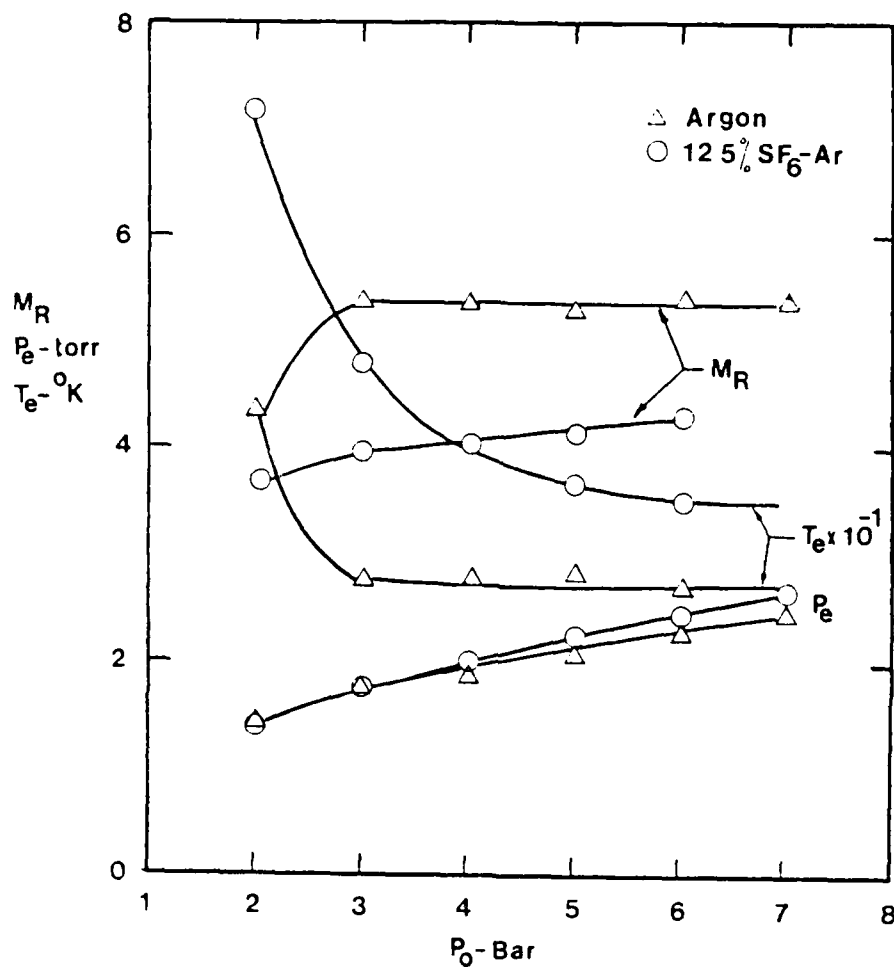


Fig. 4 Typical flow properties at the exit of Nozzle 7 are shown plotted as a function of p_0 . They include the static pressure p_e , temperature T_e and Mach number M_R . They cover the span in mole fractions from 0% to 12.5%. Note that the exit pressures are in the 1-2 torr range while temperature approaches 30 K.

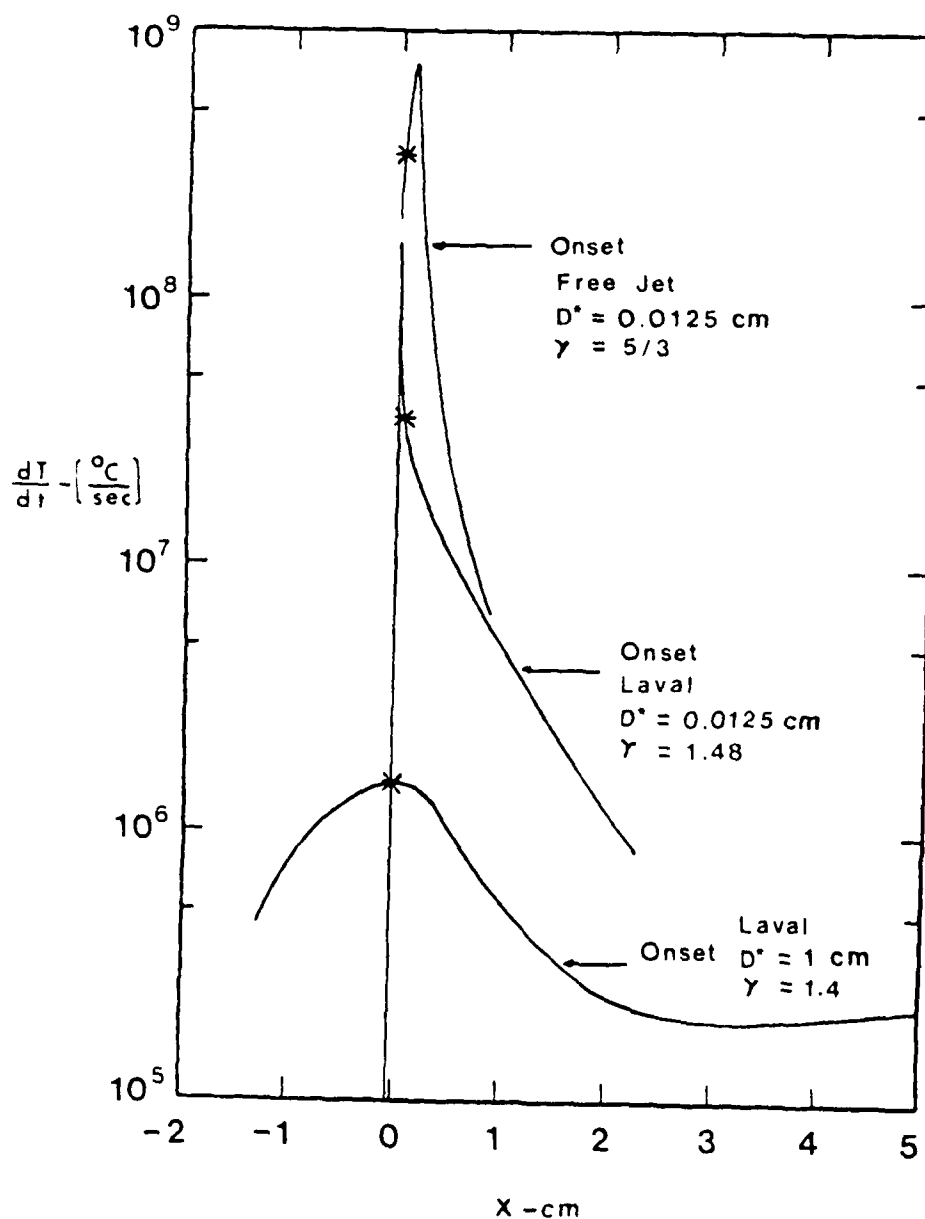


Fig. 5 Characteristic cooling rates are shown for Laval nozzles with throat diameter equal to 1 and .0125 cm and for a free jet of the same diameter as the small Laval nozzle. The cooling rate at the throat is denoted with * and typical onset cooling rates indicated by an arrow. The steady state nucleation theory is satisfactory for the lower cooling rate but must be modified for the upper two.

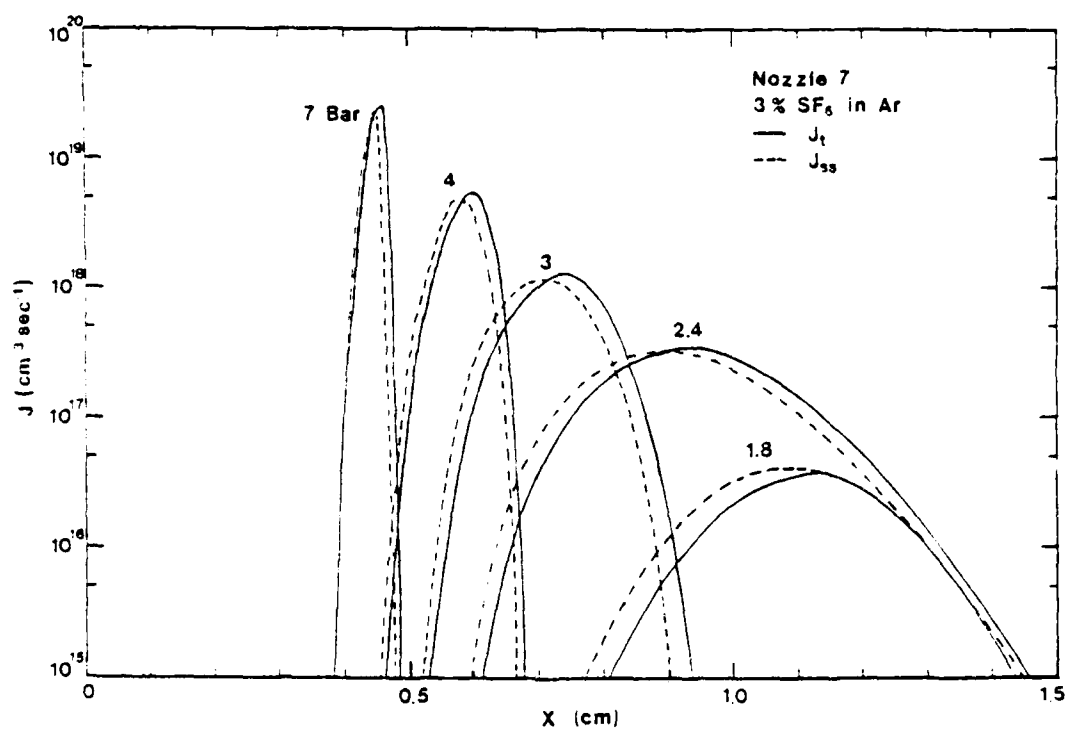


Fig. 6 The nucleation rate J has been calculated for 3% SF₆ in Ar for Nozzle 7 using appropriate boundary layer parameters as determined from gasdynamic measurements. The steady state J_{ss} is compared to the time-dependent rate J_t . Due to the nucleation lag time the time-dependent rate builds up more slowly than the steady state, rises to a higher peak value and decreases downstream of the steady state. Also, as p_0 is decreased from 7 Bar, J begins further down the nozzle and is spread out over a longer flow length.

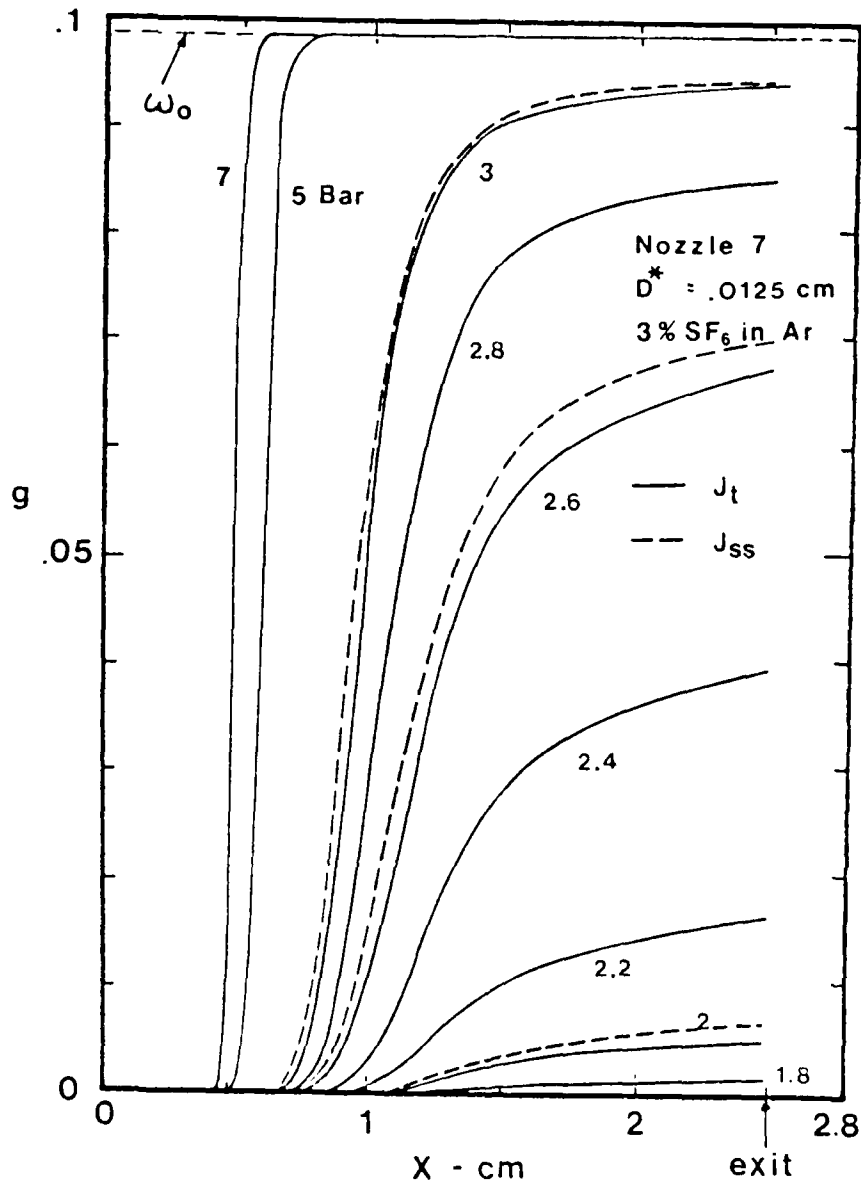


Fig. 7 The mass fraction condensed g (grams condensed per gram of mixture) is plotted as a function of position in the nozzle for the same flow conditions as Fig. 6. For $p_0 > 3$ bar virtually all the vapor is predicted to be condensed out.

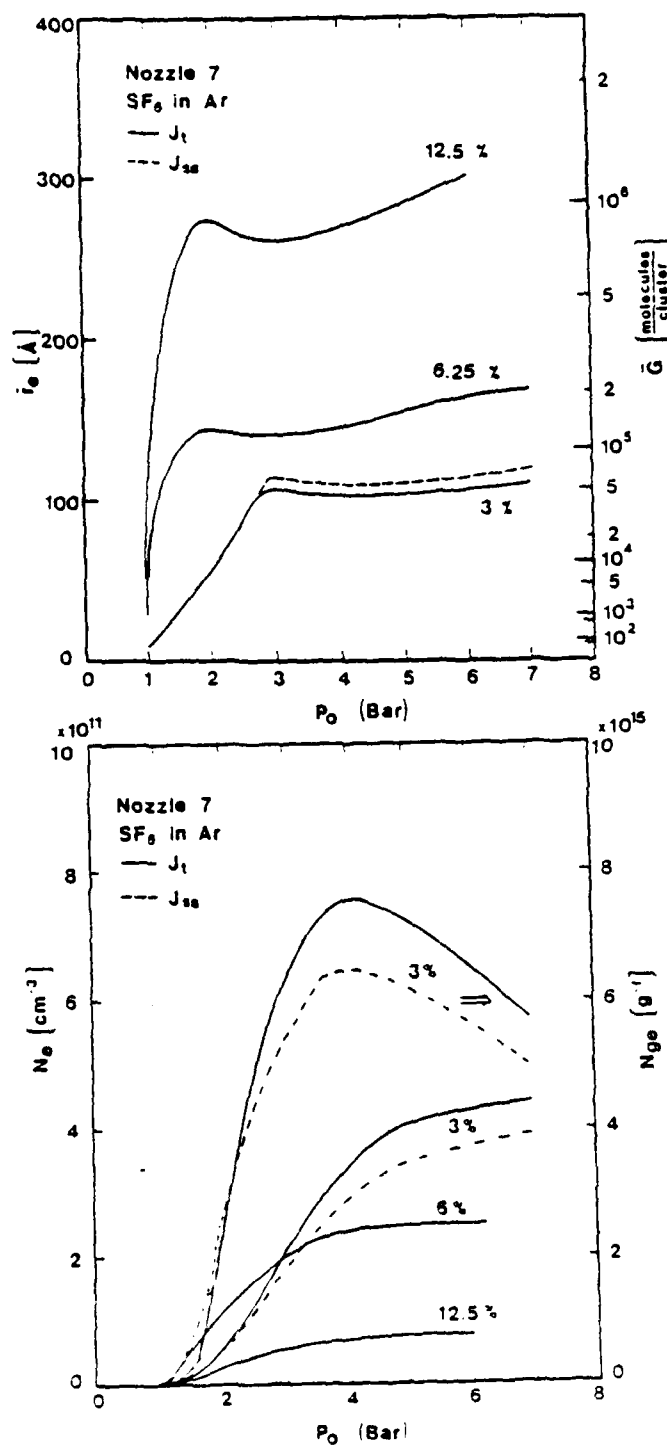


Fig. 8 The mean particle radius at the exit - \bar{r}_p plus cluster concentration both per unit volume - N_p and per unit gram of mixture - N_{gp} are plotted for several SF₆ mole fractions as a function of p_0 . For higher mole fractions the onset of nucleation occurs at lower p_0 and the clusters grow to larger mean sizes while the number density per unit volume is inversely proportional to mole fraction. The steady state nucleation theory predicts a slightly larger size and smaller concentration for the 3% mixtures. Note that cluster concentration per gram of mixture goes through a maximum at $p_0 = 4$ bar.

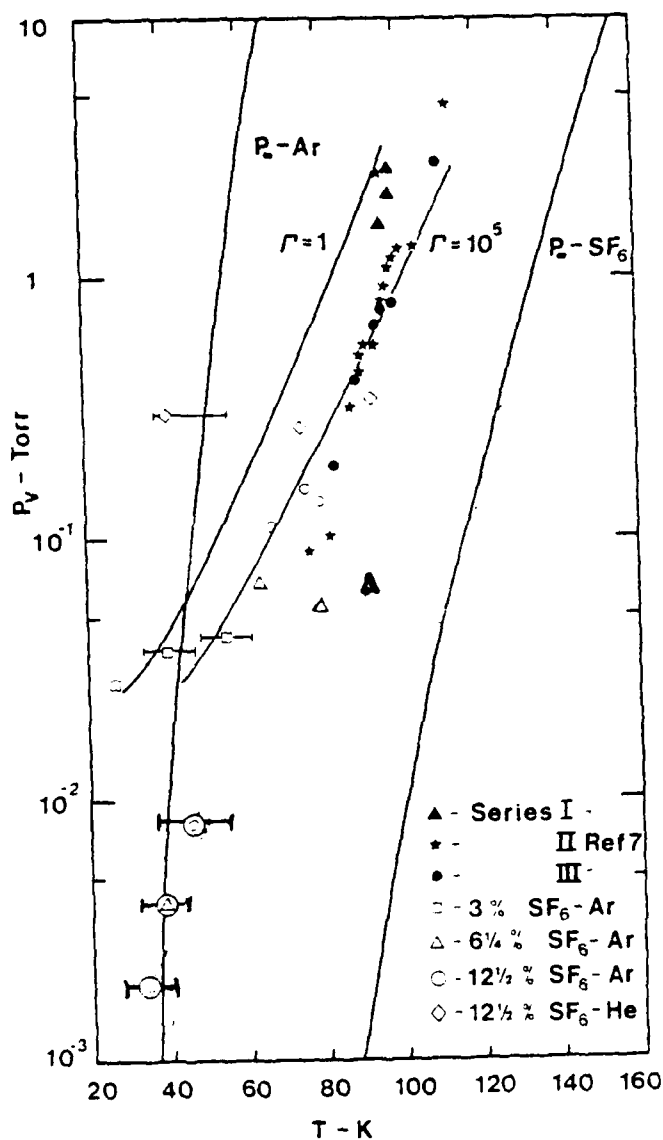


Fig. 9 The onset of SF_6 nucleation has been plotted in a phase diagram where p_v is the partial pressure of the SF_6 . The equilibrium lines for both SF_6 and Ar are shown. Previous data from "large" nozzles⁷ are compared with these results and the theoretical predictions are shown as the two solid lines $r = 1$ and 10^5 . The symbols with circles around them denote the molecular beam data. Note that three of the lower onset points cross the Ar equilibrium line.

GASDYNAMICS OF VERY SMALL LAVAL NOZZLES

O. Abraham, J. A. Binn, B. G. DeBoer and G. D. Stein

submitted to Physics of Fluids

GASDYNAMICS OF VERY SMALL LAVAL NOZZLES

by

Oommen Abraham, Jack H. Binn,^{a)} Barry G. DeBoer,^{b)} and Gilbert D. Stein
Northwestern University
Gasdynamics Laboratory
Evanston, Illinois 60201
February 11, 1980
(Revised August 20, 1980)

ABSTRACT

An investigation of diverging supersonic nozzles with throat diameters in the range of 0.025 to 0.25 mm has been carried out using gasdynamic measurements for a variety of gases and mixtures with sulfur hexafluoride. Due to the small nozzle size, boundary layers, although thin, may constitute a major fraction of the flow or, indeed at low pressures, may be fully developed. Nevertheless these nozzles have been shown to be very efficient for production of clusters condensed from the expanding gas. They produce orders of magnitude increases in molecular beam intensities, relative to the conventional, "isentropic" free jet sources. The effects of gas properties and nozzle design on performance have been analyzed and compared to theoretical solutions to the governing equations of motion including condensation due to cluster nucleation and growth.

PACS Numbers

- 1.) 47.55.Ea
- 2.) 47.55.kf
- 3.) 82.60.Nh
- 4.) 36.90.+f

^{a)} Present address: Midwestco Corp., Chicago, Illinois 60606
^{b)} Present address: GTE Sylvania Laboratory, Salem, Massachusetts 01970

INTRODUCTION

The study of small Laval nozzles has been undertaken in our laboratory as part of a research investigation into the properties of microscopic atomic or molecular particles. These nozzles constitute the source or first stage of a molecular beam apparatus which will provide a continuous stream of clusters in a high vacuum environment. It is well known that when a gas supersaturates in an adiabatic expansion the amount of undercooling that occurs before the onset of condensation depends on the cooling rate in the expansion. The slower the expansion, the smaller the amount of undercooling for cases where the expansion is continuum or collision dominated. For supersonic expansions the cooling rate scales with the throat dimension. Thus larger nozzles will form droplets earlier in the expansion (i.e. at lower supersaturations and higher temperatures) than for small nozzles. Free jet or uncontrolled expansions into a high vacuum environment represent the most rapid, in fact the upper limit, cooling rate attainable in an adiabatic gas expansion. Thus it is expected that a free jet expansion will produce far less condensate than a controlled Laval nozzle expansion of the same size. This is in fact the case as has been demonstrated previously.¹⁻⁵

The use of small nozzles has become attractive for a number of important technological applications. One method of uranium isotope separation involves the adiabatic cooling of UF_6 to as cold a temperature as possible for use of tunable spectroscopic selection of isotopes.^{6,7} Therefore small nozzles are potentially useful in that they delay nucleation due to their rapid cooling rates and yet maintain relatively high cluster densities compared /with the uncontrolled free jet expansions. Another application which is being implemented in Germany involves a small Laval nozzle expansion to produce clusters of hydrogen to be used for fusion machine fueling and heating.^{8,9} A prototype of this scheme is currently under

evaluation. A third use for these small nozzles in conjunction with a high vacuum, molecular beam type of configuration, would be to form small metal or semiconductor clusters for production of thin film devices.¹⁰ The prospect of producing thin films with unusual or more uniform properties is the goal here. Finally, there are a number of applications for small nozzles in basic research. Primarily they can be used as an efficient source of small clusters in order to study the physical properties of the clusters themselves or to use them in the study of atoms or molecules adsorbed onto them.

It is perhaps ironic that the development of molecular beam sources has gone through a couple of full circles. The initial sources in the 1930's were orifice or free jet expansions^{11,12} but at such low pressures that they were effusive in nature. Then in 1951 it was suggested that the source pressure be increased and that the orifice be replaced with a hypersonic nozzle to make use of the so-called Mach focusing in order to increase beam intensity. Due to some problems with regard to viscous effects and flow blockage, in the particular configuration considered, this technique was dropped in favor of high pressure free jet expansions which eliminated the viscous effects but retained the advantages of Mach focusing. This method has been used up to the present time as a beam source for a great variety of basic and applied research.¹³⁻¹⁵ Recently with the advent of greatly increased interest in the study of small aggregates in the gas phase, the Laval nozzle has reemerged as an important device. The design, however, is substantially different from that originally proposed.

As an example, consider the enormous increase in cluster beam intensity from a Laval nozzle as compared ^{with} a free jet source (with the same throat diameter). The relative beam intensity of a pure argon cluster beam is shown in Fig. 1. By the time the source pressure is raised to $p_0 = 3$ bar ($1 \text{ bar} = 10^5 \text{ Pa} \equiv \text{Newton/m}^2 = 0.99 \text{ atmosphere} \equiv 760 \text{ torr}$) the beam intensity is off scale for the ionization gage detector used in this experiment. On the other hand, even at $p_0 = 11$ bar the free jet beam intensity is so low that it was not usable for our electron beam diffraction experiments. Thus it becomes obvious, both from theoretical consideration as well as experimental evidence, that the controlled expansion of a small Laval nozzle is far superior to that of the free jet with respect to making cluster beams.

That this great enhancement in beam intensity exists has been demonstrated in several laboratories.¹⁻⁴ However, in order to understand the dynamics of the expansion in some detail, to be able to predict when condensation will begin for a given gas or gas mixture, and to determine how to design nozzles for future applications, a series of gasdynamic studies has been undertaken. For example, it is known that solid boundaries will grow boundary layers which for normal flow situations would be thin at these pressures. However even thin boundary layers (of the order of 0.1 mm) can constitute a significant fraction of the nozzle radius or even the entire radius (i.e., fully developed flow). Nevertheless, even though there are viscous effects in small nozzles, there are conditions in which the clustering is still far superior to the "inviscid" free jet expansions. How important and under what flow conditions are viscous effects important or dominant in the small nozzle expansions? Is there an isentropic core in these expansions and if so under what circumstances? Is it possible to design nozzles which use helium as a coolant or carrier gas when the viscous effects in helium flows are much greater than for heavier species, that is, species with much greater collision cross sections? Is it possible to optimize the design parameters such as throat size, divergence angle, nozzle length and contour to produce clusters of given concentrations and/or size? Since pumping capacity in high vacuum systems is always a problem, how small a nozzle can one use and still get sufficient beam densities?

EXPERIMENTAL CONFIGURATION

The apparatus built to test nozzles is shown in Fig. 2. It is connected to the laboratory foreline manifold which is pumped by two mechanical pumps in series with a large enough capacity so that the pressure downstream of the nozzle exit, p_A , is in the range of 0.01-0.1 torr. The nozzles are axisymmetric and made from glass capillary tubing with entrance diameters $D_0 = 0.025-0.3$ mm with exit diameters $D_e = 3-4$ mm. Several different nozzle extensions are used to test the effect of nozzle length on performance. A static pressure tap is installed in these extensions in order to avoid drilling holes in the glass. The static pressure at the nozzle exit, p_1 , is measured using a 10 torr capacitance manometer.

Stagnation chamber pressure p_0 and temperature T_0 are also measured. Gas is supplied from bottles either as pure vapor or as mixtures of known mole fraction. Downstream of the nozzle exit a Pitot tube is mounted on a pressure transducer and manipulated with x-y-z motion capability. Thus the total pressure, p_{02} , can be measured as a function of position either along the flow direction or normal to it. T_0 is always near room temperature and p_0 is varied from 1 to 11 bar. Since it is known from the molecular beam experiments that condensation will occur in these nozzles as p_0 is increased, an argon ion laser and associated optics are included in order to detect the onset of nucleation just beyond the exit of the nozzle.

Results from four nozzles will be discussed in this paper and their contours are shown in Fig. 3. The diameter has been expanded by a factor of 8 to highlight the differences. Nozzle 7 looks like a cut-off version of nozzle number 4 with respect to the downstream contour but has a larger throat diameter. Nozzle 1 has the lowest divergence angle near the throat, θ_T , and Nozzle 6 the greatest. Nozzle 1 opens up more rapidly than the others toward the exit. Nozzle 7 has the smallest exit diameter, 2 mm, and Nozzle 6 is the shortest. In order to get an idea of the actual contour Nozzle 7 is also plotted on a 1:1 scale showing that the expansion is indeed very gentle. Two angles are used to characterize each nozzle defined as follows:

$$\theta_T \equiv \tan^{-1} \left(\frac{dD}{dx} \right)_{x=0} \quad (1)$$

$$\theta_N \equiv \tan^{-1} \left(\frac{D_e - D_0}{L} \right), \quad (2)$$

where L is nozzle length.

Note that none of these nozzles has a converging section. This is done mainly to eliminate boundary layer growth through the minimum section (throat) of the nozzle. Also, since they have relatively high exit Mach numbers, conditions at the entrance up to Mach 1 will not significantly influence conditions at the exit. Three different exit configurations are shown in Fig. 3. They have the effect of reducing nozzle length going from A to C, with the additional length being 5 mm, 0.5 mm, and 0. The geometrical contours of the nozzles are measured using precision drill rod, as plus gages. These data are used in a computer program to provide a best fit using a seventh-order polynomial

$$D(x) = \sum_{i=0}^7 a_i x^i, \quad (3)$$

where the coefficient a_i and other pertinent dimensions for the nozzles are given in Table I.

MEASUREMENTS AND GASDYNAMIC INTERPRETATIONS

The basic experimental procedure is as follows:

- (1) Install a particular nozzle and nozzle exit extension.
- (2) Choose a particular gas mixture to be used for a complete set of measurements.
- (3) Run at constant pressure, measure p_o , T_o , p_1 , p_{02} on centerline.
- (4) Record Pitot pressure traces as a function of x , y , or z .
- (5) Take intermittent measurements of light scattering at nozzle exit.
- (6) Change p_o and repeat 3-5 above.
- (7) Change gas or gas mixture and repeat 2-6.
- (8) Change nozzle and/or nozzle exit extension and repeat 2-7.

It would, of course, be desirable to have measurements along the complete nozzle contour, but this would have entailed an enormous design and instrumentation program. Also since the primary interest is in the flow out of the nozzle exit, it is the properties at this point which are of greatest concern. The data are summarized in Table II.

The first level of analysis makes use of the above listed measurements in conjunction with straightforward one-dimensional gasdynamic analysis. The single most important parameter for characterizing flow conditions is the Mach number at the nozzle exit. The Mach number is calculated in three ways. If one assumes that there is an isentropic core then p_1 and p_o will yield a Mach number via the well known relation

$$\frac{p_1}{p_o} = \left(1 + \frac{\gamma-1}{2} M_s^2 \right)^{-\frac{\gamma}{\gamma-1}}, \quad (4)$$

where γ is the ratio of specific heats and M_s is the Mach number at the exit using static pressure measurement. The second method of calculating an exit Mach number is to use the Pitot pressure measurement. Here the flow must also be assumed to be isentropic (on the centerline) so that the total pressure ahead of the Pitot probe is the same as p_o . With this assumption the Mach number can be obtained with the supersonic Pitot equation:

$$\frac{p_o}{p_{02}} = \left(\frac{2\gamma M_p^2 - \gamma + 1}{\gamma + 1} \right)^{\frac{1}{\gamma-1}} \left(\frac{2 + (\gamma-1)M_p^2}{(\gamma+1)M_p^2} \right)^{\frac{\gamma}{\gamma-1}} \quad (5)$$

The third method for calculating exit Mach number is to make use of the so called Pitot-Rayleigh equation. This requires only local measurements, that is, the static pressure at the exit p_1 and the centerline Pitot pressure p_{02} at the same location in the nozzle as the static pressure tap. This method does not rely on any previous history of the centerline flow, that is, it does not have to be isentropic. Since the nozzle angular gradients are very small, treating the flow as one dimensional is a good assumption and thus p_1 is also the centerline static pressure. The Pitot-Rayleigh Mach number M_R is obtained using:

$$\frac{p_1}{p_{02}} = \left(\frac{2\gamma M_R^2 - \gamma + 1}{\gamma + 1} \right)^{\frac{1}{\gamma-1}} \left(\frac{2}{(\gamma+1)M_R^2} \right)^{\frac{1}{\gamma-1}} \quad (6)$$

The exit Mach number calculated in the three ways described here are shown plotted in Fig. 4 for Nozzle 7 as a function of p_o for argon expansions. Results for the long nozzle extension A ^{arg} shown as the dotted curves and the short nozzle extension B as solid lines. First of all, note that both M_s and M_p are greater than the Pitot-Rayleigh Mach number M_R . This is a reflection of the fact that the centerline or core flow is not isentropic. When comparing the results of the long and short nozzle extensions we see that the static Mach numbers agree but the Pitot and the Pitot-Rayleigh do not. If it is assumed that the additional nozzle length results in increased viscous dissipation, then the larger values for M_p and the smaller values of M_R are qualitatively consistent. It is interesting that the static Mach number M_s is the same in both cases. In Fig. 4 (b) we see the results using the same nozzle for sulphur hexafluoride, SF_6 . Here the Mach numbers computed in all three ways are in fairly close agreement. This can be interpreted to mean that there is relatively little viscous dissipation on the centerline or core flow, i.e., that the core flow is isentropic.

It is also noteworthy to point out that all of the Mach number curves are nearly flat beyond $p_o = 2$ bar. This is normally interpreted to mean that the boundary layers in the nozzle are not changing with increasing pressure and thus that there is indeed an isentropic core with size not

varying appreciably with pressure. However, since the three Mach numbers do not agree, except in the case of SF_6 , there must have been some entropy production between the stagnation chamber and the nozzle exit. Beyond $p_0 = 3$ bar there is some entropy increase in the flow due to latent heat release due to condensation, except in the case of pure SF_6 and He. The discrepancy between the Mach number based on geometric area ratio, M_G and the other Mach numbers is due, of course, to the boundary layer.

In order to obtain a more complete picture of the nozzle flow, Pitot traverses perpendicular and parallel to the flow direction are taken. Pitot traverses across the flow just beyond the nozzle exit (i.e. along the y directions with the $z = 0$, see Fig. 3) are shown in Fig. 5 for two of the nozzles fitted with the long nozzle extension A. The Pitot tube has an OD of 0.5 mm and an ID of 0.25 mm and is set 0.76 mm from the nozzle exit. Figure 5A shows the results for both helium and argon expanded through Nozzle 6. The first thing to be noticed is that wherever there are flat sections of the profile, they constitute relatively small fractions of the exit diameter. For the argon the first evidence for a flat part of the Pitot (and therefore the velocity) profile appears at $p_0 = 2.5$ bar. The helium on the other hand must be expanded from a stagnation pressure of nearly 8 bar before a level part of the Pitot trace is seen. The level section is interpreted as a flat velocity profile, i.e. a region outside the boundary layer. It is also seen that the flat velocity profile disappears for the argon at higher pressures. This is believed due to the massive condensation occurring at these pressures and the possibility that the droplets are large enough to traverse the stand-off shock wave and enter the probe before complete evaporation.

The Pitot traverse measurements at the exit for Nozzle 4 are shown in Fig. 5B. The most important difference between Nozzle 4 and the others is that its throat diameter is smaller by a factor of 2 or more. Thus viscous effects can reach the centerline from the wall more readily. Here it is seen that even starting pressures as high as 10 bar produce no flat profile. Also notice that the magnitude of the Pitot pressure is around 5 torr as compared ^{with} 120 torr in Nozzle 6, an enormous difference. Even the argon must be expanded up to nearly 8 bar before a flat velocity profile is obtained. Recall that the downstream ambient pressure, p_a in Fig. 2, is in the range of 0.1-0.01 torr and so there is an additional expansion beyond the nozzle exit. Also, as the free jet continues downstream of the nozzle exit, there will be a mixing zone with the ambient gas.

Pitot traces along the nozzle centerline show a variation in pressure with x at the lower pressures for argon and at all pressures for helium. In Fig. 6 Pitot profiles are shown at several x locations from the

exit of the nozzle downstream. The flow is argon through Nozzle 1, exit configuration B (i.e., Nozzle 1-B) with the exit defined as 0.5 mm beyond the end of the glass nozzle (see Fig. 3). Many of the Pitot profiles with this configuration show pressure bumps or "horns" on either side of the centerline. This type of feature has been observed in supersonic boundary layer flow as the Pitot probe approaches the solid boundary.¹⁶ Under these circumstances the shock wave standing off the Pitot probe can interact with the boundary layer causing separation upstream of the probe thus changing the flow field seen by the Pitot tube. This explanation is consistent with all of the Pitot traverses that we have made in the course of these studies. The horns have been seen only when the probe is within the nozzle or in the neighborhood of the exit, i.e., close to solid boundaries. It also disappears in nozzle flows where $p_0 \leq 3$ bar. As the probe moves out of the nozzle the horns get smaller and then disappear by the time the probe is 1.5 mm downstream (i.e., $x/D_e = 0.6$). Notice also that the centerline Pitot pressure is dropping as the probe is moved further downstream.

The symmetry of the horns is related to the direction the probe is moving, that is, away from or toward the solid boundary. When the probe direction is reversed the asymmetry of the Pitot profile is reversed. The Pitot profiles are not taken as continuous traverses across the flow, but as discrete points waiting a sufficient time at each point to insure that no time lag appears in the measurements.

An extensive set of Pitot profiles has been taken for a great variety of flows in several of the nozzles. An example is provided in Fig. 7 for Ar and Ar-SF₆ mixtures in Nozzle 7-B. The Pitot probe is located 0.5 mm into the nozzle, at the plane between the glass nozzle and the exit extension. (See Fig. 2 or 3). The effect of the SF₆ on the boundary layer growth can be seen. At $p_0 = 3$ bar the flat portion of the profile is quite small in the Ar flow and gets larger as the percentage of SF₆ is increased. Thus the SF₆ reduces the boundary layer thickness. (Although the flows presented here were all steady, under some circumstances, especially with high SF₆ mole fractions, the flow became unsteady when probed by the Pitot tube.) As expected, the increase in the size of the core flow with starting pressures is evidenced in all three sets of data.

Because the Pitot probes must be smaller than the characteristic flow diameter and since the density in the flow near the exit is falling rapidly

there is some concern as to whether there might be significant corrections to the one-dimensional Pitot probe theory assumed for Eqns. (5) and (6).

It is known that due to viscous effects Pitot tube measurements in the flow field will be different than that of the true total pressure if the Reynolds number of the probe Re_p is less than 100^{17} (based on probe diameter and properties just ahead of the probe but behind the detached shockwave). In the range $100 > Re_p > 10$ the measured value falls to about 85% of the theoretical value and then rises above the theory for $Re_p < 10$. In order to test this effect it

is necessary to probe a flow of known properties. The obvious choice for this investigation is the use of free jet orifices. The theory for free jet expansions has been verified many times and with a variety of different types of measurement.¹⁸ Pitot data have been taken with two different orifices by different investigators more than a year apart. They are converted to Mach number using Eqn. (5) and compared in Fig. 8 to the theoretical Mach number given by Ashkenas and Sherman:¹⁹

$$M = A \left(\frac{x-x_o}{D} \right)^{\gamma-1} - \frac{1}{2} \frac{(\gamma+1)}{(\gamma-1)} \left[A \left(\frac{x-x_o}{D} \right)^{\gamma-1} \right] \quad (7)$$

where A and x_o/D are constants dependent on γ with the following values: for $\gamma = 5/3$, $A = 3.26$, $x_o/D = 0.075$; for $\gamma = 1.4$, $A = 3.65$, $x_o/D = 0.40$. The earlier data are from an orifice with throat size was 0.155 mm for argon, helium and nitrogen while the later data are for argon only using an orifice of 0.65 mm diameter. The error bars on the earlier data are due to an uncertainty in the probe location with regard to the exit of the orifice. It is seen, however, that the data fit the theory quite well, but are slightly lower than the theory except for the helium data without error bars (i.e., large orifice experiments.) This small deviation may be due to condensation effects. All data presented in Fig. 8 are for high enough starting pressures p_o so that $Re_p > 100$, i.e. no pressure corrections are required. At lower p_o the deviation between measurements and theory can be reconciled with the Pitot correction.¹⁷ Thus the Pitot-Rayleigh Eqn. (6) can be used with confidence if $Re_p > 100$ and all of the results presented in this paper meet this criterion.

The exit Mach number has been determined for numerous gases and nozzles. The two most important factors affecting the value of the Mach number are dynamic viscosity μ and specific heat ratio γ . Increasing μ and decreasing γ will lower the Mach number. Also as p_o is increased, latent heat due to condensation will decrease the Mach number slightly. The results for Nozzle 1 are presented in Fig. 9A and show a Mach number plateau with increasing pressure for Ar, Ar-SF₆ mixtures, and SF₆. At the higher pressures the Mach number for Ar, 3 and 5% SF₆-Ar mixtures all occur at a value of about 1.5. Thus in this range the counteracting effects of decreasing γ and decreasing viscosity with increasing SF₆ mole fraction, plus the effect of heat addition just cancel out. The pure SF₆ would be expected to be

AD-A093 950

NORTHWESTERN UNIV EVANSTON IL DEPT OF MECHANICAL AND--ETC F/G 7/4
INVESTIGATION OF METAL AND METAL OXIDE CLUSTERS SMALL ENOUGH TO--ETC(U)
NOV 80 G D STEIN
TR-17

N00014-76-C-0378

NL

UNCLASSIFIED

2 of 2

8-A
023400



END
DATE
FILMED
8-8
DTIC

lower Mach number on the basis of γ reduction only, but the reduced viscous effects in these flows result in a thinner boundary layer thus raising the Mach number. The net result is a decrease in Mach number

to about 5.0. The 12.5% SF_6 -Ar appears to be dominated more by the γ and heat addition effect than by the effects of lower viscosity, resulting in an exit Mach number of 4. The increased viscous effects in the helium flows are evident by their much reduced Mach numbers in spite of the fact that helium has a high γ . Neither the He nor the 12% SF_6 -He mixture reaches a plateau.

Consider now the results of Nozzle 1 relative to Nozzle 7. Careful inspection of the contours in Fig. 3 reveal that Nozzle 1 has a slower area expansion near the throat but a more rapid increase in the latter part. Thus small changes in viscous effects between Ar and the 3 and 6% Ar- SF_6 mixtures produce larger differences in Nozzle 1 due to the slower opening throat area. This results in higher exit Mach numbers with increased mole fraction of SF_6 up to 6% (See Fig. 9B). However, the helium mixtures perform consistently better in Nozzle 1. The small section near the throat is about as detrimental as it is in Nozzle 7, however the downstream section with a more rapid opening will reduce the viscous dissipation in this region. The viscous effects in the argon expansions are minimal in this section for both nozzles. The 12.5% SF_6 -He mixture reaches a Mach number plateau above 4 bar. Thus the data provide some indication of what nozzle features influence gas expansions with different viscous effects (i.e. Reynolds number $Re = \rho u D / \mu$ where ρ is density) and specific heat ratios.

In addition to the Mach number, other dimensionless parameters are calculated. Reynolds number is used to characterize viscous effects, Knudsen number (and its inverse Kn^{-1}) is an indication if and when rarefied gasdynamics is of importance, and Prandtl number Pr indicates the relative importance of thermal to viscous boundary layers. Prandtl number is $Pr = \mu c_p / k$ where c_p is the constant pressure specific heat and k is the thermal conductivity and does not vary greatly through the nozzle or with changes in p_0 . Typical values for Ar are 0.65 to 0.7 and for SF_6 0.44 to 0.48. Representative values for Re and Kn^{-1} as a function of p_0 for Nozzle 7-B are shown in Fig. 10. Reynolds and Knudsen numbers ($Kn = \lambda / D$ where λ is the mean free path) range over two orders of magnitude. This is true for all SF_6 -Ar, but He and SF_6 -He have about an

order of magnitude greater variation. There is less than a factor of 2 change with pressure.

If relationships can be established for boundary layer effects, they could then be used to predict many of the nozzle characteristics without having to conduct gasdynamic experiments. One such correlation is given in Fig. 11. The boundary layer thickness δ is estimated here using the Pitot pressure traverses across the exit of the nozzle. Core flow is taken as that part of the profile which is flat and the remainder is assumed to be boundary layer. The displacement thickness δ_d is estimated using M_R to get an isentropic area A_I and $A_G/A_I = r^2/(r-\delta_d)^2$. The results provide the magnitude of the boundary thickness, with $\delta > \delta_d$ as it should be, and $\delta = r$ (fully developed flow at the exit) for $Re < 4,000$. Pitot and static pressure data for several nozzles and gases are converted to Mach number which, when compared to geometric Mach number, is related to the displacement thickness. When plotted as a function of $Re^{1/2}$ (related to laminar boundary layer growth) times Pr (ratio of thermal to viscous boundary layer thickness) the results fall along lines having a monotonic variation with kinematic viscosity, $\nu = \mu/\rho$ (see Fig. 12).

COMPARISON TO SOLUTION OF GOVERNING EQUATIONS

A complete two-dimensional solution to the equations of motion with viscosity and heat conduction along with nucleation and growth of the condensed phase, with its attendant latent heat release, would constitute an enormous undertaking both in terms of man-years and computer funds. The authors feel this is not warranted in terms of the goals of this work which require an understanding primarily of the centerline flow. A one-dimensional approach, incorporating some of the two-dimensional features for momentum and energy transport, has been developed. It includes the important physical phenomena for the flow process but this compromise requires that several features be characterized by parameters. They are adjustable but must be chosen in a self-consistent and physically meaningful way. The particular approach chosen here is not unique in the sense that it is the only way to pursue a simplified description of this process. It has, however, provided some theoretical guidance and insight with modest use of computer time.

Detailed computations for the case of 3% SF_6 -Ar expansions have been carried out for Nozzle 7. The one-dimensional steady state equations for conservation of mass, momentum and energy have been employed with an additional term for viscous effects in the momentum equation and a term for heat conductivity within the gas in the energy equation:

$$\rho Au = \dot{m} \quad \text{Continuity,} \quad (8)$$

$$dp + \rho u du = dP_v \quad \text{Momentum,} \quad (9)$$

$$d\left(h + \frac{u^2}{2}\right) = dq + dP_k \quad \text{Energy,} \quad (10)$$

where ρ is density, A is nozzle cross sectional area, u is velocity, \dot{m} is mass flow rate and is constant for steady flow, p is pressure, h is enthalpy and q is the latent heat release per unit mass due to phase change, i.e. $dq = Ldg$ where L is the latent heat for the condensible (SF_6 here) and g is the mass condensed per mass of mixture (carrier gas, condensible vapor and condensate). The quantities dP_v in the momentum equation (9) and dP_k in the energy equation (10) are "Production" terms due to the transport of momentum (viscous effects) and energy (heat conduction) to the centerline flow. Density and enthalpy are for the mixture including the condensed phase if present, i.e. $\rho = \rho_i + \rho_v + \rho_k$ and $h = h_i + h_v + h_k = c_{p_i}T + c_{p_v}T + cT$. The subscript i is for the inert carrier gas (Ar or He), v is for the condensible vapor (SF_6) and k for the condensed phase. The specific heat at constant pressure is c_p and c is the condensed phase specific heat. The perfect gas equation of state is

$$p = (1-g)\rho RT/\bar{m}_g \quad \text{State,} \quad (11)$$

where T is temperature and \bar{m}_g is the molecular weight of the gas mixture which changes as condensation begins due to vapor depletion, thus $(1-g)\rho = \rho_g$.

The boundary conditions at the solid wall are the no slip velocity condition and no heat exchange, i.e. an adiabatic wall. However, due to temperature gradients in the boundary layer, energy transport occurs within the gas resulting in heat flow from the periphery inwards. For those situations where the boundary layers grow together making a fully developed flow, the two transport terms are brought into use in the governing equations.

The term dP_v in Eqn. (9) is then

$$dP_v = \mu \frac{\partial^2 u}{\partial r^2} dx \quad (12)$$

(see e.g. Ref. 20 Eqn. 2-24a) and dP_k in Eqn. (10) becomes

$$dP_k = k \frac{\partial^2 T}{\partial r^2} + \frac{\partial T}{\partial r} \frac{\partial k}{\partial r} + \mu u \frac{\partial^2 u}{\partial r^2} + \frac{1}{2} \left(\frac{\partial u}{\partial r} \right)^2 + u \frac{\partial \mu}{\partial r} \frac{\partial u}{\partial r} \quad (13)$$

(see e.g. Ref. 20 Eqn. 7-5) where μ is the dynamic viscosity and k is the thermal conductivity.

Since only the centerline flow is of interest in molecular beam applications, solutions of the entire two dimensional flow field are not desired and would represent a substantial effort to attain. The viscous and heat conduction "production" terms of Eqns. (12) and (13) are essential for a physically meaningful description of the centerline flow. An integral approach is used¹⁶ in which the production term in each volume element $dV = 2\pi r dr dx$ is summed over the flow volume cross section slice between x and $x + dx$ (see Fig. 3) and divided by the slice volume to give an average value (for either dP_v or dP_k)

$$\overline{dP} = \frac{\int_0^{r_w} 2\pi r dP dr dx}{\int_0^{r_w} 2\pi r dr dx} \quad (14)$$

In order to evaluate Eqn. (14) the functions $u=u(r)$, $T=T(r)$, $\mu=\mu(T)$ and $k=k(T)$ must be specified.

Data for the temperature dependence of the viscosity and the thermal conductivity of Ar^{21} and SF_6^{22} are fitted with linear functions. The velocity distribution is assumed to be parabolic, where fully developed, going from zero at the wall to a maximum at the centerline (subscript c):

$$u(x,r) = u_c(x)(1-r^2/r_w^2) \quad (15)$$

where r_w is the radial distance to the wall. The temperature profile is also assumed to be parabolic rising from the value at the centerline $T_c(x)$ to an adiabatic wall temperature T_{aw} . The use of a temperature recovery factor of the form $r = (T_{aw}-T_c)/(T_0-T_c)$ is frequently used in viscous flow²⁰ where T_0 is the stagnation temperature $\approx 295k$. For a Prandtl number near unity (0.7) $r \approx 0.86$ giving $T_{aw} = 0.14 T_c(x) + 258$. The temperature distribution then becomes

$$T(x,r) = T_c(x) + \Delta T(r^2/r_w^2), \quad (16)$$

where $\Delta T = T_{aw}-T_c$.

The average value of the transport or "Production" term, Eqn. (14), for viscosity and heat conduction can now be evaluated and they are

$$\overline{dP_v} = \frac{-2u_c}{r_w^2} \frac{dx}{dr} \left(\mu_c + \frac{3}{2} \frac{d\mu}{dT} \Delta T \right), \quad (17)$$

and

$$\overline{dP_k} = \frac{dx}{P_c u_c} \left[\frac{2\Delta T}{r_w} \left(k_c + \frac{3}{2} \frac{dk}{dT} \Delta T \right) + \frac{u_c^2}{r_w} \left(\mu_c + \frac{d\mu}{dT} \frac{\Delta T}{3} \right) \right], \quad (18)$$

where $d\mu/dT$ and dk/dT are obtained from the straight line curves fitted through the temperature dependent μ and k and averaged for the particular mole fraction of Ar and SF_6 at that x position.

Since the radial gradients dT/dr and du/dr are small near the flow centerline, the production terms dP_v and dP_k in Eqns. (9) and (10) should be a small fraction, call it F_μ of the volume averaged term over all r . Thus we can write

$$dP_v = F_\mu \overline{dP_v}, \quad (19)$$

and

$$dP_k = F_\mu \overline{dP_k},$$

The use of the integral technique eliminates the need for the actual velocity profiles so that $\overline{dP_v}(\overline{dP_k})$ is not sensitive to the details of the velocity (temperature) distribution. Typical values of F_μ used to calculate the transport properties on the centerline are in the range 0.0001 to 0.0005. The point at which fully developed flow begins and ends can be varied in the program.

It should be stressed here that the radial distribution of properties are used only to compute the value of the production terms dP_v and dP_k (Eqns. (17) and (18) substituted into Eqn. (19)) which appear in Eqns. (9) and (10). The solution to the governing equations of motion, Eqns. (8), (9), (10) are carried out with the use of an equation of state, Eqn. (11), plus droplet nucleation and growth equations described by Eqns. (21) and (22). They are solved as a closed set of one-dimensional (x) flow equations with phase change and transport terms for viscosity and heat conduction. The boundary layer effects are handled in the usual way²³ with a displacement thickness δ_d which grows from zero thickness at the nozzle entrance to a value at the exit, δ_d , characterized by a non-dimensional thickness $\lambda = \delta_d/r_{wc} = 2\delta_d/D_p$. The values for the centerline properties used in calculating dP_v and dP_k are taken as those obtained from the one-dimensional solutions.

The variation of displacement thickness with x is provided for using an exponential growth equation giving the equivalent nozzle diameter as

$$D(x) = 2r_w(x) = \delta_d(x) \frac{N}{\lambda} \quad (20)$$

where x_0 is the distance from nozzle entrance to exit and N is varied typically from 1 (i.e. linear) to 2.

In addition to the gasdynamics, equations to describe the droplet nucleation and growth are also included.²³⁻²⁵ Due to the relatively high cooling rates for gases passing through these small nozzles, a correction to the steady state nucleation theory²⁶⁻³² is incorporated.²⁹ The steady state nucleation theory is applicable for nozzle cooling rates of up to 10^6 °C/sec. Cooling rates of 10^9 °C/sec, typical of free jet expansions, are thought to be too high to be dealt with using the nucleation rate theory. The nozzles in this paper have cooling rates in the range of 10^7 - 10^8 where adjustments to the steady state theory are expected to apply (Corrections by a factor of 2-4 at most).

The steady state nucleation theory is a function of the thermodynamic variables obtained in conjunction with the solution to the governing equations (8)-(11),

$$J = \left(\frac{p_v}{kT}\right)^2 \left(\frac{2\sigma}{\pi m}\right) v_c \exp(-\Delta G^*/kT), \quad (21)$$

where J is the number of critical size (*) clusters formed $\text{cm}^{-3} \text{ sec}^{-1}$ and $\Delta G^* = 4\pi r^{*2}\sigma/3$ is the Gibbs free energy of formation of a critical size cluster, i.e. the size which is large enough to become a stable droplet of condensed SF_6 . Here p_v is the SF_6 vapor pressure, k is Boltzmann's constant, σ is the SF_6 surface tension, m is the mass of an SF_6 molecule and v_k is the volume of one SF_6 molecule in the condensed phase. The critical radius is $r^* = 2\sigma v_k/kT \ln S$, where S is the SF_6 saturation ratio, $S = (p_v/p_{v\infty})_T$ with $p_{v\infty}$ the SF_6 vapor-liquid equilibrium pressure at temperature T .

Since the cluster size is small compared to the mean free path of the gas and since the condensate (SF_6) is a small fraction (3%) of the argon carrier gas, the droplet growth law is that obtained from elementary kinetic theory with a condensation coefficient α near 1.0. Thus the growth law is

$$dO/dt = \alpha \beta O, \quad (22)$$

where O is the droplet area $O = 4\pi r^2$ and β is the SF_6 impingement rate per unit area, $\beta = p_v/(2\pi mkT)$. Taking proper account of the number of droplet formed at x , $N(x)$, plus the growth of previously nucleated clusters, the mass fraction condensed can be computed, $w(x)$, and since dq/dx Eqns. (21) and

(22) provide dq and g in Eqns. (3) and (4).

To summarize: Eqn. (19) provides the production or transport terms when boundary layer effects penetrate to the flow centerline, Eqn. (20) provides the effective nozzle area A , Eqns. (21) and (22) provide dq and g , and $h=h(T)$. Therefore Eqns. (8)-(11) can be considered, after the above substitutions, as 4 equations in 4 unknowns, p , ρ , T and u .

Due to the high cooling rates in these nozzles, and densities typically falling less than 1% of the starting density, vibrational relaxation for the SF_6 molecule is included using published relaxation times.³³ The program calculates all the thermodynamic variables, gasdynamic properties including velocity and Mach number, details of the phase change including nucleation rate, number of droplets formed, and size. The primary concern here is to match the gasdynamic properties, i.e. p_1 and p_{02} . These data for the 3% SF_6 -Ar in Nozzle 7 are plotted as the circles in Fig. 13. As p_0 is increased the boundary layer thickness δ , the displacement thickness δ_d , the centerline production dP_v and dP_k , and the length of centerline viscous effects x^+ are all changing. The calculation procedure holds these parameters constant while p_0 is varied and thus the theoretical results represent "planes" crossing the plane of the experimental data in a hyperspace.

Upon examining many sets of computer results using a systematic variation in parameters a reasonable and consistent picture of the nozzle flow is obtained. The Pitot pressure data seen in Fig. 13 (b) are intersected with lines of constant Δ . It is found that variation of N , F_μ and x^+ all have virtually no effect on p_{02} . Thus Pitot pressure is determined once Δ is fixed for a given inlet p_0 . The variation of Δ from 0.65 to 0.5 as p_0 increases from 3 to 8 bar, shown indirectly in Fig. 13(b) and explicitly in Fig. 14(a), is qualitatively correct since as the density increases the transport of momentum and energy from the nozzle wall is decreased giving thinner boundary layers. Below 3 bar viscous effects (F_μ) are important as well as Δ for the values of p_{02} .

Static pressure p_1 is much lower than p_{02} and changes in most of the listed parameters produce small fractional changes in the static pressure. (The accuracy of the experimental data is $\pm .02$ torr.) Variation in boundary layer growth, N in Eqn. (20), results in a change of slope for p_1 vs p_0 in Fig. 13 (a). The best match to the slope of the data occurs for $N=1.5$ which was then used for all the calculations presented.

here. The magnitude of p_1 for a given p_0 is then determined by fixing F_μ . The Pitot data below 2 bar fall below the calculated values. This is believed to be due in part to a drop in measured Pitot pressure from that of the true Pitot pressure at low probe Reynolds numbers (i.e. less than 100) which are encountered in the flows at low p_0 . Even when corrected they fall below the curves for $\delta = 0.5-0.6 r_{we}$. In this range the viscous effects are quite prevalent since boundary layers get thicker at lower Re and at 1 bar an increase of F_μ to 0.0008 still does not match the Pitot data. An upper value for F_μ used here is set at that value which drives the Mach number subsonic.

In addition to the theoretical comparison to pressure measurements shown in Fig. 13 the results for Δ and M_G are summarized in Fig. 14. Displacement thickness Δ varies from 0.5 to 0.65 with exit Mach number leveling off at 5.4. The computed results are numbered, with the conditions for the program given in Table III. Since the program is run with discrete choices for parameters, the fit, although close, is not expected to be perfect in every case. The somewhat lower values of Δ , compared to those obtained from measurement, is qualitatively correct since Δ is based on boundary layer displacement thickness while the measurements in Fig. 11 are velocity boundary layers and thus $\delta > \delta_d$ as expected.

DISCUSSION

Flows at higher pressures have thinner boundary layers, and smaller centerline viscous dissipation occurring only in the early part of the expansion. The boundary layer becomes fully developed shortly inside the nozzle entrance where the diameters and θ_T are very small. Further downstream where the nozzle angle opens up more rapidly we assume that a boundary layer edge reappears, leaving a core flow with very little viscous dissipation, i.e., nearly isentropic but with a value of entropy greater than the starting value. This is consistent with the Pitot traverses normal to the flow at high pressures which have flat profiles near the center, indicating flat velocity profiles and thus little viscous effects in this region. As the pressure decreases the Reynolds number will decrease and the boundary layer increases. Thus the point at which a boundary layer edge reforms will occur progressively further down the nozzle, resulting in a profile with a flat section that is a smaller portion of the flow. For $p_0 \leq 2$ bar the flow remains fully developed along the entire nozzle except for a very short inlet region. Here the theoretical calculation

allow the possibility for the flow actually to go from supersonic to subsonic again due to viscous effects. This is similar to heat addition in condensing supersonic flows. As the nozzle opens up downstream the flow can again become supersonic.

It should again be emphasized that the amount of dissipation seen in these flows is relatively small, that is, in the range of 0.02-0.1% of the average dissipation at any given nozzle cross-section where the flow is fully developed. This picture is consistent with all of the gasdynamic data. In addition the phase change droplet nucleation and growth calculations in this program predict condensation in agreement with both measurement of laser light scattering and ionization gage beam detection in the molecular beam configuration.³⁴ (There is experimental and theoretical evidence for condensation approaching 100% of the condensable species in the higher pressure runs.³)

However for some flow conditions and especially with light carrier gases such as helium, viscous dissipation can be prevalent to such an extent that nozzles become less efficient than free jet expansions.³⁵ Nozzles have been designed so that nucleation of small mole fractions of noble gases in a helium carrier gas can be used for beam experiments.³⁵ In pure SF_6 expansions the boundary layers remain thin even in the very small entrance sections of several of the nozzles so that an isentropic core was maintained all the way to the exit. Analysis of the data using one-dimensional gasdynamics, along with the calculation of thermodynamic properties and dimensionless quantities, has provided a means for designing small nozzle sources to encourage or indeed discourage condensation.

ACKNOWLEDGMENTS

The authors would like to thank Mr. Sang-Soo Kim for use of the argon molecular beam results shown in Fig. 1 and Mr. Diancheng Shi for the large orifice data in Fig. 8. One of us (GDS) thanks Prof. Alan L. Kistler for valuable suggestions and comments with respect to several aspects of both data and theoretical analysis. We are grateful to Mr. James F. Morris, the glassblower who made our nozzles, and Mr. Robert D. Klaub and his Machine Shop for construction of the remainder of the apparatus. We also wish to acknowledge the Engineering Energetics section of the National Science Foundation and the Power Branch of the Office of Naval Research for partial support of this research.

REFERENCES

1. O. F. Hagena and W. Obert, J. Chem. Phys., 56, 5 (1973)
2. O. F. Hagena, in Molecular Beams and Low Density Gas Dynamics, edited by P. P. Wegener, (Marcel Dekker, New York, 1974), p. 93
3. S. S. Kim, B. G. DeBoer, and G. D. Stein, in Rarefied Gas Dynamics, edited by R. Campargue, (Commissariat a L'Energie Atomique, Paris, 1979), p. 1151
4. W. Obert, in Rarefied Gas Dynamics, edited by R. Campargue, (Commissariat a L'Energie Atomique, Paris, 1979), p. 1181
5. B. J. C. Wu, P. P. Wegener, and G. D. Stein, J. Chem. Phys., 69, 1776 (1978)
6. B. J. C. Wu and G. A. Laguna, J. Chem. Phys., 71, 2991 (1979)
7. S. S. Fisher, Phys. Fluids 22, 1261 (1979)
8. E. W. Becker, H. Falter, O. F. Hagena, W. Henkes, R. Klingelhöfer, H. O. Moser, W. Obert, and I. Poth, Nucl. Fusion 17, 617 (1977)
9. E. W. Becker, H. Falter, O. F. Hagena, W. Henkes, R. Klingelhöfer, H. O. Moser, W. Obert, and I. Poth, in 1st Symposium on the Production and Neutralization of Negative Hydrogen Ions and Beams, (Brookhaven National Laboratories, Long Island, New York, 1977)
10. T. Takagi, I. Yamada, K. Yanagawa, M. Kunori, and S. Kobiyama, J. Appl. Phys. Suppl. 2, Pt. 1, 427 (1974)
11. A. Kantrowitz and J. Grey, Rev. Sci. Instrum. 22, 328 (1951)
12. G. B. Kistiakowsky and W. P. Slichter, Rev. Sci. Instrum. 22, 333 (1951)
13. J. B. Anderson, in Molecular Beams and Low Density Gas Dynamics, edited by P. P. Wegener, (Marcel Dekker, New York, 1974), p. 1
14. R. L. Smalley, B. L. Ramakrishna, D. H. Levy, and L. Wharton, J. Chem. Phys., 61, 3463 (1974)

15. R. E. Smalley, L. Wharton, and D. H. Levy, in Accounts of Chemical Research, edited by J. Bunnett, (American Chemical Society, Washington, D.C., 1977), Vol. 10, p. 139
16. A. L. Kistler (private communication)
17. J. L. Potter and A. B. Bailey, AIAA J. 2, 743 (1964)
18. H. Ashkenas and F. S. Sherman, in Rarefied Gas Dynamics, edited by J. H. deLeeuw, (Academic, New York, 1975), Vol. II, p. 84
19. J. B. Fenn, S. B. Ryali, and M. P. Sinha, Final Report on Contract #954327 to the Jet Propulsion Laboratory (1977)
20. F. M. White, Viscous Fluid Flow, (McGraw-Hill, New York, 1974) pp. 576-581
21. The Matheson Unabridged Gas Data Book, Argon booklet, p. 4 and 7 (Matheson Gas Products, East Rutherford, New Jersey, 1974)
22. The Matheson Unabridged Gas Data Book, Sulfur Hexafluoride booklet, p. 7 and 9 (Matheson Gas Products, East Rutherford, New Jersey, 1974)
23. P. P. Wegener and A. A. Pouring, Phys. Fluids, 7, 352 (1964)
24. B. J. C. Wu, Report to Office of Naval Research, available from National Technical Information Service, No. A0775257. (1974)
25. C. A. Moses and G. D. Stein, J. Fluids Eng., 100, 311 (1978)
26. A. Kantrowitz, J. Chem. Phys., 19, 1097 (1951)
27. R. F. Probstein, J. Chem. Phys., 19, 619 (1951)
28. H. Wakeshima, J. Chem. Phys., 22, 1614 (1954)
29. F. C. Collins, Z. Elektrochem., 59, 404 (1955)
30. R. P. Andres and M. Boudart, J. Chem. Phys., 42, 2057 (1965)
31. J. Feder, K. C. Russel, J. Lothe, and C. M. Pound, Advan. Phys., 15, 111 (1966)
32. F. F. Abraham, J. Chem. Phys., 51, 1632 (1969)
33. W. D. Breshears and L. S. Blair, J. Chem. Phys., 59, 5824 (1973)

34. O. Abraham, S. S. Kim, and G. D. Stein, submitted to J. Chem. Phys.
35. S. S. Kim, D. C. Shi, and G. D. Stein, Twelfth International Symposium on Rarefied Gas Dynamics, University of Virginia, July, 1980

TABLE I
Nozzle Geometry

Nozzle Number	D _o cm	bc cm	L cm	θ_T Deg	θ_N Deg	a _o	a ₁	a ₂	a ₃	a ₄	a ₅	a ₆	a ₇
1	0.0137	0.256	3.05	1.78	4.61	0.0137	-0.0982	0.3843	-0.4834	0.3189	-0.0984	0.0113	0
4	0.0063	0.256	3.15	2.01	4.58	0.00635	-0.0248	0.1488	-0.1156	0.0450	-0.00637	0	0
6	0.0119	0.256	2.31	7.31	6.56	0.0119	0.1038	-0.0404	0.1133	-0.065	0.0102	0	0
7	0.0127	0.218	3.0	2.95	3.83	0.01277	-0.01553	0.1555	-0.18189	0.09671	-0.0058	-0.0092	0.0018

TABLE II
Gasdynamic Data

Nozzle	Gas	P ₀ Bar	P ₁ Torr	P ₀₂ Torr	M _R
1	Ar	3	1.459	53.84	4.98
		4	1.663	60.65	4.95
		5	1.866	68.93	4.98
		6	2.067	75.40	4.95
		7	2.27	81.87	4.92
	0.125 SF ₆ -He	3	2.13	20.78	2.69
		4	2.54	80.43	4.94
		5	2.92	93.37	4.96
	SF ₆	3	1.244	34.79	4.88*
		4	1.562	43.06	4.84
		5	1.82	51.68	4.87
		6	2.121	58.87	4.86
		7	2.421	66.78	4.84
	0.125 SF ₆ -Ar	2	1.31	23.65	3.71
		3	1.584	33.15	4.12
		4	1.866	45.93	4.35
		5	2.113	56.0	4.51
		6	2.303	63.18	4.60
		7	2.63	66.78	4.42
	0.03 SF ₆ -Ar	2	1.236	36.99	4.58
		3	1.452	56.43	5.23
		4	1.743	68.53	5.26
		5	1.881	75.0	5.30
		6	2.107	82.47	5.25
		7	2.332	87.42	5.14
	0.0625 SF ₆ -Ar	2	1.235	28.68	4.11
		3	1.487	51.68	5.04
		4	1.690	66.06	5.35

* Because γ for SF₆ is a function of temperature the first iteration for M_R is obtained using $\gamma(T_0)$ which is then used to estimate exit temperature T₀ and $\gamma(T_0)$ then used to get the final value of M_R.

TABLE II
Gasdynamic Data (Cont.)

Nozzle	Gas	P ₀ Bar	P ₁ Torr	P ₀₂ Torr	M _R
		5	1.922	79.00	5.49
		6	2.174	87.62	5.44
		7			
		8	2.655	92.85	5.06
		9	2.898	102.0	5.08
	He	3	2.80	10.92	0.50
		4	3.18	29.11	2.43
		5	3.43	79.0	3.91
		6	3.62	158.6	5.42
		7	3.82	255.55	6.72
		8	4.03	352.09	7.69
4	Ar	2	0.485	1.37	1.25
		3	0.683	1.97	1.27
		4	0.870	2.66	1.32
		5	0.959	3.44	1.45
		6	1.008	7.12	2.12
		7	1.06	10.83	2.57
		8	1.11	15.60	3.03
		9	1.18	19.28	3.28
		10	1.24	22.93	3.50
	SF ₆	4	0.575	4.82	2.68
		5	0.630	8.27	3.38
		6	0.713	12.30	3.86
		7	0.749	14.60	4.10
		8	0.865	18.05	4.24
	0.063 SF ₆ -Ar	4	0.840	2.52	1.35
		5	0.935	4.82	1.86
		6	1.010	7.70	2.30

TABLE II
Gasdynamic Data (Cont.)

Nozzle	Gas	P ₀ Bar	P ₁ Torr	P ₀₂ Torr	M _R
		7	1.095	10.57	2.61
		8	1.170	13.45	2.86
6	Ar	2	0.939	33.0	4.86
		3	1.093	44.5	5.23
		4	1.215	55.28	5.53
		5	1.326	59.59	5.50
		6	1.422	65.34	5.56
		7	1.501	71.09	5.65
	SF ₆	2	0.694	22.21	5.19
		3	0.789	31.56	5.76
		4	0.900	38.75	5.97
		5	1.025	45.21	6.03
		6	1.146	50.25	6.02
		7	1.211	56.00	6.17
	0.03 SF ₆ -Ar	2	0.637	22.21	4.95
		3	1.095	44.50	5.35
		4	1.187	54.56	5.70
		5	1.277	61.75	5.84
		6	1.352	68.93	6.00
		7	1.487	73.96	5.93
	0.0625 SF ₆ -Ar	2	0.932	16.46	3.57
		3	1.115	37.31	4.95
		4	1.229	55.28	5.75
		5	1.382	63.18	5.79
		6	1.433	71.09	6.04
		7	1.525	79.0	6.17
	0.125 SF ₆ -Ar	2	0.925	18.62	3.93
		3	1.120	28.68	4.44

TABLE II
Gasdynamic Data (Cont.)

Nozzle	Gas	P ₀ Bar	P ₁ Torr	P ₀₂ Torr	M _R
		4	1.275	38.75	4.84
		5	1.410	48.81	5.17
		6	1.475	56.0	5.42
		7	1.608	63.18	5.52
	He	2	1.581	5.68	1.45
		3	2.115	10.0	1.70
		4	2.376	21.50	2.41
		5	2.527	47.37	3.52
		6	2.666	90.50	4.77
		7	2.775	127.87	5.57
	0.125 SF ₆ -He	2	1.190	7.12	2.07
		3	1.458	27.25	3.78
		4	1.739	45.93	4.51
		5	1.990	55.28	4.63
		6	2.130	61.75	4.73
		7	2.314	67.50	4.74
	7	2	1.401	36.40	4.16
		3	1.753	76.12	5.40
		4	1.873	80.43	5.37
		5	2.083	87.62	5.32
		6	2.288	102.0	5.48
		7	2.490	109.18	5.43
	0.125 SF ₆ -He	3	2.344	18.62	2.42
		4	2.834	33.71	2.99
		5	3.272	49.65	4.00
		6	3.681	119.20	5.00
	0.03 SF ₆ -Ar	2	1.433	27.25	3.00
		3	1.701	64.62	5.17

TABLE II
Gasdynamic Data (Cont.)

Nozzle	Gas	P ₀ Bar	P ₁ Torr	P ₀₂ Torr	M _R
		4	1.947	80.43	5.40
		5	2.169	89.06	5.38
		6	2.365	96.25	5.36
		7	2.572	105.59	5.38
		8	2.764	113.30	5.38
	0.063 SF ₆ -Ar	2	1.402	25.09	3.59
		3	1.751	51.68	4.64
		4	2.003	73.25	5.17
		5	2.231	89.06	5.41
		6	2.423	102.00	5.56
		7	2.658	112.06	5.56
	SF ₆	2	1.106	27.96	4.65
		3	1.41	39.46	4.88
		4	1.728	48.09	4.56
		5	2.066	56.0	4.80
		6	2.437	64.62	4.75
		7	2.868	71.09	4.60
		8	3.220	79.0	4.58
	He	4	3.641	20.06	1.85
		5	4.000	44.5	2.69
		6	4.245	90.5	3.77
		7	4.467	162.37	4.94
	0.125 SF ₆ -Ar	2	1.409	24.37	3.63
		3	1.790	37.31	3.99
		4	2.099	44.5	4.03
		5	2.427	54.56	4.15
		6	2.693	66.06	4.34

TABLE III
COMPUTER SOLUTIONS FOR NOZZLE 7-B, 3% SF₆-Ar

Run No.	P ₀ torr	Δ	F _μ	x _μ [†]	P ₁ torr	P ₀₂ torr	M
1	1	0.6	0.0006	0.88	1.03	20.4	3.64
2	1	0.6	0.0008	0.88	1.15	20.2	3.44
3	2.2	0.6	0.0002	0.37	1.46	n.c.	4.62
4	2.5	0.58	0.0002	0.37	1.63	46.7	4.39
5	3	0.6	0.0001	0.37	1.57	60.9	5.10
6	3.5	0.6	0.0001	0.37	1.72	71.2	5.28
7	4	0.6	0.0001	0.37	1.88	n.c.	5.40
8	5	0.6	0.0001	0.37	2.21	n.c.	5.58
9	6	0.55	0.0003	0.37	2.16	98.3	5.19
10	7	0.52	0.0004	0.37	2.57	101.8	5.16
11	8	0.52	0.0004	0.37	2.78	116.6	5.31

n.c. - not calculated.

FIGURE CAPTIONS

- Fig. 1 Nozzle 7 is compared to a free jet source in a molecular beam configuration. The relative beam intensity, I_B , primarily measures cluster intensity and shows the enormous advantage of the nozzle over the free jet. (Values of I_B greater than 100 are intense enough for experimental use.)
- Fig. 2 The experimental arrangement permits nozzles and exit sections to be interchanged. Light scattering is used to detect condensation, M - mirror, L - lens, S - slit, FO - fiber optic, PMT - photomultiplier and BT - beam trap. The Pitot probe has x-y-z motion capability.
- Fig. 3 The four glass nozzles discussed in this paper are shown expanded 8:1 in diameter in order to see the qualitative differences. A 1:1 contour of Nozzle 7 shows the actual geometry. Three exit sections A, B, and C were attached to the nozzles to test the effect of nozzle length and to provide a static pressure tap in the case of exit sections A and B (See Table I for additional details.) The upper part of the figure shows the coordinates for the solution to the equations of motion plus the boundary layer displacement thickness.
- Fig. 4 The exit Mach number for Nozzle 7 is plotted as dash lines for exit A and solid lines for exit B. The Mach number M_s is based on the static pressure measurement, Eqn. (4), M_p is based on the Pitot measurements and Eqn. (5), and M_R is based on both measurements at the exit and Eqn. (6). The geometric Mach number M_G is based on area ratio only, i.e., no viscous effects, and is the upper limit. The correct Mach number is M_R and the deviation from the other Mach numbers is due to viscous effects. Note the closeness of the three Mach numbers in the case of SF_6 indicating little or no viscous dissipation in the "isentropic" core. The data provide increasing Mach numbers in the order M_R , M_s , and M_p at any given p_0 although the symbols overlap for the SF_6 case.

- Fig. 5 Pitot traverses, for varying stagnation pressure, are shown for Nozzle 6 (relatively large throat size) and Nozzle 4 (small throat size) for helium and argon flows both using exit configuration A shown in Fig. 1. A larger diameter nozzle provides more intense beams or higher exit Mach numbers. Nozzle 4 is virtually of no use with helium. (The nozzle exit diameter is D_e .)
- Fig. 6 Pitot traverses across the flow beyond the exit of Nozzle 1, Exit B, for argon are shown as a function of position downstream of the exit. Note the flat core section close to the nozzle exit which disappears progressively downstream. Here x is measured from 0.5 mm beyond the exit plane of the glass nozzle.
- Fig. 7 Pitot profiles for Nozzle 7-B as a function of p_0 are shown for argon, 3%, and 6.3% SF_6 in argon. For one gas the decrease in the core size with decreasing pressure is due to progressively thicker boundary layers, i.e. lower Reynolds numbers. The variation in core size and centerline Pitot pressure from one mixture to another is due to a combination of variation in γ and δ . The measurements were made in the exit plane of the glass nozzle (i.e., $x/D_e = -0.25$ in Fig. 6).
- Fig. 8 Pitot measurements are shown for two free jets with a factor of 25 difference in throat area and several gases. Mach number from Eqn. (5) is compared to the theoretical values given by Eqn. (7). This theory has been verified with numerous types of measurements and is applicable for the $x/D > 2$.
- Fig. 9 Mach numbers are plotted with properties based on the initial mole fractions for mixtures and are nearly independent of p_0 above 3 bar, except for He and He- SF_6 , while SF_6 is constant over the entire range. Nozzle 1 shows a slightly larger variation in exit Mach numbers for the Ar and Ar- SF_6 mixtures. The He- SF_6 mixture turns over toward a flat value in this nozzle but the pure helium does not.
- Fig. 10 Typical values of Reynolds number Re and inverse Knudsen number Kn^{-1} for Ar and SF_6 in Nozzle 7 are shown with θ - the throat properties and e - the exit. The characteristic dimension for both parameters is the nozzle diameter and shows that the flows are still collision dominated even at the lower pressures. A wider variation exists for He.

- Fig. 11 The exit boundary layer thickness, δ , divided by nozzle radius r is plotted as a function of exit Reynolds number. Pitot traverses provide δ using exit B or C. The upper limit of $(\delta/r)_e = 1.0$ represents a fully developed flow. The lower curve is the displacement thickness $(\delta_d/r)_e$ obtained from M_R .
- Fig. 12 The ratio M_R/M_G is an indication of the boundary layer displacement thickness and is shown as a function of $Re^{1/2} Pr$.
- Fig. 13 The static and the Pitot pressure data for 3% SF_6 -Ar in Nozzle 7 are compared with theoretical solutions shown as solid lines.
- Fig. 14 The parameters for the theoretical solutions of Fig. 14 are shown in part A. Part B compares the exit Mach number from the computer calculations, that include the variation of properties with temperature and condensation, to that obtained from the data and one-dimensional gasdynamics using isentropic exit properties and no phase change.

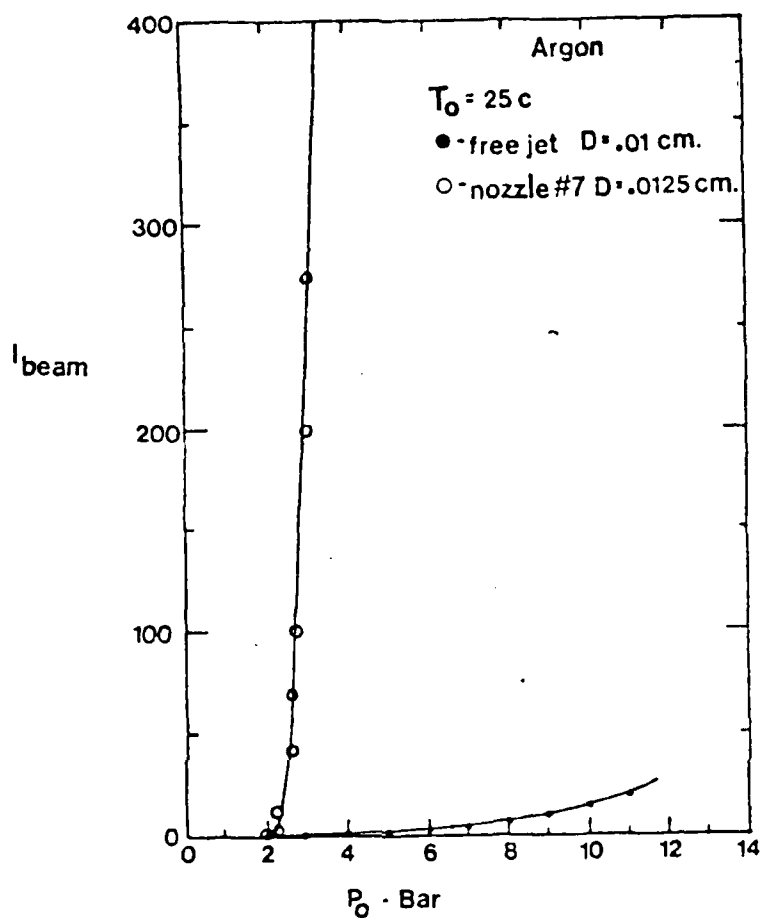


FIG. 1 Nozzle 7 is compared to a free jet source in a molecular beam configuration. The relative beam intensity I_B , primarily measures cluster intensity and shows the enormous advantage of the nozzle over the free jet. (Values of I_B greater than 100 are intense enough for experimental use.)

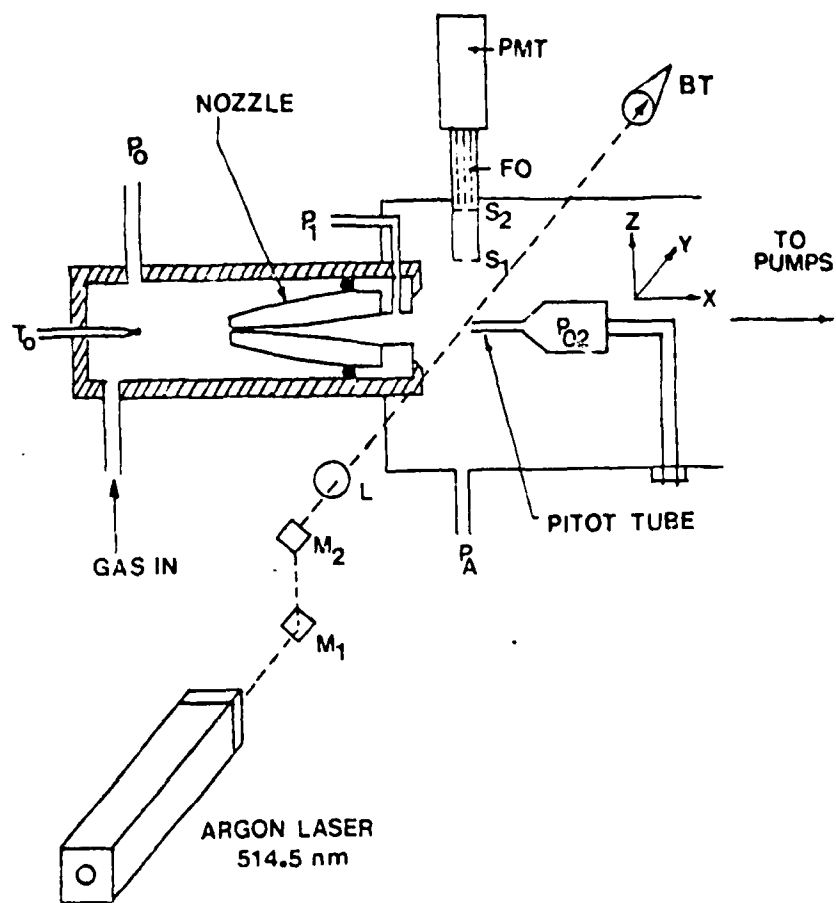


FIG. 2 The experimental arrangement permits nozzles and exit sections to be interchanged. Light scattering is used to detect condensation, M - mirror, L - lens, S - slit, FO - fiber optic, PMT - photomultiplier and BT - beam trap. The Pitot probe has x-y-z motion capability.

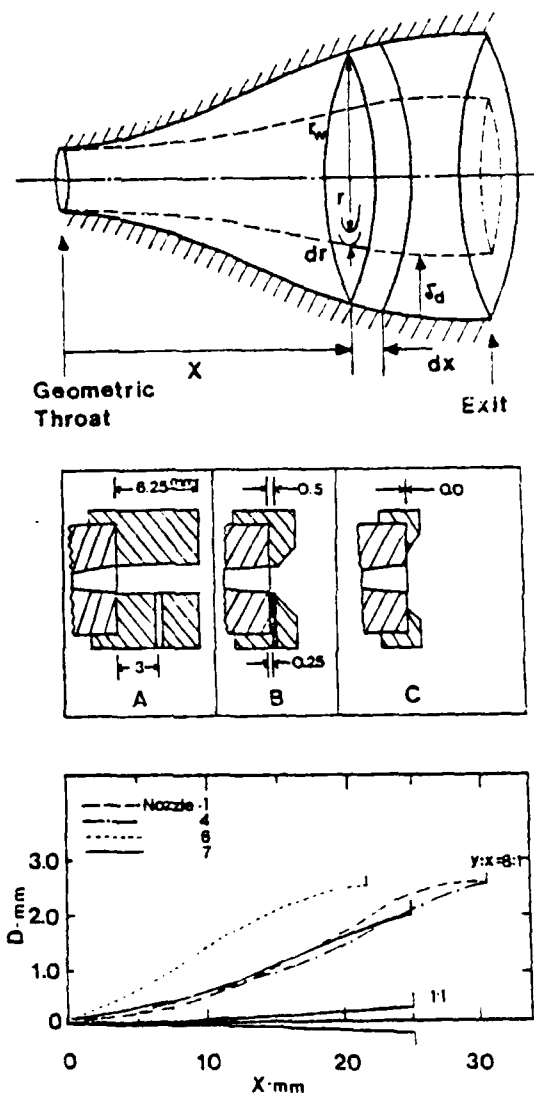


FIG. 3 The four glass nozzles discussed in this paper are shown expanded 8:1 in diameter in order to see the qualitative differences. A 1:1 contour of Nozzle 7 shows the actual geometry. Three exit sections A, B, and C were attached to the nozzles to test the effect of nozzle length and to provide a static pressure tap in the case of exit sections A and B (See Table I for additional details). The upper part of the figure shows the coordinates for the solution to the equations of motion, plus the boundary layer displacement thickness.

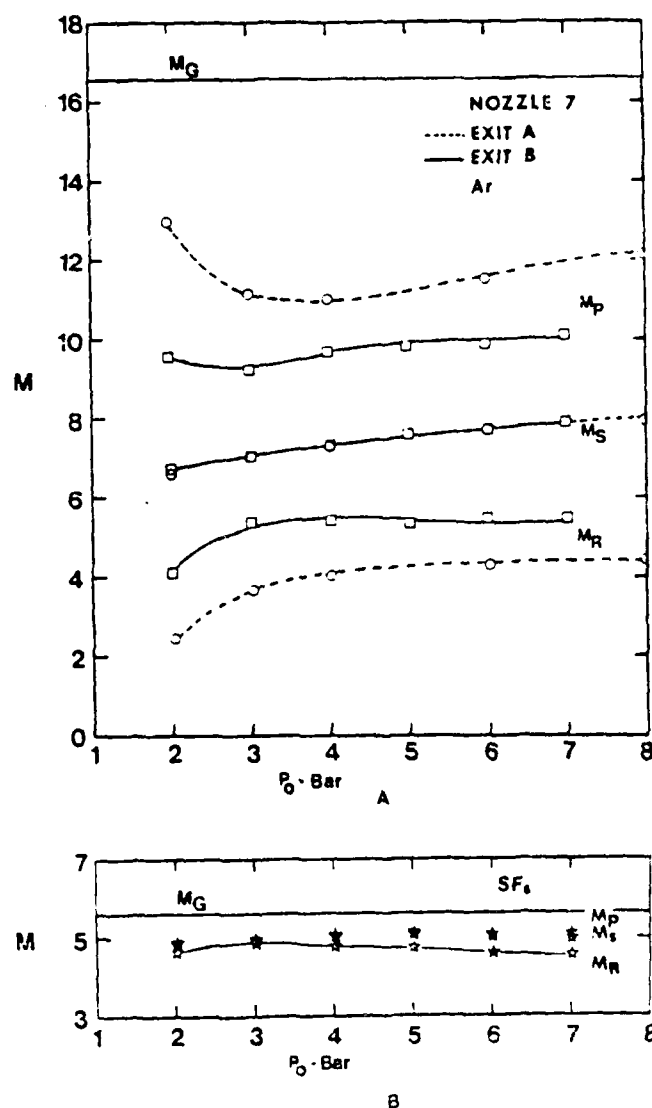


FIG. 4 The exit Mach number for Nozzle 7 is plotted as dashed lines for exit A and solid lines for exit B. The Mach number M_0 is based on the static pressure measurement, Eqn. (4), M_p is based on the Pitot measurements and Eqn. (5), and M_R is based on both measurements at the exit and Eqn. (6). The geometric Mach number M_0 is based on area ratio only, i.e., no viscous effects, and is the upper limit. The correct Mach number is M_R and the deviation from the other Mach numbers is due to viscous effects. Note the closeness of the three Mach numbers in the case of SF_6 indicating little or no viscous dissipation in the "isentropic" core. The data provide increasing Mach numbers in the order M_0 , M_p , and M_R at any given p_0 although the symbols overlap for the SF_6 case.

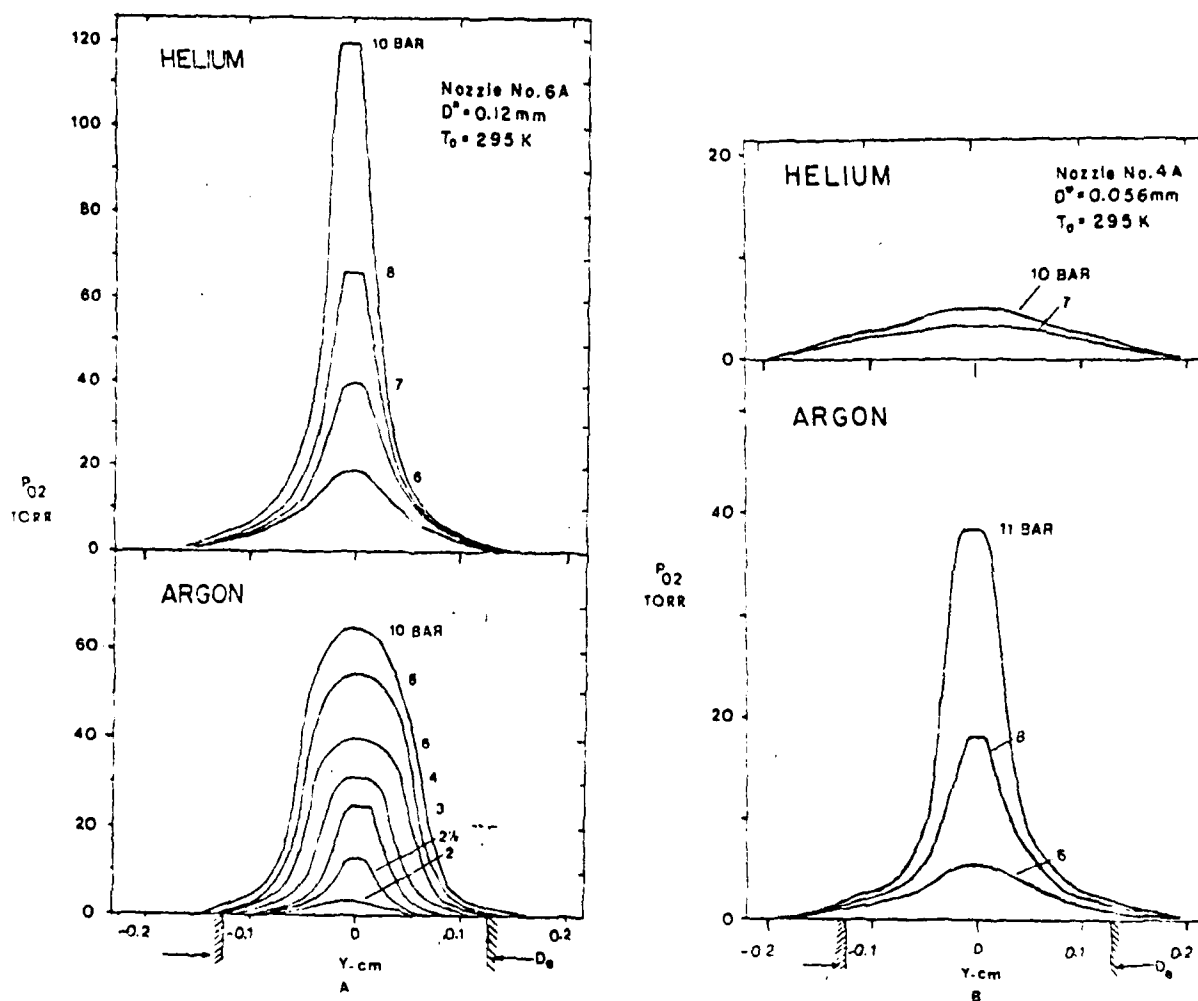


FIG. 5 Pitot traverses, for varying stagnation pressure, are shown for Nozzle 6 (relatively large throat size) and Nozzle 4 (small throat size) for helium and argon flows both using exit configuration A shown in Fig. 1. A larger diameter nozzle provides more intense beams or higher exit Mach numbers. Nozzle 4 is virtually of no use with helium. (The nozzle exit diameter is D_e .)

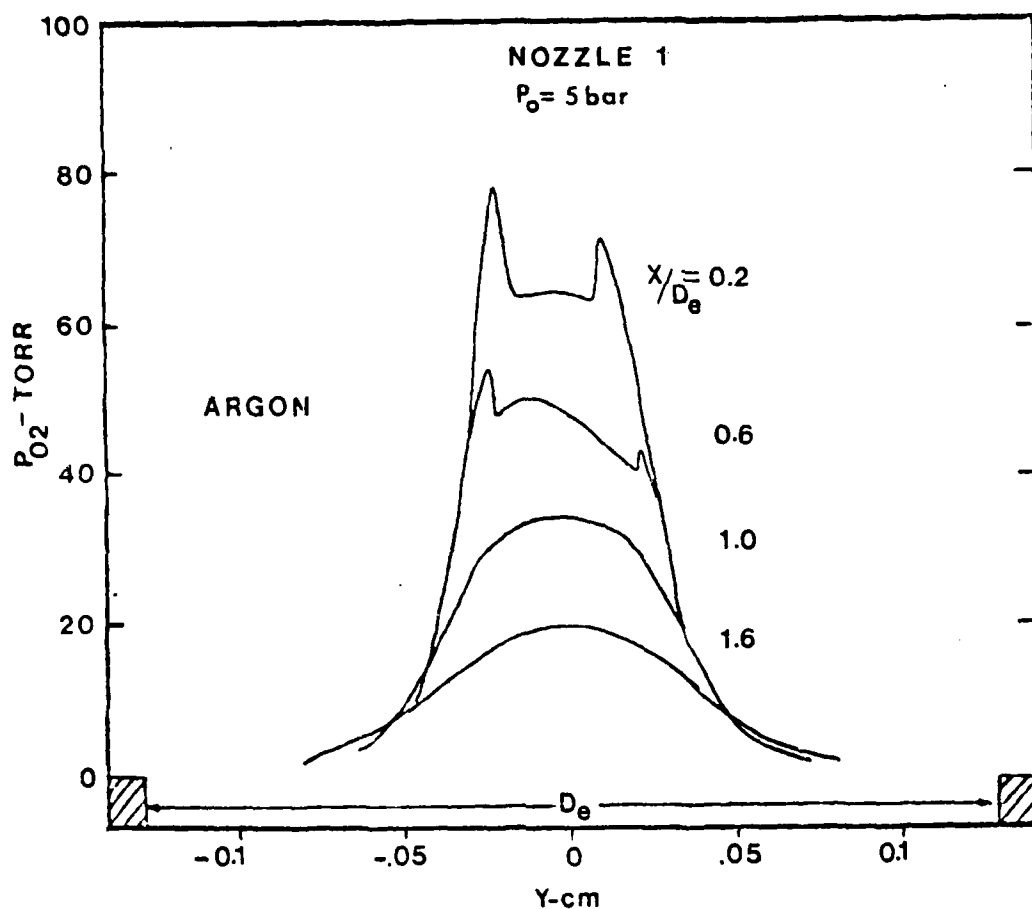


FIG. 6 Pitot traverses across the flow beyond the exit of Nozzle 1. Exit P_0 for argon are shown as a function of position downstream of the exit. Note the flat core section close to the nozzle exit which disappears progressively downstream. Here x is measured from 0.5 mm beyond the exit plane of the glass nozzle.

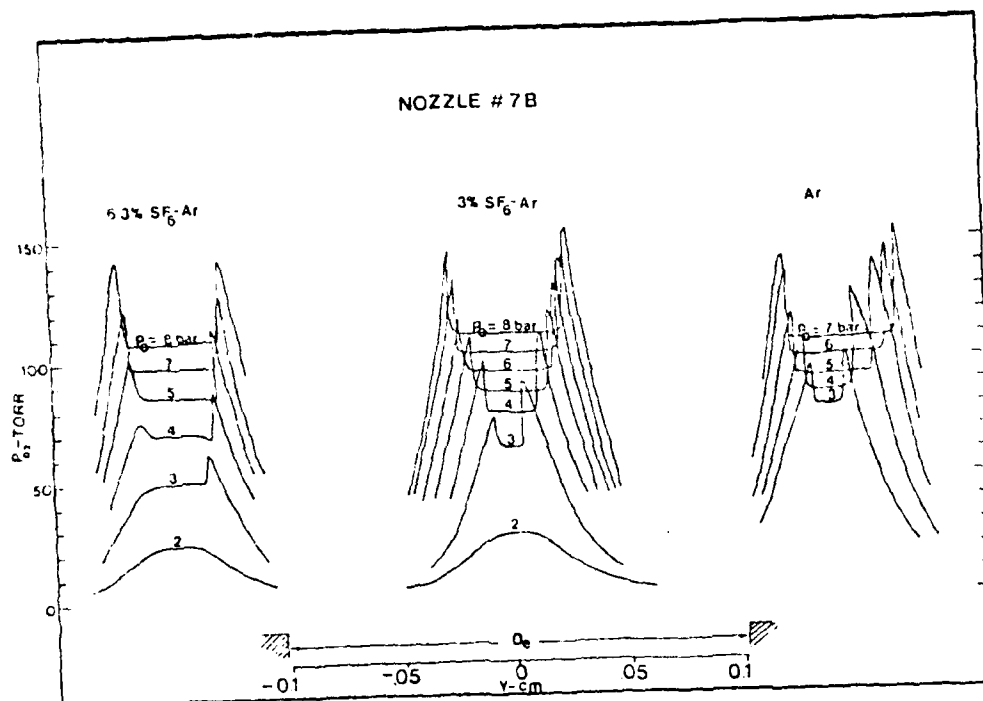


FIG. 7 Pitot profiles for Nozzle 7-3 as a function of p_0 are shown for argon, 3% and 6.3% SF_6 in argon. For one gas the decrease in the core size with decreasing pressure is due to progressively thicker boundary layers, i.e. lower Reynolds numbers. The variation in core size and centerline Pitot pressure from one mixture to another is due to a combination of variation in γ and β . The measurements were made in the exit plane of the glass nozzle (i.e., $x/D_0 = -0.25$ in Fig. 6).

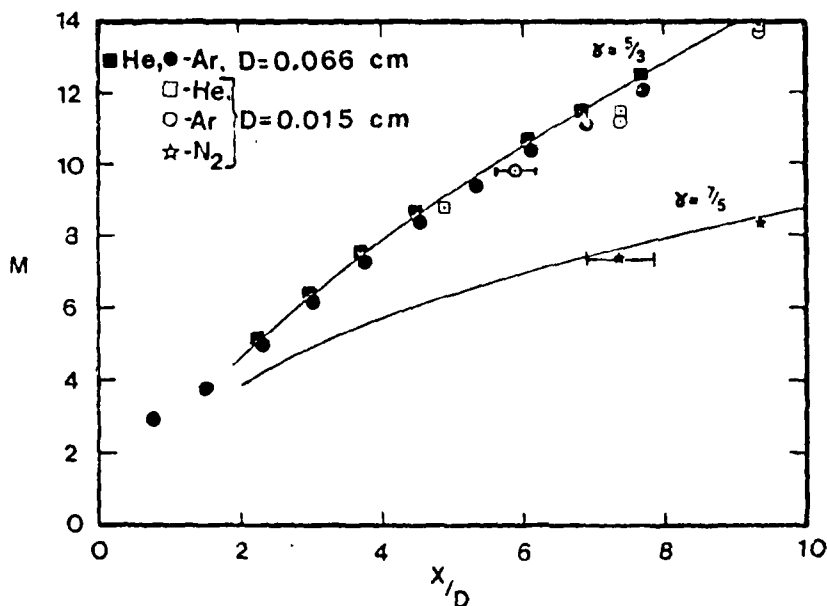


FIG. 3 Pitot measurements are shown for two free jets with a factor of 25 difference in throat area and several gases. Mach number from Eqn. (5) is compared to the theoretical values given by Eqn. (7). This theory has been verified with numerous types of measurements and is applicable for the $x/D > 2$.

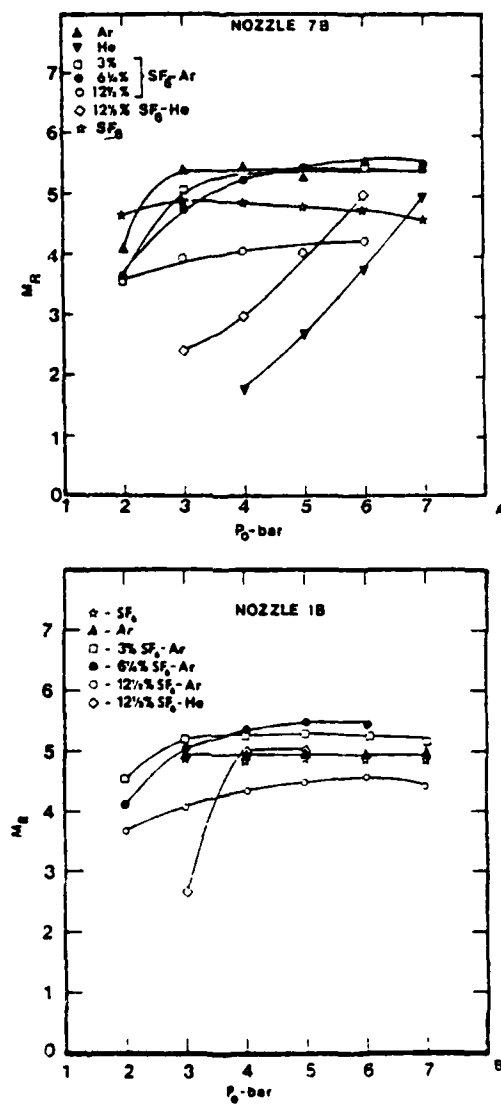


FIG. 9 Mach numbers are plotted with properties based on the initial mole fractions for mixtures and are nearly independent of p_0 above 3 bar, except for He and He- SF_6 , while SF_6 is constant over the entire range. Nozzle 1 shows a slightly larger variation in exit Mach numbers for the Ar and Ar- SF_6 mixtures. The He- SF_6 mixture turns over toward a flat value in this nozzle but the pure helium does not.

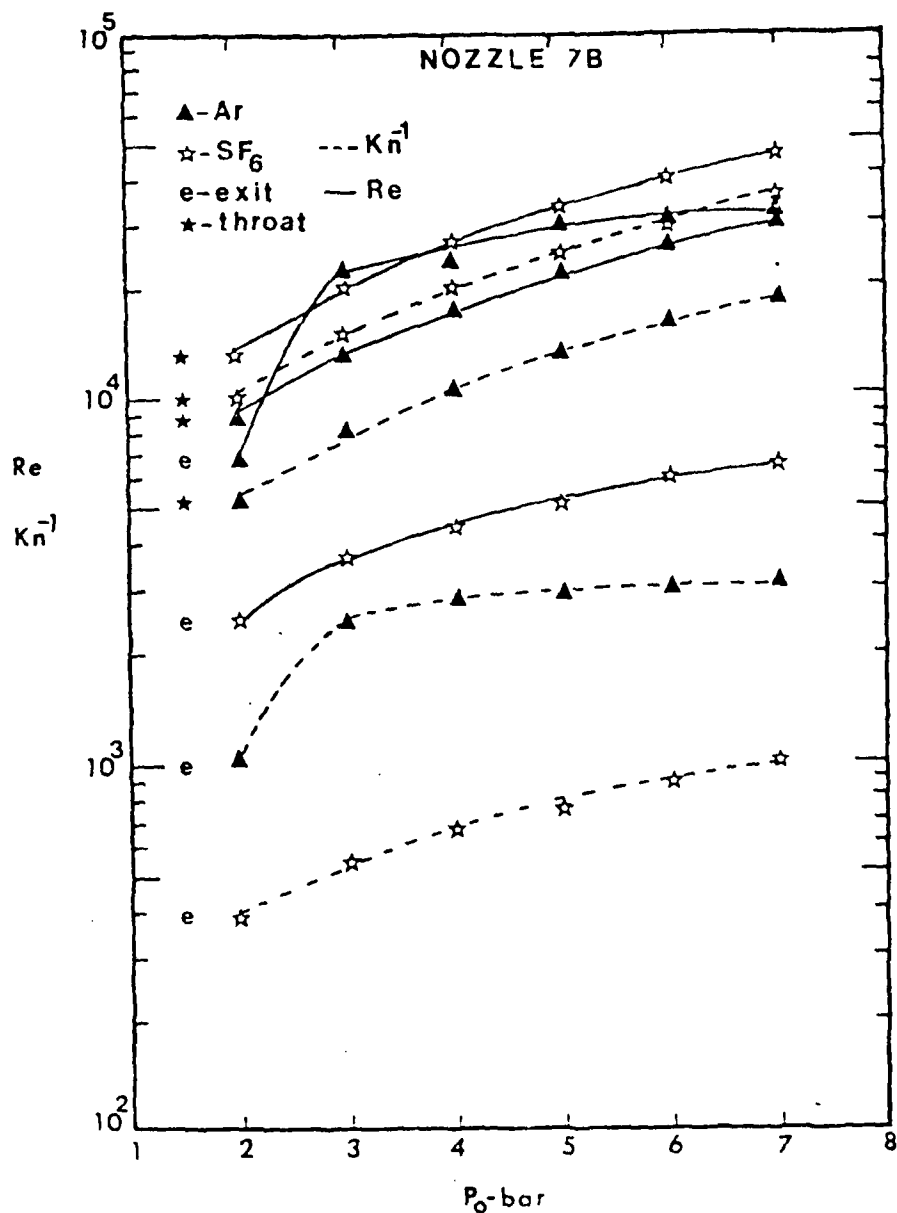


FIG. 10 Typical values of Reynolds number Re and inverse Knudsen number Kn^{-1} for Ar and SF_6 in Nozzle 7 are shown with * - the throat properties and e - the exit. The characteristic dimension for both parameters is the nozzle diameter and shows that the flows are still collision dominated even at the lower pressures. A wider variation exists for He.

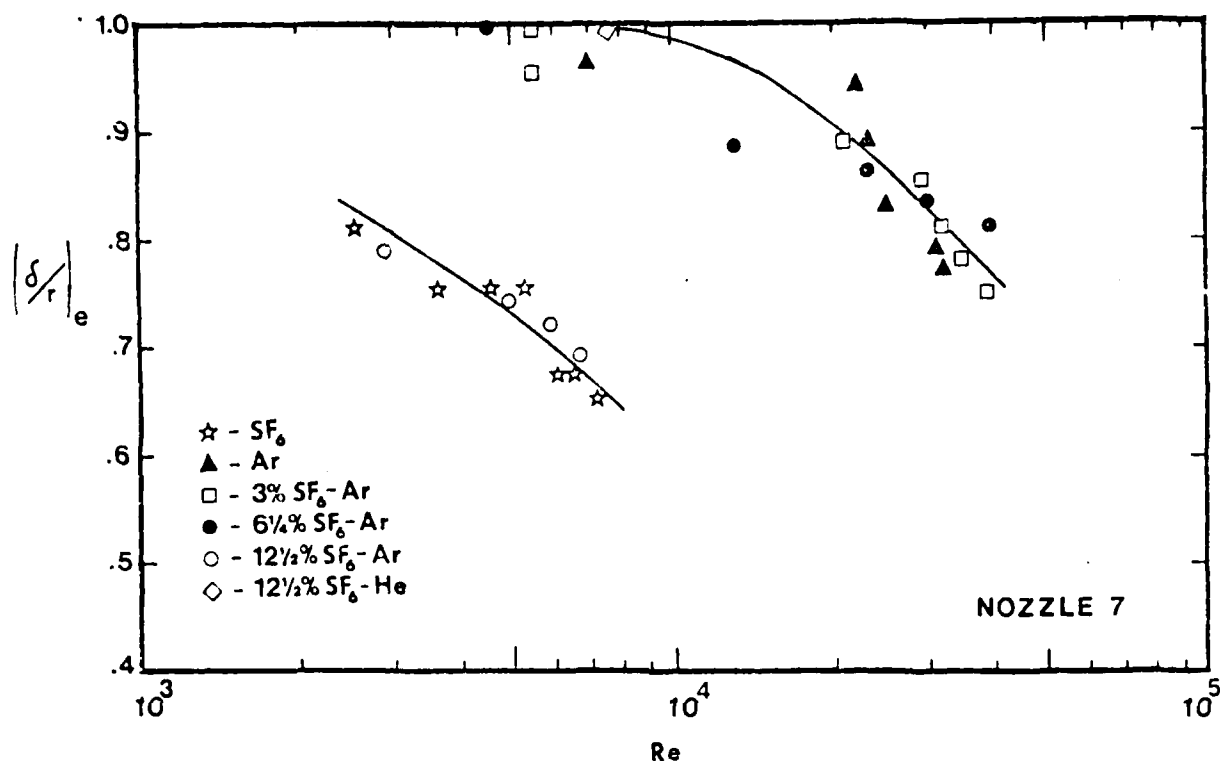


FIG. 11 The exit boundary layer thickness, δ , divided by nozzle radius r is plotted as a function of exit Reynolds number. Pitot traverses provide δ using exit B or C. The upper limit of $(\delta/r)_e = 1.0$ represents a fully developed flow. The lower curve is the displacement thickness $(\delta_d/r)_e$ obtained from M_f .

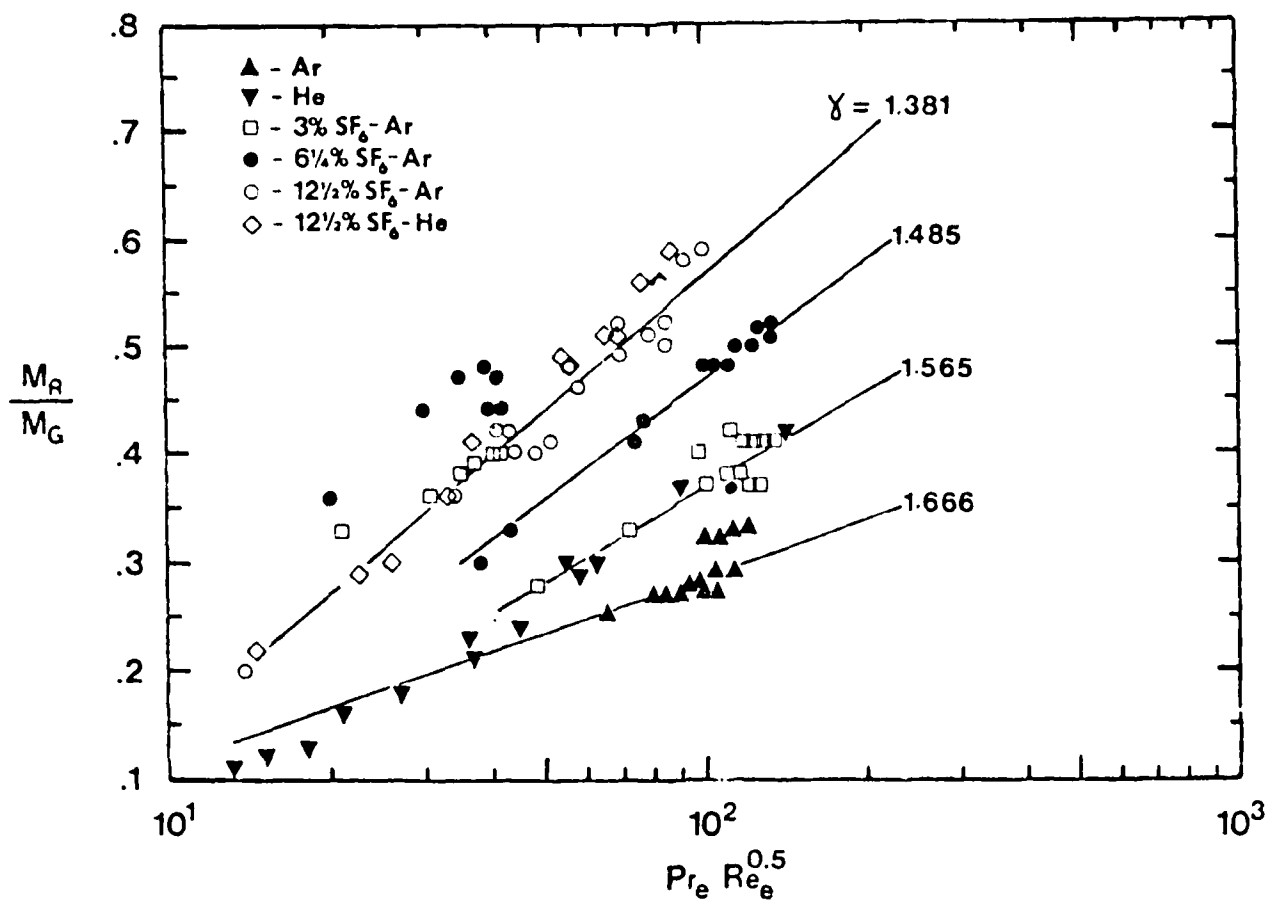


FIG. 12 The ratio M_R/M_G is an indication of the boundary layer displacement thickness and is shown as a function of $\text{Re}^{0.5} \text{Pr}$.

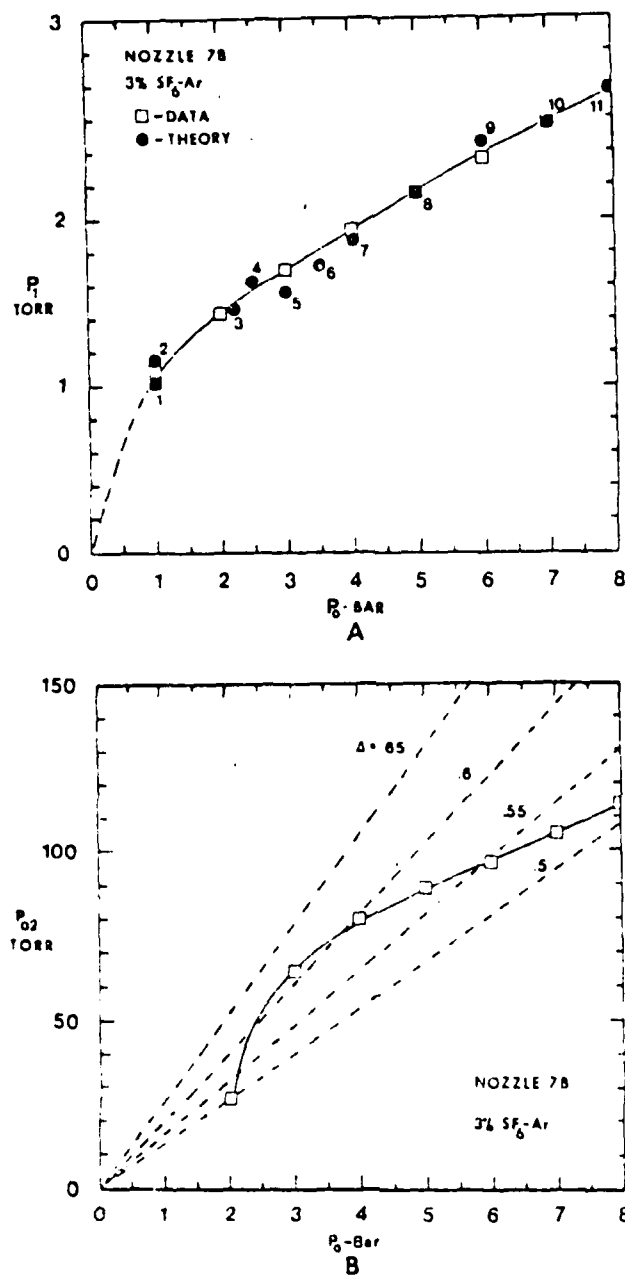
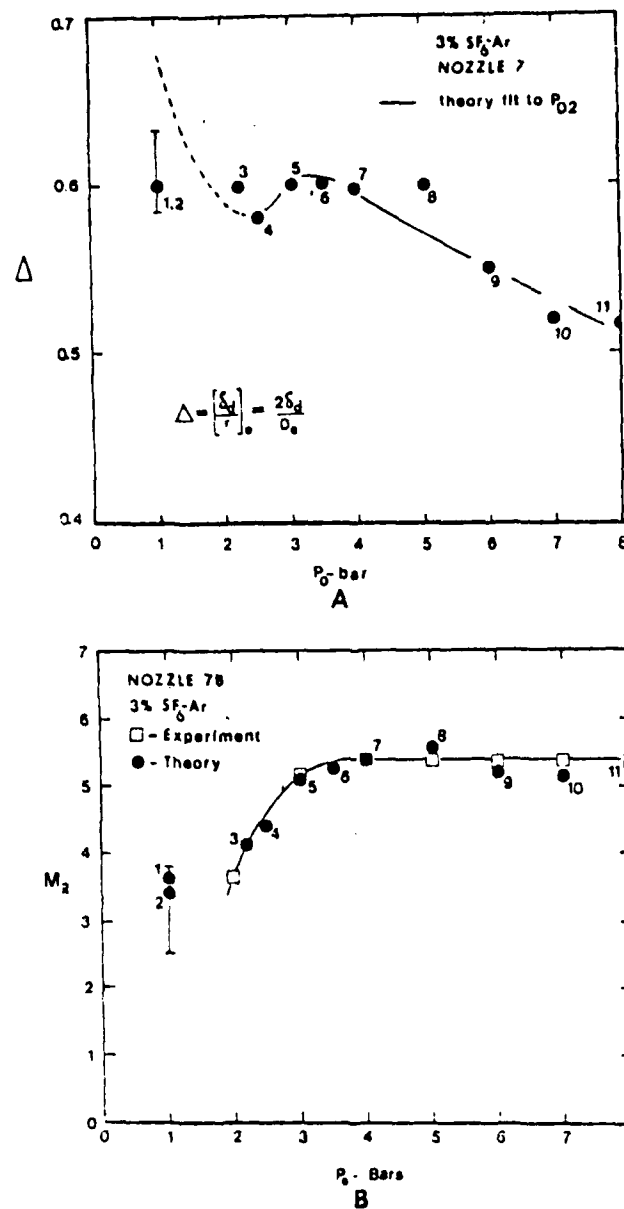


FIG. 13 The static and the Pitot pressure data for 3% SF₆-Ar in Nozzle 7 are compared with theoretical solutions shown as solid lines.



NOBLE GAS CONDENSATION IN CONTROLLED-EXPANSION BEAM SOURCES

S. S. Kim, D. C. Shi and G. D. Stein

to appear in Rarefied Gas Dynamics
American Institute of Aeronautics and Astronautics, New York, N.Y.

NOBLE GAS CONDENSATION IN CONTROLLED-EXPANSION BEAM SOURCES

Sang Soo Kim,^{*} Dian Cheng Shi,[†] and Gilbert D. Stein[‡]

Northwestern University, Evanston, Ill.

Abstract

Over the past several years an investigation into the gasdynamic and nucleation properties of very small Laval nozzles has been undertaken in our laboratory due to their great potential use as sources in cluster molecular beams. A series of nozzles designed specifically for helium carrier gas expansions has been tested in our molecular beam apparatus and used to study the condensation of the noble gases, Ar, Kr, and Xe. The goal of producing cluster beams with densities high enough to carry out high energy electron diffraction experiments has been attained for these gases with mean cluster sizes in the range of 100-400 atoms per cluster. The onset of nucleation appears to correlate with the product of nozzle diameter, starting pressure, and atomic potential well depth: i.e., $p_0 D_0$ e/k.

Introduction

It is well known that supersonic nozzles can have their contours designed to control, within limits, the rate of expansion and that they can be very much more efficient in nucleating a particular gas than uncontrolled, free-jet expansions having the same throat diameter.¹⁻⁴ Nozzles made of varying throat diameter, exit diameter, and nozzle length have

Presented as Paper 145 at the Twelfth International Symposium on Rarefied Gas Dynamics, Charlottesville, Va., July 7-12, 1980. Copyright American Institute of Aeronautics and Astronautics, Inc., 1980. All rights reserved.

^{*}Gas Dynamics Laboratory, Department of Mechanical and Nuclear Engineering.

[†]Gas Dynamics Laboratory, Department of Mechanical and Nuclear Engineering. On leave from the Institute of Electronics Academia Sinica, People's Republic of China.

[‡]Gas Dynamics Laboratory, Department of Mechanical and Nuclear Engineering.

been built and tested. They have been instrumented so that the following data can be obtained: stagnation pressure p_0 , temperature and T_0 , nozzle exit static pressure p_1 , pitot pressure measurements p_{02} near the nozzle exit, and pitot traverses parallel and normal to the flow direction.

The experimental arrangement is shown in Fig. 1a. The nozzle source is mounted with xyz motion capability and is shown with a diverging Laval nozzle installed. If pitot (i.e. impact) measurements are to be made, the skimmer S is removed and a probe and pressure transducer mounted so as to separate the first and second pumping chambers. Replacement of the skimmer re-establishes the standard molecular beam configuration. The cluster beam is crossed by a 40 keV electron beam for diffraction studies and Debye-Scherrer patterns are taken with a single channel, electron scintillator, photon counting detection system using phase-sensitive detection and a chopped molecular beam.

The contours for the nozzles used in this work are shown in Fig. 1b. The throat diameters vary from 0.05 to 0.1 mm and exit diameters range from 2 to 5 mm. The nozzles are diverging with the minimum diameter at the entrance. The subsonic flow ahead of the entrance is not important for the nucleation process. Their contours have been measured and fitted to a tenth order polynomial as shown in Table I. Nozzle 4 has the smallest divergence angle ($<1^\circ$ total included angle) and is longer than the other nozzles. The noble gas experiments discussed here were obtained using nozzles 11, 12 and 13. They were designed to determine the effect of throat diameter D_0 and nozzle contour on their performance as cluster sources. Nozzles 12 and 13 have the same contour except near the nozzle entrance. Nozzle 11 diverges more rapidly than 12 and 13 near the inlet.

Gasdynamics

Extensive gasdynamic measurements using a variety of gases and gas mixtures reveal that a large fraction of the nozzle flow lies within a boundary layer with some viscous dissipation occurring all the way to the centerline.^{3,5} Thus, in order to correctly determine the local Mach number at any point in the nozzle, one must measure both static and pitot pressure since the total pressure in the flow will decrease due to

viscous effects. The only point where both pressures are measured in this work is at the nozzle exit. The Mach number is obtained using the so-called Rayleigh supersonic pitot equation,

$$\frac{p_1}{p_{02}} = \left(\frac{2\gamma}{\gamma+1} M_R^2 - \frac{\gamma-1}{\gamma+1} \right)^{\frac{1}{\gamma-1}} \left(\frac{\gamma+1}{2} M_R^2 \right)^{-\frac{\gamma}{\gamma-1}} \quad (1)$$

where γ is the local value of the specific heat ratio. The exit Mach number M_R is shown in Fig. 2 for several gas mixtures, all of which are 6 mole % in a helium carrier gas ($x_0 = 0.06$). This Mach number is seen to increase monotonically with p_0 , to values as high as 10. The three solid curves are for nozzle 12 but with different condensable species. For $p_0 < 4$ bar the Mach numbers are nearly the same but increase with molecular weight, i.e., from Ar to Kr to Xe. Above 4 bar the curves reverse with Ar having the highest Mach numbers for a given p_0 . For Xe a comparison for the three nozzles 11-13 is shown. Nozzle 12 gives the highest Mach number for a given p_0 and nozzle 11 (same throat size but more rapid expansion) is second highest. Nozzle 13 (same contour as 12 but smaller entrance diameter D_0) exhibits the lowest Mach numbers.

With the system arranged in its molecular beam configuration, beam intensities were measured using an ionization gage (IG in Fig. 1). The nozzle-to-skimmer distance, x_s , was varied to determine its effect on beam intensity. Pure argon expansions are shown in Fig. 3. Note that intensity variations with x_s/D_e are not large. There is an interesting variation in maximum beam intensity going from a downstream peak location, double peak, and upstream location as p_0 is increased, analogous to some free jet cluster source data.^{6,7} All beam experiments were carried out with $x_s = 2.5$ mm. This gives a value of $x_s/D_e \approx 0.5$ for nozzle 13 which is optimum for the high p_0 beams as seen in Fig. 3.

Although Laval nozzles are much more efficient cluster sources than free jets for most flows, care must be taken in their design or they can actually produce beam intensities lower than a free jet source. Consider for example the expansion of SF_6 ($x_0 = 0.125$) through nozzle 4 shown in Fig. 4. When expanded in an argon carrier gas the beam intensity

increases dramatically near $p_0 = 2.5$ bar due to clustering. However, for helium carrier gas (same specific heat ratio γ) the beam intensities remain quite low even out to $p_0 = 8$ bar. Thus this nozzle is of little use for helium carrier gas, condensation experiments with T_0 near room temperature.

Because a high γ carrier gas is required for condensation of a low γ gas in an adiabatic expansion, and because the Laval nozzles control the rate of expansion but cannot limit the maximum Mach number in these expansions, He is desirable since it is unlikely to supersaturate and cause mixed condensable-carrier gas clusters. The use of pure gas expansions is also an option, provided γ is not too near 1, but does not allow for the possibility of controlling the cluster size distribution or temperature that is potentially available using a carrier gas. In addition there is the problem of the high cost of some pure gases such as Xe. As a result of these criteria and prior experience with nozzles having long, small divergence inlets, e.g., nozzle 4, several shorter nozzles that diverge more rapidly have been constructed.

There are, however, a number of problems using He rather than other commonly used carrier gases such as Ar or N_2 . Boundary layer effects are more severe due to its higher kinematic viscosity. In addition there is the problem of reduced high vacuum diffusion pump performance. (i.e., for nozzles with $D_0 > 0.1$ mm pressure fluctuations of an order of magnitude or more occurred in the second and third stage pumping chambers when $p_0 > 2$ bar.) Thus in order to operate at sufficiently high p_0 for cluster beam generation, it is necessary to decrease the nozzle throat size below 0.1 mm. This exacerbates the problem of helium boundary layer growth so that nozzle design must be carefully considered.

Nucleation

Measured molecular beam intensities for He-carried Ar, Kr, and Xe with $x_0 = 0.06$ are shown in Fig. 5 for nozzle 12 and $T_0 \approx 295$. As one might expect, condensation occurs in the order Xe, Kr, and Ar as p_0 is increased. All the molecular beam intensity data are given in fixed, arbitrary units (a.u. in Figs. 3-7) with 10 approximately equal to 2×10^{18} atoms/($\text{cm}^2 \text{ s}$) at the electron beam location. Once the beam intensity, I_b , exceeds unity (a.u.) the beam density is sufficient for electron diffraction measurements. Because all three of these gases are noble gases, one is tempted to look for some universal behavior. Thus normalizing to Xe, these three curves are replotted as dotted lines with the ordinate equal to $p_0 \epsilon/k$

where ϵ is the interatomic potential well depth⁸ and k Boltzmann's constant. When replotted the onset of condensation occurs at the same value of $p_0 \epsilon/k$ for the three gases.

A plot of these data as a function of a nondimensional or reduced pressure $p_0/(\epsilon/\sigma^3)$ or $p_v/(\epsilon/\sigma^3)$, where σ is the radius for zero interaction potential⁸ and p_v is the condensable vapor partial pressure, provided no unification of the onset point.

For a given species and mole fraction nucleation results from one nozzle to another will be compared. The results for Ar, $x_0 = 0.25$, for nozzles 11-13 are shown in Fig. 6. The solid lines are for the data plotted as a function of p_0 in which the onset of nucleation, for the nozzles with the two largest diameters, occurs first. Nozzle 12, with a lower expansion rate than nozzle 11, exhibits more rapid growth of the condensed phase after the point of onset since the measured beam intensity beyond onset is due entirely to the condensed phase. As with free jet cluster sources, these data have also been plotted vs $p_0 D_0$ (dashed lines) such that the curve for nozzle 12 is unchanged. Recall that $p_0 D_0$ is proportional to the total number of binary collisions per atom for a given expansion. Here again it is interesting to note that detectable condensation onset occurs at a single point on the $p_0 D_0$ scale. Note, however, that the three curves would also converge to a common onset point were they plotted versus $p_0 D_0$ which is proportional to the three-body collision frequency required to form a stable dimer in the initial cluster formation process. These results, although interesting are not universal, as seen in Fig. 7 for Xe, $x_0 = 0.06$ expansions. In this case the onset of nucleation in nozzle 11 occurs at lower p_0 than that of nozzle 12 and their growth curves cross over at a pressure above onset. When replotted as a function of $p_0 D_0$ the results from nozzles 12 and 13 (which have the same nozzle contour but different D_0) fall nicely on top of one another whereas the results from nozzle 11 move slightly further away (see Fig. 7). Thus the correlation with binary or trimolecular collision frequency is not perfect, but

then the various nozzles have flow histories which are not as universal as those of the free jet expansions.

Electron Diffraction

Electron diffraction patterns have been taken with our single channel detection system for all three condensable noble gases under a variety of conditions and using several nozzles. An average cluster size can be estimated from the measured broadening of the diffraction rings. Knowing the density of the condensed phase, the number of atoms per cluster may then be calculated. The results for Xe, $x_0 = 0.06$ are shown in Fig. 8. The sizes are in the $\bar{g} = 100-1000$ atoms per cluster range. The sizes of Fig. 8 correlate with the relative intensities of Fig. 7 in that a given I_p and \bar{g} occur for progressively higher p_0 in the order nozzle 11, 12, and 13. Recall that \bar{g} comes from a diffraction peak which is a sum of the diffraction from a large number of clusters that cross the electron beam. There is always a distribution of sizes in the beam, and since the scattering intensity at a diffraction peak goes as the square of the number of atoms in a cluster, the larger clusters scatter more electrons. Thus \bar{g} is weighted toward the high end of the size distributions. Theoretical models for the noble gas clusters in this size regime predict the possibility of icosahedral packing in contrast to the bulk FCC structure.^{9,10} The comparisons we have made between data and cluster models have so far shown better agreement using icosahedral rather than the bulk structure.

Conclusions

We have arrived at the following conclusions with regard to small Laval nozzle, noble gas clustering:

1) Noble gases, even when a small mole fraction expanded in helium, readily nucleate.

2) Because of the high kinematic viscosity of helium the nozzle contour must be carefully designed to balance off the effects of increased boundary layer growth and the requirement that throat diameter be small to avoid pumping problems.

3) There is tantalizing evidence that a parameter $p_0 D_0^2 s/k$ or $p_0^2 D_0^2 s/k$ will provide correlation or scaling with regard to the onset of noble gas nucleation in Laval nozzle sources.

4) Cluster beam intensities (actually cluster densities) high enough to conduct electron diffraction can be attained in a size regime of great interest for study of the structure of

the condensed phase and possible deviations from bulk matter.

Acknowledgments

The authors would like to thank the Engineering Energetics section of the National Science Foundation and the Power Branch and the Chemistry Program of the Office of Naval Research for partial support of this work.

References

- ¹Hagena, O. F. and Obert, W., "Cluster Formation in Expanding Supersonic Jets: Effect of Pressure, Temperature, Nozzle Size, and Test Gas," Journal of Chemical Physics, Vol. 56, 1973, p. 1793.
- ²Hagena, O. F., Molecular Beams and Low Density Gas Dynamics, edited by P. P. Wegener, Marcel Dekker, New York, 1974.
- ³DeBoer, B. G., Kim, S. S., and Stein, G. D., "Molecular Beam Studies of Sulfur Hexafluoride Clustering in an Argon Carrier Gas from Both Free Jet and Laval Nozzle Sources," Rarefied Gas Dynamics, edited by R. Campargue, Commissariat A L'Energie Atomique, Paris, 1979, p. 1151.
- ⁴Obert, W., "Properties of Cluster Beams Formed with Supersonic Nozzles," Rarefied Gas Dynamics, edited by R. Campargue, Commissariat A L'Energie Atomique, Paris, 1979, p. 1181.
- ⁵Abraham, O., Binn, J. H., DeBoer, B. G., and Stein, G. D., "Gasdynamics of Very Small Laval Nozzles," submitted to Physics of Fluids, 1980.
- ⁶Bossel, U., "Investigation of Skimmer Interaction Influences on the Production of Aerodynamically Intensified Molecular Beams," Ph.D. thesis, Astronautical Sciences Division, Univ. of California, Berkeley, Calif., 1968.
- ⁷Armstrong, J. A., "An Investigation of the Physical Properties of Small Molecular Clusters Formed Via Homogeneous Nucleation in Nozzle Beams," Ph.D. thesis, Dept. of Mechanical Engineering and Astronautical Sciences, Northwestern University, Evanston, Ill., 1973.
- ⁸Hirschfelder, J. O., Curtiss, C. F., and Bird, R. B., Molecular Theory of Gases and Liquids, Table I-A, Wiley and Sons Inc., New York, 1964, pp. 1110-1111.

⁹ Briant, C. L. and Burton, J. J., "Molecular Dynamics Study of the Structure and Thermodynamic Properties of Argon Microclusters," Journal of Chemical Physics, Vol. 63, 1975, p. 2045.

¹⁰ Farges, J., deFeraudy, M. F., Raoult, B., and Torchet, G., "Structure Compacte Désordonnée et Agrégats Moléculaires Modèles Polytétraédriques," Journal de Physique Colloque C2, Vol. 36, 1975, pp. C2-13.

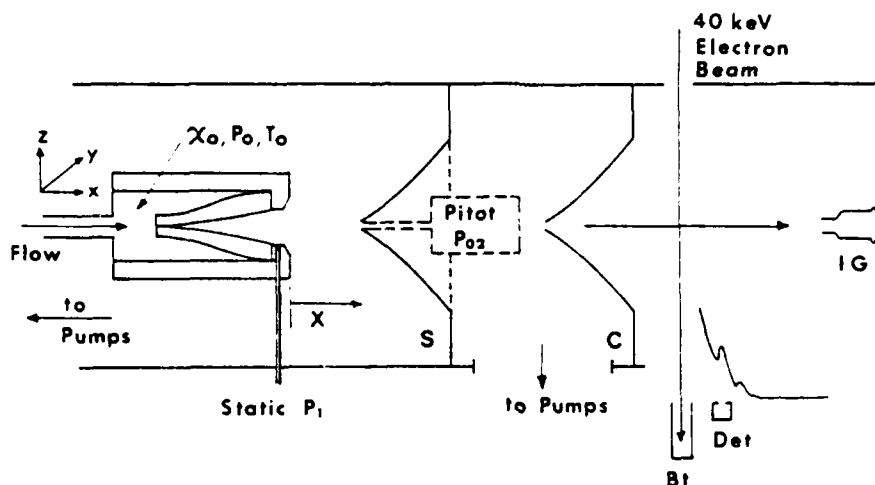
Table I Nozzle Geometry^{a)}

Nozzle Number	4	11	12	13
D ₀ -cm	0.0063	0.0089	0.0089	0.0056
D _e -cm	0.256	0.47	0.47	0.47
L ₀ -cm	3.15	1.176	1.356	1.293
a ₀	0.00635	0.0088	0.009	0.0055
a ₁	-0.0248	-0.0150	0.0150	-0.1402
a ₂	0.1488	4.6518	-1.6208	2.473
a ₃	-0.1156	-43.562	23.052	-13.2382
a ₄	0.0450	+180.334	-120.408	39.238
a ₅	-0.00637	-361.34	337.06	-63.936
a ₆	0	+378.88	-561.0	59.028
a ₇	0	-201.50	579.44	-29.728
a ₈	0	43.006	-366.	6.0812
a ₉	0	0	129.404	0
a ₁₀	0	0	-19.6	0

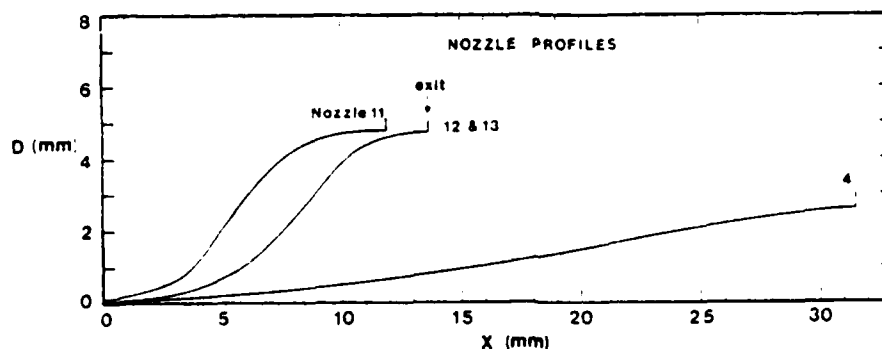
^{a)} A best fit polynomial equation of the form,

$$D(\chi) = \sum_{i=0}^{10} a_i \chi^i$$

is fitted to measured contours with D and χ in cm.



A



B

Fig. 1 The experimental arrangement shows the nozzle and stagnation chamber movable in xyz space with either a skimmer-S or a pitot probe and transducer located downstream of the nozzle exit. With the skimmer in place and collimator C a molecular beam is crossed with a 40 keV electron beam which is trapped in a beam trap BT. Diffraction patterns are taken with a detector Det. The nozzle contours are shown in 1b with additional details in Table I.

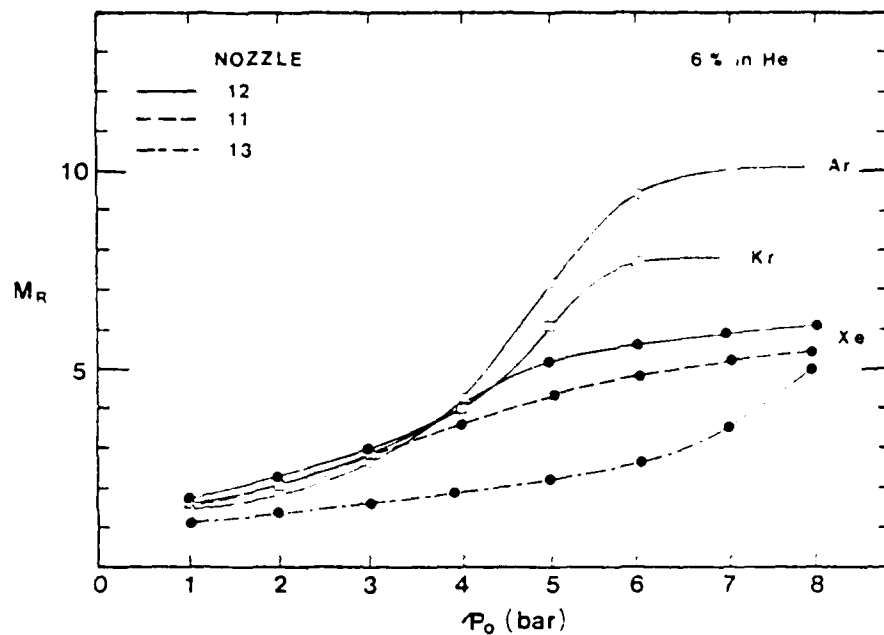


Fig. 2 Typical nozzle exit Mach numbers obtained using Eq. (1) are shown for nozzle 12 as the solid lines for Ar, Kr, and Xe and as dashed lines for Xe in nozzles 11 and 13. All expansions begin from room temperature $T_0 = 295$ K and $\chi_0 = 0.06$ in a He carrier gas.

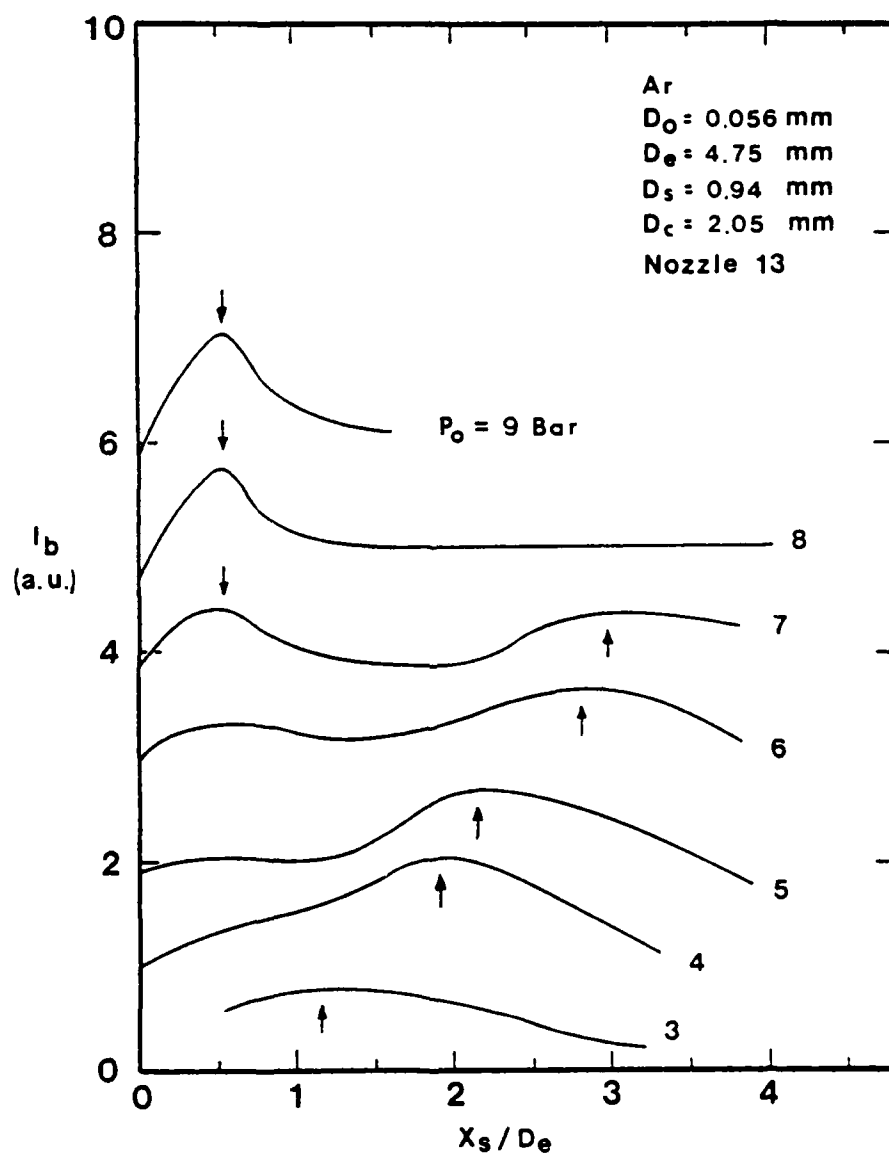


Fig. 3 Molecular beam intensities I_b are shown as a function of distance from the nozzle exit to the skimmer. The location of maximum beam intensity is indicated with an arrow.

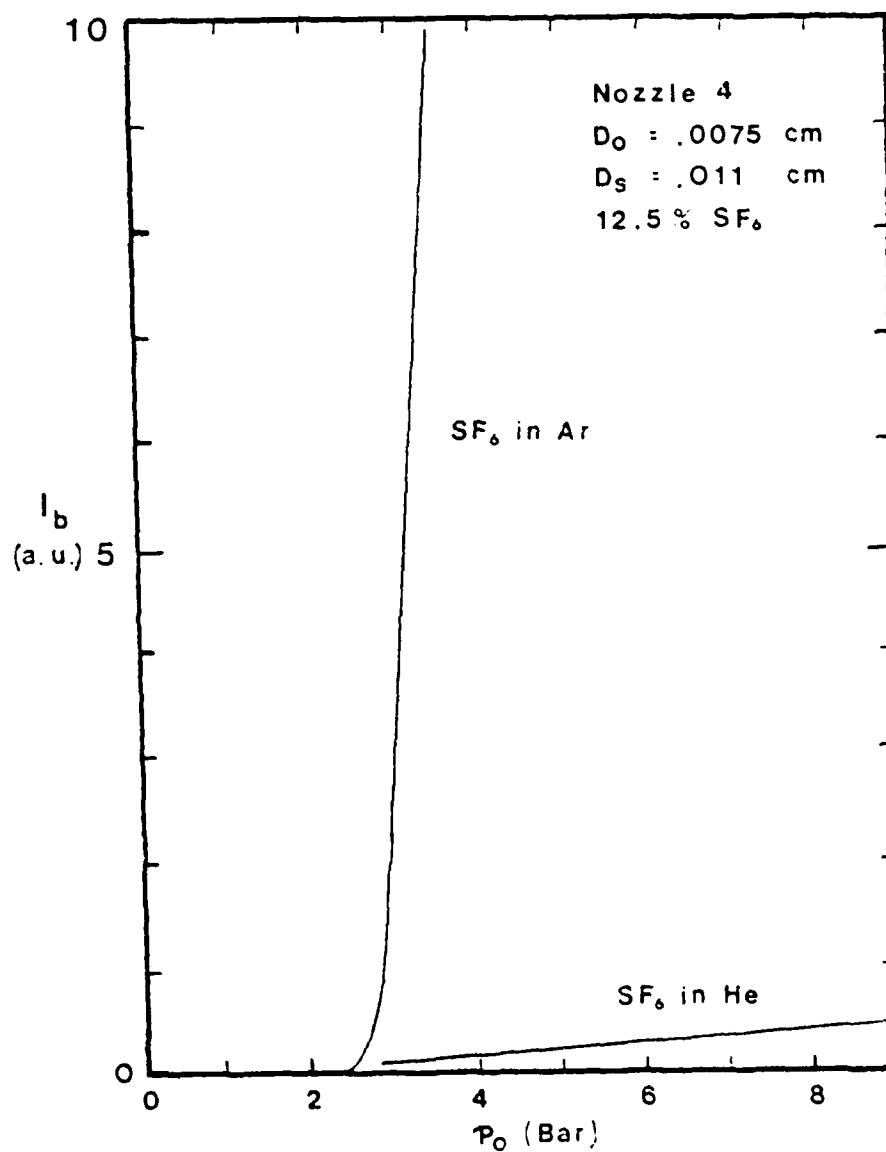


Fig. 4 Molecular beam intensities for SF_6 are shown for nozzle 4 with Ar and He carrier gases.

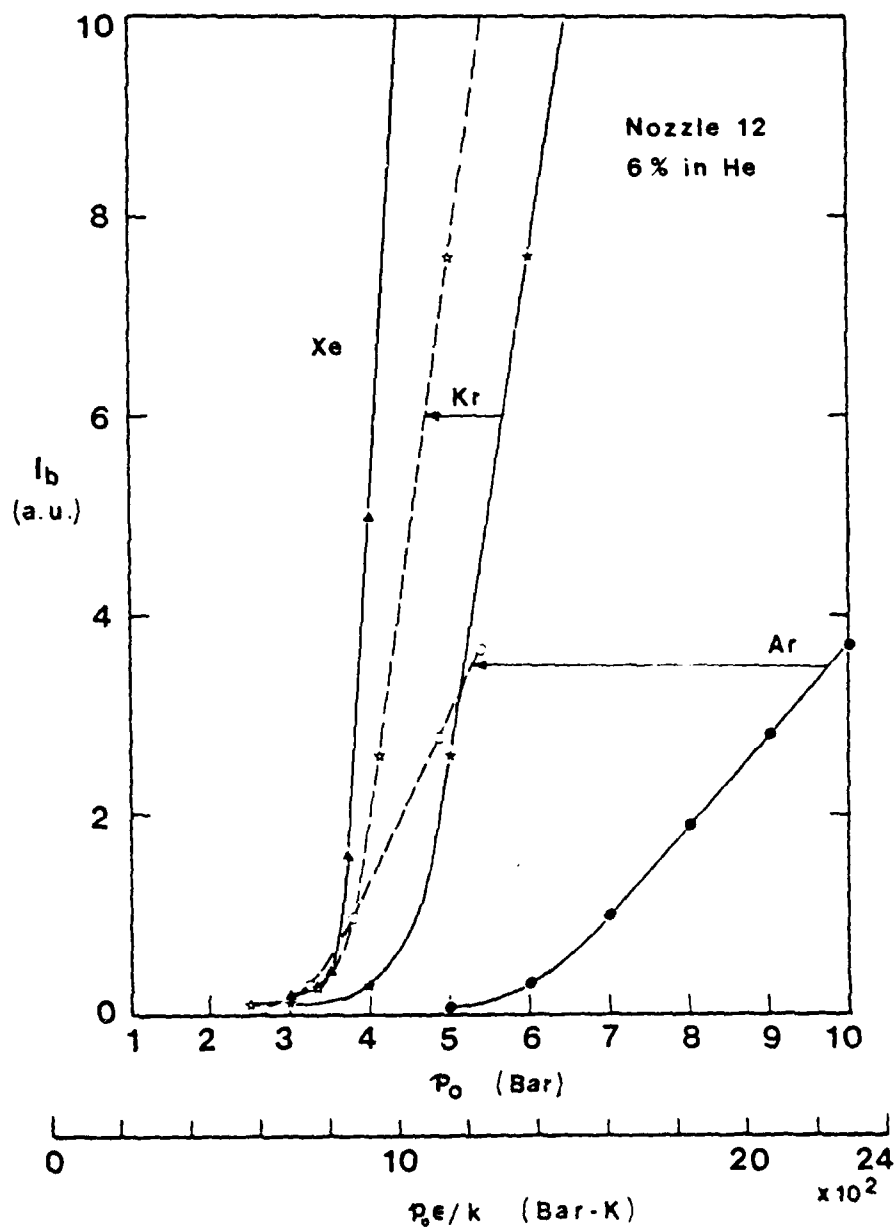


Fig. 5 Beam intensities as a function of p_0 are shown as the solid lines for nozzle 12 with $x_0 = 0.06$ and a He carrier gas. With a scale change to $p_0 \epsilon/k$, normalized to Xe, the curves for Ar and Kr move to the dashed lines as indicated by the arrows.

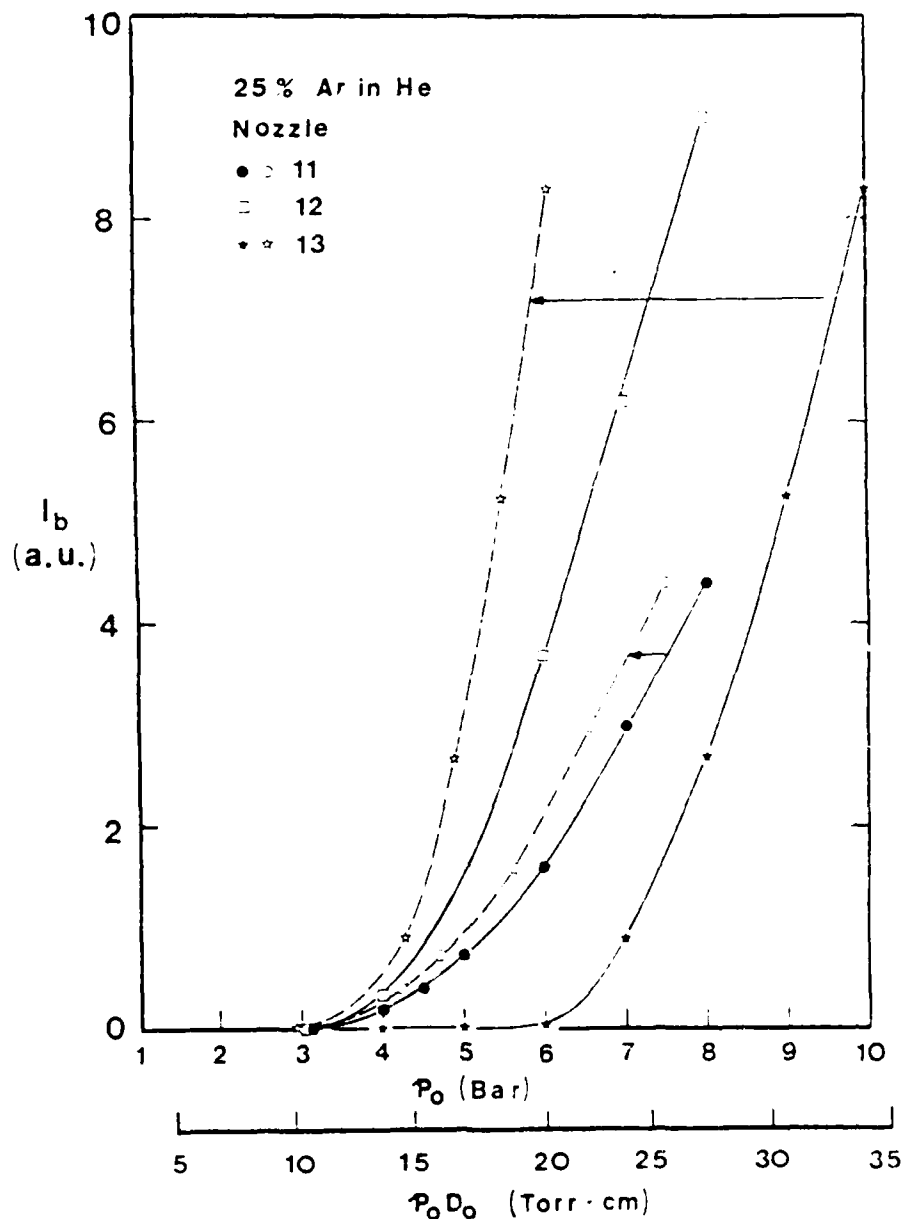


Fig. 6 Beam intensities as a function of p_0 are shown as the solid lines and as the dashed lines for $p_0 D_0$ normalized to nozzle 12 for Ar, $x_0 = 0.25$ in a He carrier gas.

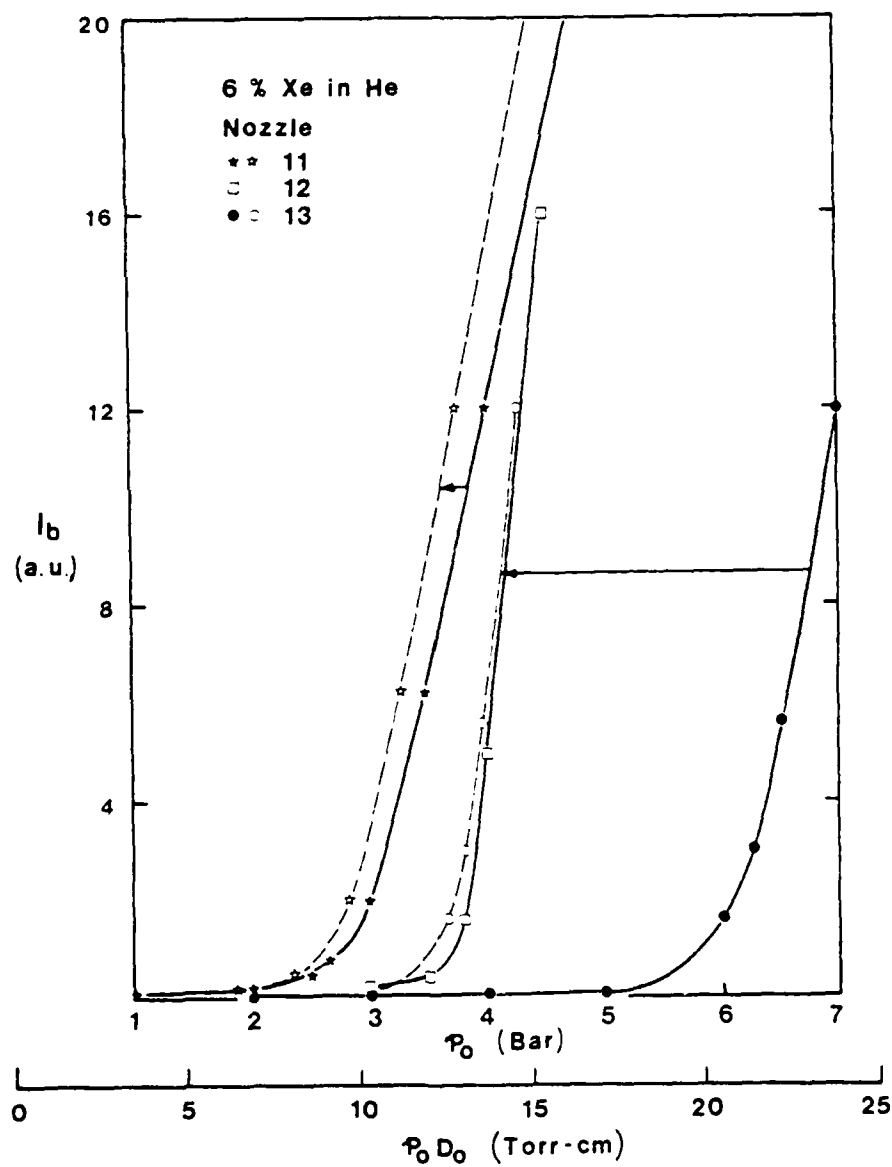


Fig. 7 Beam intensities as a function of p_0 are shown as solid lines with the dashed curves shifted for the ordinate $p_0 D_0$ normalized to nozzle 12 for Xe, $\chi_0 = 0.06$ in a He carrier gas.

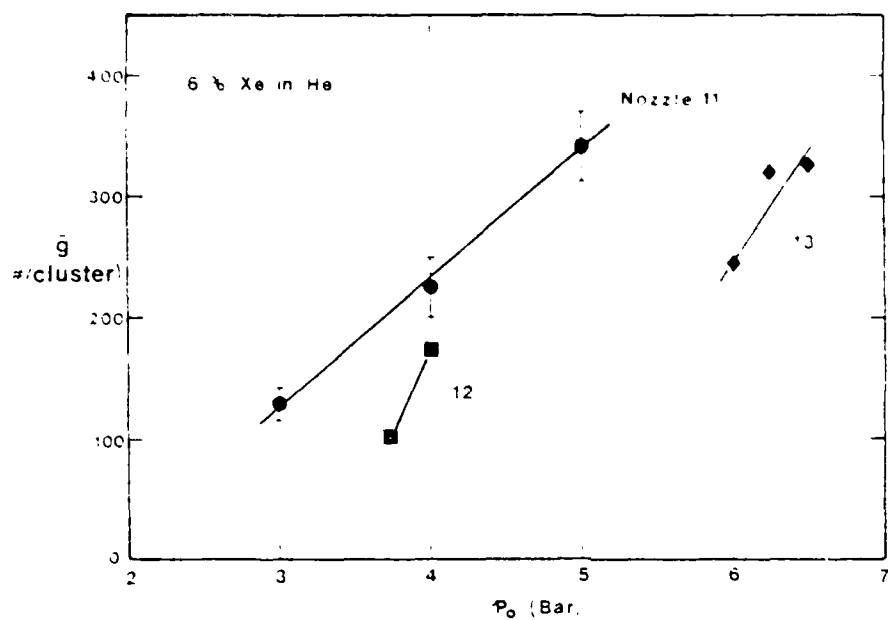


Fig. 8 The average number of atoms per cluster \bar{g} is shown as a function of p_0 for Xe, $x_0 = 0.06$ in a He carrier gas for nozzles 11-13.

INT.

ENERGETIC MATERIALS RESEARCHDISTRIBUTION LIST

	<u>No. Copies</u>		<u>No. Copies</u>
Assistant Secretary of the Navy (R, E, and S) Attn: Dr. R.E. Reichenbach Room 5E787 Pentagon Washington, DC 20350	1	AFATL Eglin AFB, FL 32542 Attn: Dr. Otto K. Heiney	1
Office of Naval Research Code 473 Arlington, VA 22217 Attn: Dr. R. Miller	10	AFRPL Code PACC Edwards AFB, CA 93523 Attn: Mr. W. C. Andrepont	1
Office of Naval Research Code 200B Arlington, VA 22217 Attn: Dr. J. Enig	1	AFRPL Code CA Edwards AFB, CA 93523 Attn: Dr. R. R. Weiss	1
Office of Naval Research Code 260 Arlington, VA 22217 Attn: Mr. D. Siegel	1	Code AFRPL MKPA Edwards AFB, CA 93523 Attn: Mr. R. Geisler	1
Office of Naval Research Western Office 1030 East Green Street Pasadena, CA 91106 Attn: Dr. T. Hall	1	Code AFRPL MKPA Edwards AFB, CA 93523 Attn: Dr. F. Roberto	1
Office of Naval Research Eastern Central Regional Office 495 Summer Street Boston, MA 02210 Attn: Dr. L. Peebles Dr. A. Wood	2	AFSC Andrews AFB, Code DLFP Washington, DC 20334 Attn: Mr. Richard Smith	1
Office of Naval Research San Francisco Area Office One Hallidie Plaza Suite 601 San Francisco, CA 94102 Attn: Dr. P. A. Miller	1	Air Force Office of Scientific Research Directorate of Chemical & Atmospheric Sciences Bolling Air Force Base Washington, DC 20332	1
Defense Technical Information Center DTIC-DDA-2 Cameron Station Alexandria, VA 22314	12	Air Force Office of Scientific Research Directorate of Aero- space Sciences Bolling Air Force Base Washington, DC 20332 Attn: Dr. L. H. Caveny	1
		Anal-Syn Lab Inc. P.O. Box 547 Paoli, PA 19301 Attn: Dr. V. J. Keenan	1

	<u>No. Copies</u>		<u>No. Copies</u>
Army Ballistic Research Labs Code DRDAR-BLP Aberdeen Proving Ground, MD 21005 Attn: Mr. L. A. Watermeier	1	Hercules Inc. Eglin AFATL/DL DL Eglin AFB, FL 32542 Attn: Dr. Ronald L. Simmons	1
Army Ballistic Research Labs ARRADCOM Code DRDAR-BLP Aberdeen Proving Ground, MD 21005 Attn: Dr. Ingo W. May	1	Hercules Inc. Magna Bacchus Works P.O. Box 98 Magna, UT 84044 Attn: Mr. E. H. DeButts	1
Army Ballistic Research Labs ARRADCOM Code DRDAR-BLT Aberdeen Proving Ground, MD 21005 Attn: Dr. Philip Howe	1	Hercules Inc. Magna Bacchus Works P.O. Box 98 Magna, UT 84044 Attn: Dr. James H. Thacher	1
Army Missile Command Code DRSME-RK Redstone Arsenal, AL 35809 Attn: Dr. R. G. Rhoades Dr. W. W. Wharton	2	HQ US Army Material Development Readiness Command Code DRCDE-DW 5011 Eisenhower Avenue Room 8N42 Alexandria, VA 22333 Attn: Mr. S. R. Matos	1
Atlantic Research Corp. 5390 Cherokee Avenue Alexandria, VA 22314 Attn: Dr. C. B. Henderson	1	Johns Hopkins University APL Chemical Propulsion Information Agency Johns Hopkins Road Laurel, MD 20810 Attn: Mr Theodore M. Gilliland	1
Ballistic Missile Defense Advanced Technology Center P.O. Box 1500 Huntsville, AL 35807 Attn: Dr. David C. Sayles	1	Lawrence Livermore Laboratory University of California Livermore, CA 94550 Attn: Dr. M. Finger	1
Ballistic Research Laboratory USA ARRADCOM DRDAR-BLP Aberdeen Proving Ground, MD 21005 Attn: Dr. A. W. Barrows	1	Lawrence Livermore Laboratory University of California Livermore, CA 94550 Attn: Dr. R. McGuire	1
Hercules Inc. Cumberland Aerospace Division Allegany Ballistics Lab P.O. Box 210 Cumberland, MD 21502 Attn: Dr. Rocco Musso	2	Lockheed Missiles and Space Co. P.O. Box 504 Sunnyvale, CA 94088 Attn: Dr. Jack Linsk Org. 83-10 Bldg. 154	1

	<u>No. Copies</u>		<u>No. Copies</u>
Lockheed Missile & Space Co. 3251 Hanover Street Palo Alto, CA 94304 Attn: Dr. H. P. Marshall Dept. 52-35	1	Naval Research Lab Code 6100 Washington, DC 20375	1
Los Alamos Scientific Lab P.O. Box 1663 Los Alamos, NM 87545 Attn: Dr. R. Rogers, WX-2	1	Naval Sea Systems Command Washington, DC 20362 Attn: Mr. G. Edwards, Code 62R3 Mr. J. Murrin, Code 62R2 Mr. W. Blaine, Code 62R	1
Los Alamos Scientific Lab P.O. Box 1663 Los Alamos, NM 87545 Attn: Dr. B. Craig, M Division	1	Naval Sea Systems Command Washington, DC 20362 Attn: Mr. R. Beauregard SEA 64E	1
Naval Air Systems Command Code 330 Washington, DC 20360 Attn: Mr. R. Heitkotter Mr. R. Brown	1	Naval Surface Weapons Center Code R11 White Oak, Silver Spring, MD 20910 Attn: Dr. H. G. Adolph	1
Naval Air Systems Command Code 310 Washington, DC 20360 Attn: Dr. H. Mueller Dr. H. Rosenwasser	1	Naval Surface Weapons Center Code R13 White Oak, Silver Spring, MD 20910 Attn: Dr. R. Bernecker	1
Naval Explosive Ordnance Disposal Facility Indian Head, MD 20640 Attn: Lionel Dickinson Code D	1	Naval Surface Weapons Center Code R10 White Oak, Silver Spring, MD 20910 Attn: Dr. S. J. Jacobs	1
Naval Ordnance Station Code 5034 Indian Head, MD 20640 Attn: Mr. S. Mitchell	1	Naval Surface Weapons Center Code R11 White Oak, Silver Spring, MD 20910 Attn: Dr. M. J. Kamlet	1
Naval Ordnance Station Code PM4 Indian Head, MD 20640 Attn: Mr. C. L. Adams	1	Naval Surface Weapons Center Code R04 White Oak, Silver Spring, MD 20910 Attn: Dr. D. J. Pastine	1
Dean of Research Naval Postgraduate School Monterey, CA 93940 Attn: Dr. William Tolles	1	Naval Surface Weapons Center Code R13 White Oak, Silver Spring, MD 20910 Attn: Dr. E. Zimet	1
Naval Research Lab Code 6510 Washington, DC 20375 Attn: Dr. J. Schnur	1		

6/80

4

	<u>No. Copies</u>		<u>No. Copies</u>
Naval Surface Weapons Center Code R101 Indian Head, MD 20640 Attn: Mr. G. L. MacKenzie	1	Naval Weapons Center Code 388 China Lake, CA 93555 Attn: D. R. Derr	1
Naval Surface Weapons Center Code R17 Indian Head, MD 20640 Attn: Dr. H. Haiss	1	Naval Weapons Center Code 388 China Lake, CA 93555 Attn: Dr. R. Reed Jr.	1
Naval Surface Weapons Center Code R11 White Oak, Silver Spring, MD 20910 Attn: Dr. K. F. Mueller	1	Naval Weapons Center Code 385 China Lake, CA 93555 Attn: Dr. A. Nielsen	1
Naval Surface Weapons Center Code R16 Indian Head, MD 20640 Attn: Dr. T. D. Austin	1	Naval Weapons Center Code 3858 China Lake, CA 93555 Attn: Mr. E. Martin	1
Naval Surface Weapons Center Code R122 White Oak, Silver Spring, MD 20910 Attn: Mr. L. Roslund	1	Naval Weapons Center China Lake, CA 93555 Attn: Mr. R. McCarten	1
Naval Surface Weapons Center Code R121 White Oak, Silver Spring, MD 20910 Attn: Mr. M. Stosz	1	Naval Weapons Support Center Code 5042 Crane, Indiana 47522 Attn: Dr. B. Douda	1
Naval Weapons Center Code 3853 China Lake, CA 93555 Attn: Dr. R. Atkins	1	Rohm and Haas Company 723-A Arcadia Circle Huntsville, Alabama 35801 Attn: Dr. H. Shuey	1
Naval Weapons Center Code 3205 China Lake, CA 93555 Attn: Dr. L. Smith	1	Strategic Systems Project Office Dept. of the Navy Room 901 Washington, DC 20376 Attn: Dr. J. F. Kincaid	1
Naval Weapons Center Code 3205 China Lake, CA 93555 Attn: Dr. C. Thelen	1	Strategic Systems Project Office Dept. of the Navy Room 1048 Washington, DC 20376 Attn: Mr. E. L. Throckmorton Mr. R. Kinert	2
Naval Weapons Center Code 385 China Lake, CA 93555 Attn: Dr. A. Amster	1	Thiokol Chemical Corp. Brigham City Wasatch Division Brigham City, UT 84302 Attn: Dr. G. Thompson	1

	<u>No. Copies</u>		<u>No. Copies</u>
USA ARRADCOM DRDAR-LCE Dover, NJ 07801 Attn: Dr. R. F. Walker	1	University of California Department of Chemistry 405 Hilgard Avenue Los Angeles, CA 90024 Attn: Professor M. Nicol	1
USA ARRADCOM DRDAR-LCE Dover, NJ 07801 Attn: Dr. N. Slagg	1	University of California Energy Center Mail Code B-010 La Jolla, CA 92093 Attn: Prof. S.S. Penner	1
U.S. Army Research Office Chemistry Division P.O. Box 12211 Research Triangle Park, NC 27709	1	University of Washington Department of Chemistry Seattle, Washington 98195 Attn: Prof. B.S. Rabinovitch	1
Washington State University Dept. of Physics Pullman, WA 99163 Attn: Professor G.D. Duval	1	Dr. P. Rentzepis Bell Laboratories Murray Hill N.J. 07971	1
Space Sciences, Inc. 135 West Maple Avenue Monrovia, CA 91016 Attn: Dr. M. Farber	1	University of Southern CA Department of Electrical Engineering University Park Los Angeles, CA 90007	1
SRI International 333 Ravenswood Avenue Menlo Park, CA 94025 Attn: Mr. M. Hill	1		
Office of Naval Research Code 421 Arlington, VA 22217 Attn: Dr. B. Junker	1		
The Johns Hopkins University Department of Chemistry Baltimore, MD 21218 Attn: Dr. Joyce J. Kaufman	1		
University of California Department of Chemistry Berkeley, CA 94720 Attn: Professor Y.T. Lee	1		
Office of Naval Research Code 172 Arlington, VA 22217 Attn: Dr. G. Neede	1		